Faculty of Sciences
Physics and Astronomy

Biophysical Mechanisms of Cardiac Arrhythmias due to Fibrosis and other Pathological Conditions

Ivan V. Kazbanov

Promotor: Prof. Dr. Alexander V. Panfilov

2016

Contents

Summary

Acute cardiac arrhythmias are the main cause of death in industrialized countries. Despite tremendous clinical importance, the mechanisms behind the onset and dynamics of cardiac arrhythmias are still poorly understood. The most dangerous cardiac arrhythmias are ventricular tachycardia and ventricular fibrillation. The latter arrhythmia is lethal unless treated within several minutes. The former arrhythmia is very dangerous because it can spontaneously convert into the latter, which, in turn becomes lethal if left untreated for several minutes.

The heart is an excitable medium where waves of excitation can propagate. These waves coordinate the synchronous contraction of cardiac muscle, making the cardiac muscle work synchronously. Cardiac arrhythmias are associated with formation of reentry activity and spiral waves. Once formed, the spiral waves act as pacemakers which excite the tissue with high frequency. Therefore, the spiral waves are often referred to as the arrhythmia sources. To understand the formation and the dynamics of the spiral wave is one of the main research questions of the field.

Normally, a cardiac arrhythmia is an exceptional event, since the heart is capable of doing about 2 billion contractions without triggering rhythm abnormalities. Therefore, cardiac rhythms disruptions are associated with pathophysiological conditions. Such conditions are often amplified in the presence of cardiac arrhythmias, resulting in positive feedback.

Recent advances in computational sciences and the amount of data accumulated by *in vitro* and *in vivo* experiments allow simulating the behavior of cardiac rhythms with mathematical modeling. This approach complements experimental studies and clinical investigations by allowing the performance of wide range of numerical experiments that can pinpoint to a particular mechanism responsible for a given phenomena.

In this thesis we use mathematical modeling and numerical methods to study the effects of pathophysiological conditions on arrhythmogenesis. Our focus lies on two pathophysiological conditions: cardiac ischemia and myocardial fibrosis. Cardiac ischemia is a lack of a proper blood supply in the heart, which often triggers ventricular fibrillation. Conversely, once ventricular fibriallation is present, it is always accompanied by cardiac ischemia. Myocardial fibrosis is a state char-

acterized by an excess of connective tissue in the heart, which may have a drastic effect on cardiac excitation dynamics.

We show that global cardiac ischemia stabilizes the cardiac activation pattern, and reduces the chance for fibrillation to be spontaneously terminated. We characterize the effect of each ischemia factor on the activation pattern and find the factors responsible for acceleration and deceleration of activation. Using these results together with the results of a clinical investigation, we estimate the time dynamics of ischemia processes for the first few minutes of ischemia in the human heart.

Next, we study the effect of the spatial distribution of fibrosis on the onset of cardiac arrhythmias. We demonstrate that a tissue with homogeneous distribution of fibrosis is less susceptible to arrhythmia induction than a tissue with heterogeneous distribution of fibrosis. Our study shows how the dynamics and the mechanism of induced activation patterns depend on the fibrosis distribution. We find that the period of activation patterns is determined by the regions with the slowest arrhythmia sources. We also discover the mechanism of the underlying arrhythmia and provide insights about the ablation protocols that could terminate the activity.

Finally, we investigate the reason why the period of the activation pattern is determined by the regions with the lowest frequency of spiral rotation in the case of a heterogeneous fibrosis distribution. We show that such regions can attract the arrhythmia sources. We investigate the mechanism for this attraction and provide the conditions when this attraction is possible. We characterize this effect in terms of ECG morphology and show that this attraction is also observed in clinical studies.

In addition, we develop a patient specific model of the geometry of the left human ventricle. This model is based on the clinical MRI data

In addition, we develop a patient specific model of cardiac myofiber orientation to study the effect of attraction the magnetic resonance images of patients.

We conclude that mathematical modeling is an invaluable source of insights into the mechanisms behind cardiac arrhytmias. Our research shed new light on the overall dynamics of spiral waves in arrhythmias and the mechanisms underlying triggering of arrhythmic sources, subject to various pathological conditions. We believe that our results are useful for development of more effective ablation protocols for treating arrhythmias and for making predictions on how a particular tissue architecture is susceptible to arrhythmia induction in the heart.

Samenvatting

Acute hartritmestoornissen zijn de primaire doodszoorzaak in geïndustrialiseerde landen. Ondanks de overweldigende klinische relevantie, worden de mechanismen die zich schuilhouden achter het ontstaan en de dynamica van hartritmestoornissen nog steeds zeer slecht begrepen. De gevaarlijkste hartritmestoornissen zijn ventriculaire tachycardie en ventrikelfibrilleren. De laatstgenoemde is dodelijk tenzij het behandeld wordt binnen enkele minuten, terwijl de eerstgenoemde zeer gevaarlijk is aangezien het spontaan in ventrikelfibrilleren kan evolueren.

Het hart is een exciteerbaar medium waarin excitatiegolven zich voort kunnen bewegen. Deze golven coördineren de contractie van het hart op dergelijke wijze dat de hartspier synchroon werkt. Hartritmestoornissen worden geassocieerd met het ontstaan van 'reentry activity' en spiraalgolven. Eenmaal gevormd, spelen de spiraalgolven de rol van pacemakers die het weefsel exciteren met hoge frequentie. Daarom worden spiraalgolven dikwijls aangeduid als de bron van de ritmestoornissen. De totstandkoming en dynamica van de spiraalgolf is een van de belangrijke open onderzoeksvragen in het veld.

Eigenlijk is een hartritmestoornis een buitengewoon fenomeen aangezien het hart in staat is om ongeveer 2 miljard keer samen te trekken zonder afwijkingen in het ritme te veroorzaken. Omwille van deze reden worden hartritme stoornissen geassocieerd met pathofysiologische omstandigheden. Zulke omstandigheden worden dikwijls versterkt door de aanwezigheid van hartritmestoornissen aangezien deze een positieve feedback geven.

Recente vooruitgang in de computerwetenschappen en de hoeveelheid data die verzameld wordt in *in vitro* en *in vivo* experimenten laten toe om hartritmes te simuleren met behulp van wiskundige modellering. Deze aanpak is complementair met experimentele studies en klinische onderzoeken aangezien het toelaat om een grote hoeveelheid numerieke experimenten uit te voeren. Hierbij kan gefocust worden op een specifiek mechanisme verantwoordelijk voor een gegeven fenomeen.

In deze thesis gebruiken we wiskundige modellering en numerieke methoden om de effecten van pathofysiologische condities te bestuderen op het ontstaan van hartritmestoornissen. Onze focus ligt bij twee pathofysiologische con-

dities: cardiale ischemie en fibrose van het myocardium. Cardiale ischemie is een gebrek aan goede bloedtoevoer in het hart, wat dikwijls aanleiding geeft tot ventrikelfibrilleren. Eenmaal ventrikelfibrilleren aanwezig is in het hart, is er bovendien ook steeds ischemie te vinden. Fibrose van het myocardium is een toestand gekarakteriseerd door een teveel aan bindweefsel in het hart, wat drastisch kan wijzigen de dynamica van de hartexcitatie.

We tonen aan dat globale ischemie van het hart het activatiepatroon stabiliseert en de kans reduceert dat fibrillatie spontaan eindigt. We karakteriseren het effect van elke ischemiefactor op het activatiepatroon en vinden zo de factoren verantwoordelijk voor het versnellen en vertragen van de activatie. Wanneer deze resultaten gebruikt worden samen met de resultaten van klinische onderzoeken, schatten we de tijdsdynamica van ischemie processen af voor de eerste paar minuten van ischemie in het menselijk hart.

Vervolgens bestuderen we het effect van de ruimtelijke verdeling van fibrose op het ontstaan van hartritmestoornissen. We tonen aan dat weefsel met een homogeen verdeelde distributie van fibrose minder vatbaar is voor inductie van ritmestoornis dan weefsel met een heterogeen verdeelde distributie. Onze studie toont aan hoe de dynamica en het mechanisme van geïnduceerde activatiepatronen afhangen van de distributie van fibrose. We vinden dat de periode van de activatiepatronen bepaald wordt door de regio's met de traagste ritmestoornisbronnen. We beschrijven ook het mechanisme van het activatiepatroon en bieden inzicht over ablatieprotocols die de activiteit kunnen stoppen.

Tot slot onderzoeken we de reden waarom de periode van het activatiepatroon bepaald wordt door de regio's met de laagste frequenties voor spiraalrotatie in het geval van een heterogene distributie van fibrose. We tonen aan dat zulke regio's de bronnen van ritmestoornissen kunnen aantrekken. We onderzoeken het mechanisme voor deze aantrekking en bepalen onder welke voorwaarden deze aantrekking mogelijk is. We beschrijven dit effect in termen van de morfologie van het electro-cardiogram (ECG) en tonen tevens aan dat deze aantrekking ook geobserveerd wordt in klinische studies.

Daarnaast ontwikkelen we een patiëntspecifiek model van de oriëntatie van spiervezels in het hart om het effect van aantrekking te bestuderen op MRI beelden van patiënten.

We concluderen dat wiskundige modellering een onschatbare bron van inzicht biedt in de mechanismen achter hartritmestoornissen. Ons onderzoek laat nieuw licht schijnen op de mechanismen van het opwekken en de algemene dynamica van ritmestoornissen onder verschillende pathofysiologische omstandigheden. We geloven dat onze resultaten nuttig zijn voor het ontwikkelen van meer effectieve ablatieprotocols bij het behandelen van ritmestoornissen en bij het maken van voorspellingen voor hoe een bepaalde weefselarchitectuur vatbaar is voor de inductie van een hartritmestoornis.

Abbreviations

A-V Atrio-ventricular

ADP Adenosine diphosphate

AF Atrial fibrillation

APD Action potential duration

ATP Adenosine triphosphate

BZ Belousov-Zhabotinsky

CV Conduction velocity

ECG Electrocardiogram

LGE Late gadolinium enhanced

MRI Magnetic resonance imaging

ODE Ordinary differential equation

PS Phase singularity

RFCA Radio frequency catheter ablation

VF Ventricular fibrillation

VT Ventricular tachycardia

Chapter 1

General Introduction

1.1 The Heart

> *— Yes, man is mortal, but that would be only half the trouble. The worst of it is that he's sometimes unexpectedly mortal—there's the trick!*
>
> — Mikhail Bulgakov, The Master and Margarita

The heart is a biological machine whose only function is to pump the blood. There are several reasons why the blood must constantly flow within the body: it transports chemical signals from glands to other organs, delivers nutritive materials and oxygen to all the cells, and washes away the toxic by-products. Thereby the blood flow is responsible for the body's metabolism. For these reasons, an arrest of the normal blood flow makes the organs suffer from both the lack of energy and the accumulation of toxins. Most organs and tissues, like skeletal muscles, are capable of surviving for several hours under such conditions, however there is one notable and important exception: the brain. The brain must always have a constant supply of glucose and oxygen to function properly. Even a short-term disruption in the delivering of these components is followed by loss of consciousness and coma. An arrest of perfusion for more than 10–15 minutes leads to brain death. This makes the heart—the blood pumping machine—one of the most vital organs, justifying its symbolic value in different languages and cultures.

As straightforward as it may seem, pumping blood in the body is not that straight forward. The proof of this fact is that despite the recent advances in electronics and material technology, mankind has still not created an artificial heart that could deliver a life quality comparable to what the natural heart delivers. The most important reason for this is, of course, the lack of proper materials which would not trigger blood coagulation and could be calcification-proof. However, another important reason is that the heart is an "intelligent" pump which adapts for the demands of other organs. For instance, at rest, blood flows at the rate of approximately 5 liter per minute corresponding to a heart rate of about 1 beat per second. However, under heavy stress, the flow can increase up to 6 times with a corresponding 3-fold increase in the pacing rate. Up to a certain extent this process is regulated by the heart itself. In addition, the heart responds to external (neural and humoral) regulation; for instance, the release of adrenaline in times of danger causes an increase in both the heart rate and the intensity of contractions.

Being a pumping machine the heart performs periodic work. This work is coordinated by a special electrical signal which is called an *action potential*. There are four important features of the heart that make its work possible: *excitability, automaticity, conductivity, and contractility*. The first property—excitability—is the ability of the cardiac tissue to respond to stimulation. If an electrode is

placed somewhere in the cardiac tissue, applying an electrical stimulation on that electrode results in generation of the action potential. The second property—automaticity—is the ability of the heart to generate the action potential by itself, without any external stimulation. Even if the heart is physically extracted from the body, it is still able to work provided one can perfuse it normally. The automaticity of the heart is normally controlled by special cardiac cells called *pacemakers*. The third property—conductivity—is the ability of the signal to propagate. The action potential generated by a cardiac cell is transmitted to a next cardiac cell, connecting all the heart cells together. The velocity of such propagation in the heart varies from region to region but is usually of the order of 10–100 cm/s. Finally, the fourth property—contractility—is the ability of the cardiac cells to shorten their length by transforming chemical energy into mechanical energy. The contraction of a cell is regulated by a special sub-system which is coupled to the action potential generation.

In the norm, these four properties of the heart contribute to periodic synchronize contraction. This is due to periodic generation of the signal, its rapid synchronous delivery, and coupling of the signal to mechanical action. In this case the heart performs its pumping function. However, in some cases a disruption of this rhythm becomes possible. This phenomenon is known as *cardiac arrhythmia*, and many of cardiac arrhythmias are extremely dangerous since they can lead to insufficiency or a complete arrest of the blood flow which, as was mentioned earlier, is of vital importance. The most dangerous arrhythmias are called *acute*; they occur spontaneously and more often than not they have a lethal outcome: *sudden cardiac death*. Nowadays, this is the major reason of death in the Western world. Therefore, understanding the conditions leading to cardiac arrhythmias, and the underlying mechanism of formation of cardiac arrhythmias is of ultimate importance.

1.2   Excitable Media

In this section we shall introduce the concept of *excitable medium*. Since the beginning of the last century, excitable media have been intensively studied both experimentally and theoretically. The reason for this widespread interest is that a vast amount of physical, chemical and biological systems can be considered as excitable media. Despite the different nature of such systems there are many generic properties that all excitable media share. In the following sections we shall reformulate the main problem of cardiac electrophysiology—formation of cardiac arrhythmias—in terms of excitable media.

An excitable medium is a medium formed by interconnected excitable elements, which upon being slightly disturbed generate a pronounced response. An element of an excitable medium can be in one of three possible states (or phases): *excited*, *refractory* and *recovered*. If an element of the excitable medium is

stimulated when it is in the recovery phase, it can generate a response and become excited. This phase is followed by the refractory phase, during which it is not possible to excite the element again. After the refractory phase, the element recovers and becomes ready for a next excitation.

Perhaps, the most visual example of an excitable medium is the wave of audience (the Mexican wave) that can be observed in stadiums during football matches. The element of this excitable medium is a spectator, which can either stay raising his arms (excited phase) or sit at his place (refractory if he does not want to stand again, or recovered otherwise). Upon seeing a standing neighbor (stimulation) the spectator stands up (generates a response), so another sitting neighbor can see that and stand up as well. In a while the spectator sits down (refractory), takes rest (recovers), and gets ready for next stimulation.

Excitable medium is an instance of a more general class: *active medium*. An active medium is a medium formed by interconnected elements that possess stored energy. This energy or a part of this energy can be released on stimulating. Apart from excitable medium, there are other types of active media: *trigger* (or *bistable*) and *oscillating*. An element of a trigger system can be in two phases: "high-energy" and "low-energy." By stimulation the element can change its phase from "high-energy" to "low-energy" and then stay in the latter state forever. A good example of a trigger system is dominoes standing in a row. The energy is stored in the gravitational field: a standing domino is in the "high-energy" phase. Given a stimulus the domino can be knocked or, in other words, brought to the "low-energy" state. During this change of the state, the domino stimulates the next domino. This, in turn, results in change of the state for the next domino.

Trigger media can serve as a model of excitable media provided we are interested excursively in the excitation process. Then the "high-energy" state corresponds to the recovered state and the "low-energy" state corresponds to the excited state. Furthermore, the same system can be considered to be both trigger and excitable depending on the time scale. If one considers propagation of fire in a forest, he deals with a trigger system since it is not possible to burn the same tree twice. However, on a larger time scale, a recovery process takes place: the burned trees are replaced, so the system can be considered as excitable.

Finally, an oscillating medium is a medium formed by interconnected elements that possess intrinsic periodic activity. Stimulation of an element may cause an increase or decrease of its oscillating frequency. Oscillating media can also serve as a model for excitable media under certain conditions.

The given examples have introduced a concept of *wave propagation*. A wave is a process that is periodic in time-space. In active media the wave exists because of two reasons: the ability of an element to generate a strong response as the result of weak stimulation and the link between neighboring elements. A wave is an emergent phenomenon: a consequence of cooperative behavior of the elements.

The theory of excitable and active media which started in the middle of the

last century, has nowadays become well established interdisciplinary science. The main results of this theory will be covered in the following sections, after we reveal a connection between the heart and exitable media.

1.3 Heart as an Excitable Medium

In the beginning of the introduction the heart was considered from holistic point of view. To complement that description, now we shall consider the heart staying on the position of reductionalism by putting more attention to the structural details.

The active element of the heart is cardiac muscle or *myocardium*, whose active elements are cardiac muscle cells or *myocytes*. A myocyte, as any other cell, has a membrane separating its inner volume from the external medium. Through the membrane, the myocyte creates electrical field by maintaining certain concentrations of electrically charged ions in its inner volume. The myocyte has two properties that make it an active element. First, the gradients of ionic concentrations maintained by the myocyte store energy. Second, a part of this energy can be released in response to external disruption of the transmembrane electrical field. Most myocytes can recover to their initial state, so they are excitable elements. The myocytes of this type are also capable of performing mechanical work, they are called *working* myocytes. The other myocytes do not have a resting state: they become excited and recovered spontaneously. The latter myocytes are called *nodal* myocytes, and they are oscillating elements.

The myocytes—the active elements—are electrically connected through special membrane proteins: *gap junctions*. This connection allows a myocyte to excite its neighboring myocytes, which results in raising of excitation wave. This is the process of signal propagation that was described in the beginning of the introduction.

On the cellular level the process of excitation and recovery of a myocyte is driven by *ionic channels* located at the membrane. These channels are molecular machines that allow electrically charged ions to flow through them under certain conditions. Most of the channels are specific, that is permeable to only one type of ions. The major role in cardiac excitation is played by the sodium, potassium and calcium ionic channels. Opening and closing of the channels is mostly regulated by the transmembrane electric field, which, in turn, is described as the difference of electric potentials between the inner volume of the cell and the extracelluar medium. This difference is called *transmembrane voltage*.

The schematic plot of a cardiac action potential is given in Fig. 1.1. At rest, the human myocyte maintains its transmembrane voltage at the level of about -85 mV. If, by external stimulation, this voltage becomes larger than about -40 mV, then the myocyte starts to generate the response—the action potential. The initial phase of the action potential is a rapid change of the transmembrane
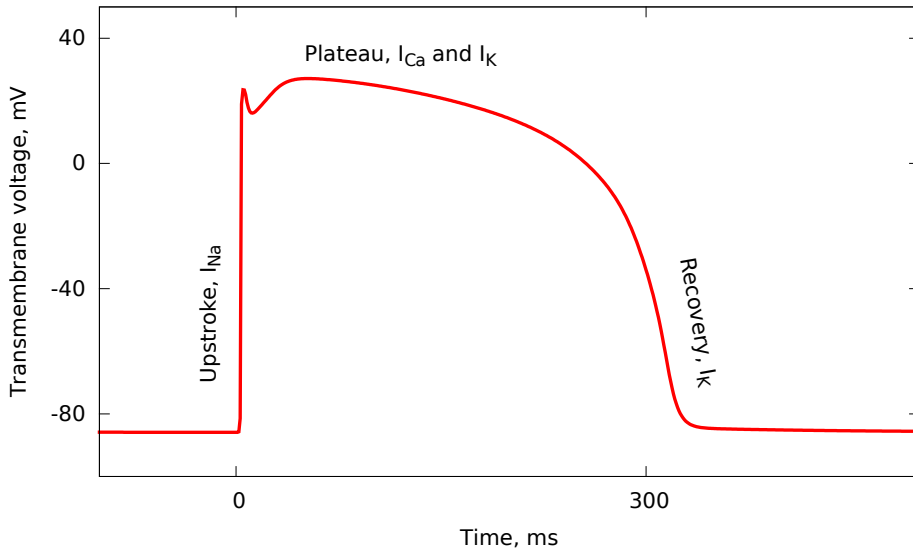
Figure 1.1. Schematic plot of a cardiac action potential with main ionic currents involved in each phase.

voltage to the peak value of about 25 mV. This happens due to opening of the fast Na channels that quickly depolarizes the membrane. This phase is called the *rapid upstroke*. When the transmembrane voltage is high, the myocyte is excited and can transmit excitation further through the gap junctions. Reaching the peak voltage is followed by closing of the Na channels and a small drop in the transmembrane potential. After that, the action potential comes to the *plateau phase*. This phase is specific to cardiomyocytes and is characterized by a steady transmembrane voltage. This is due to two types of ionic channels which act in the opposite directions. Namely, the depolarizing L-type Ca channels and the repolarizing slow delayed rectifying K channels. This phase ends with closing of the Ca channels and opening of extra K channels. The K channels bring the transmembrane voltage back to its resting state of -85 mV. After that, the Na channels recover and the myocyte is ready for the next excitation.

On the scale of the whole heart the excitation process occurs as the following. In the norm, the action potential is generated by the *sinus* node which consists of nodal cardiomyocytes. From the sinus node the action potential propagates through the top chambers of the heart—the *atria*. The bottom chambers—the *ventricles*—are electrically disconnected from the atria apart from one link: the *atrio-ventricular* node. In the atrio-ventricular (A-V) node the signal is slowed down which gives the atria time to contract. Afterwards, the signal propagates through the *His bundle* and then through *Purkinje fibers*. Finally, from the Purk-
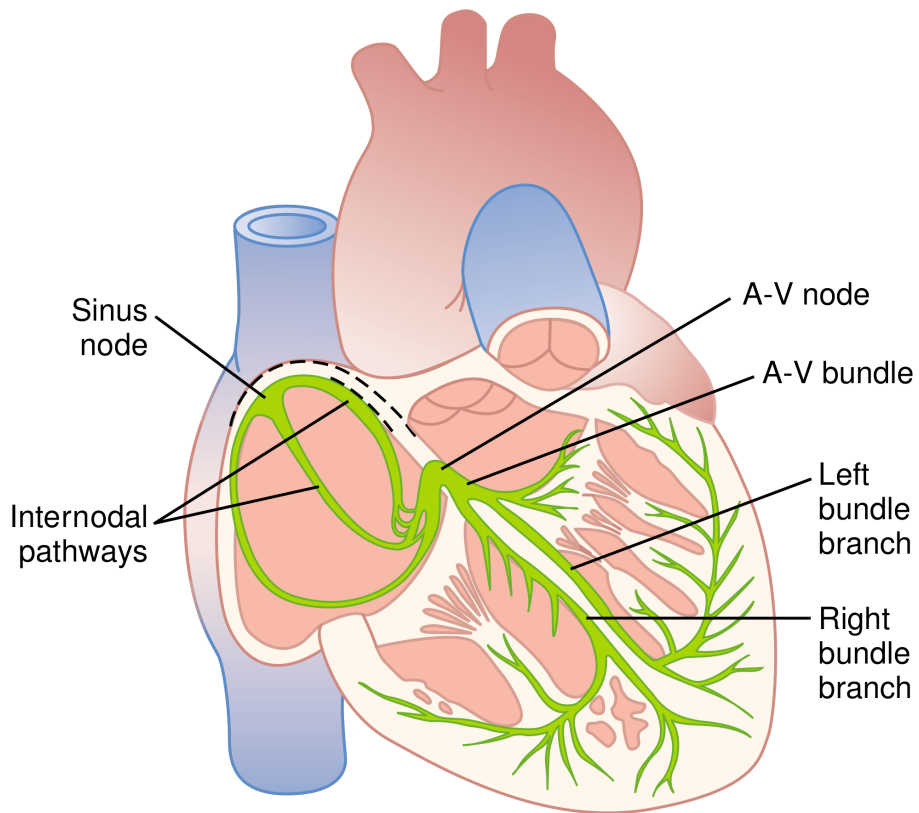
Figure 1.2. Conduction system of the heart. Taken from [1].

inje fibers the signal enters the inner layers (endocardium) of ventricles in a more or less synchronous fashion. Then, the signal propagates to the outer layers (epicardium) of the ventricles which is followed by contraction of the ventricles. The cardiac conduction system is shown in Fig. 1.2.

1.4   Theory of Excitable Media

In the previous sections we revealed that cardiac tissue is an excitable medium. This connection allows to exploit the profoundly developed theory of excitable media to describe the cardiac rhythm as well as its deviations. In this section we shall describe the focal points of this theory.

Investigations of signal propagation in cardiac tissue play two complementary roles in the theory of excitable media. On the one hand, several core results in the theory were discovered on cardiac systems. On the other hand, cardiac arrhythmias being arguably the most important application for the theory of excitable media stimulate research in all closely related fields.

One of the earliest quantitative result about the excitable media dates back to the middle of the 19th century. In 1850 Hermann Helmholtz measured the conduction velocity of an excitation wave in a frog nerve [2]. This measurement was possible because the pulse in active medium propagates with almost uniform velocity. A few decades afterwards, Helmholtz also measured the velocity of the excitation wave for a human nerve and described the threshold behavior for stimulation. In physiology, the threshold behavior was formulated as the *all-or-none* law by Henry Bowditch in 1871 for the contraction of cardiac muscle. This law states that on stimulation, one observes either the full response (e.g. propagating wave) or nothing. The strength of the stimulus is responsible solely for existence of the response but not for its characteristics.

First mathematical models of excitable media date from 1937. Kolmogorov, Petrovsky, and Piskunov [3], and in the same time Fisher [4] described a model (the KPPF model) for a trigger active medium in application to population dynamics. As it was mentioned, trigger systems are a suitable approximation for excitable systems provided one is interested exclusively in activation. The KPPF model was defined as a partial differential equation of a *reaction-diffusion* type. This model allowed to describe the propagation of trigger waves and the threshold phenomena in stimulation. Besides, the KPPF model allowed to determine that the conduction velocity scales as the square root of diffusion (connectivity) and as the square root of characteristic activation time. The beauty of the model lies in the fact that it accepts a complete analytical solution. Thus far, it is the only model with a continuous right hand side, for which the analytical solution is known to exist. Unfortunately, if the KPPF model is extended with an equation for recovery, it loses this feature.

Describing the recovery is crucial for certain effects. After one wave is passed
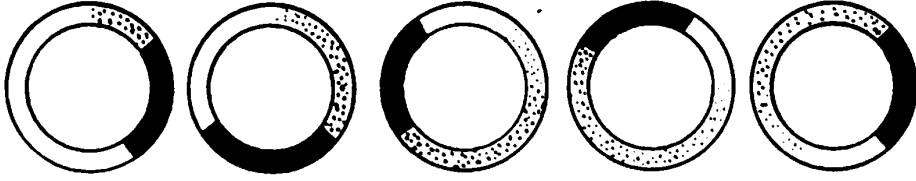
Figure 1.3. Schematic diagram of reentry activity. Taken from [5].

in an excitable medium, the medium recovers and gets ready for the next wave. The recovery time is determined by the duration of excited phase and of refractory phase. Consequently, there exists a minimal possible time interval between two subsequent stimulations. This property is called *refractoriness*. It is possible that more than one wave propagate simultaneously through the same excitable medium, provided that distance between any two waves is smaller than the minimal possible time interval multiplied by the conduction velocity. Furthermore, it is possible that one and the same wave just circulates in the excitable medium if this wave moves in a loop whose length is larger than the minimal possible time interval multiplied by the conduction velocity. This way, by the time the wave arrives to any element of the medium, that element has already been recovered from the previous activation, allowing the wave to propagate further. We have just described the most fascinating feature of excitable media which is called *reentry*.

Reentry has been known since at least the end of the 19th century [6]. In 1906 Alfred Mayer experimentally observed reentry in rings of jellyfish [7]. Later, in 1913, George Mines described the concept of reentry for cardiac tissue [5], the schematic presented in his paper is shown in Fig. 1.3. Reentry is not necessary due to a ring-shaped medium. If we increase the outer boundary of the circle in Fig. 1.3 *ad infinitum*, we effectively obtain a medium with a hole (an obstacle) inside. In this case the wave will be rotating around the obstacle, with the tip of the wave following the boundary of the obstacle and the rest of the wave propagating out of the obstacle. The wave will arrange itself into a spiral, and such patterns are referred to as *spiral waves* or, especially in cardiology, *rotors*. The period of reentry rotation in a ring or a spiral rotation around an obstacle is determined by the size of the ring or the size of the obstacle: with a smaller size the period is also smaller.

In mathematical models, reentry around an obstacle was first studied by Norbert Wiener and Arturo Rosenbloeth in application for cardiac and nerve tissue in 1946 [8]. Wiener and Rosenbloeth considered a phenomenological model of an excitable medium where an element was described as a finite automaton with three possible states: excited, refractory and recovered. An example of spiral waves presented in that work is given in Fig. 1.4. Wiener and Rosenbloeth
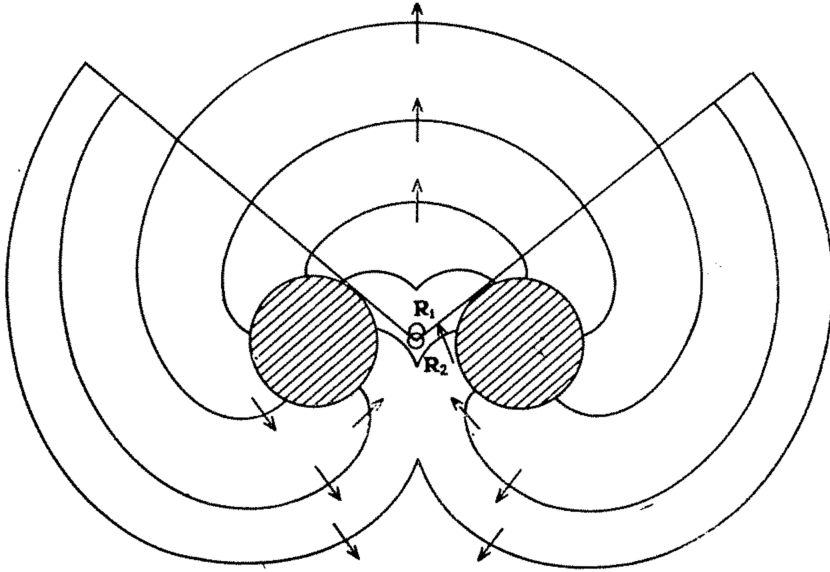
Figure 1.4. Spiral waves discovered by Wiener and Rosenbloeth. Taken from [8].

proved several theorems regarding formation of a spiral wave. They proved that one needs to deliver at least two stimuli to create a spiral wave. In cardiac physiology, it is currently known as the *S1S2 protocol*. They also proved that one needs an obstacle to support spiral rotation. Nowadays, we know that both statements are wrong, despite the proofs being absolutely correct. Spiral rotation without an obstacle was demonstrated in a follow-up study by Selfridge in 1948 [9]. He noted that the wave can circulate around itself forming an inexcitable *core* at the center of rotation. In this case, the period of the spiral wave is close to the minimal possible time interval for two subsequent stimuli. Later, in cardiac physiology, rotation around an obstacle was named *anatomical reentry* and the with no obstacle *functional reentry*.

Spiral waves are one of the cornersones of modern arrhythmia theory. A spiral wave is effectively an excitation source, that is an extra stimulation electrode if one talks about cardiac tissue.

Since the discovery of the spiral waves in mathematical models, their existence in cardiac systems has been shown for *in situ* heart preparations [10–12] as well as for *in vivo* monolayer cell cultures of cardiomyocytes [13, 14]. These discoveries are fairly recent, mostly in the 90es, when the reliable methods for mapping the transmembrane voltage in cardiac tissues became available. However, the properties of spiral waves and the mechanisms of their formation had been studied long before that time. This was possible due to the famous *Belousov-Zhabotinsky reaction*.
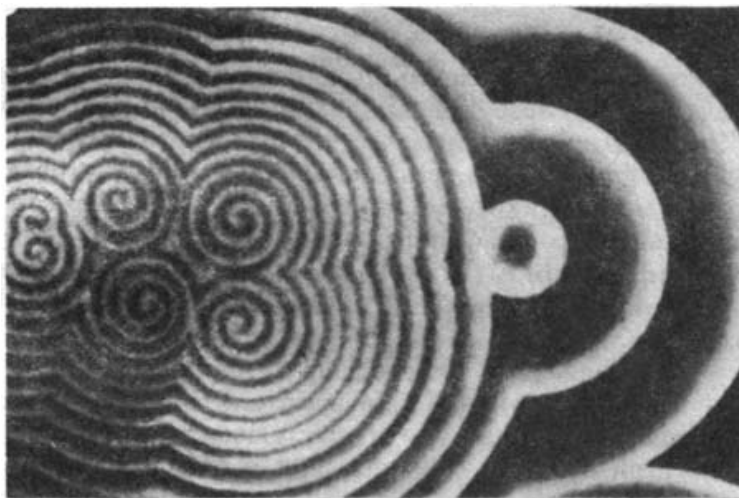
Figure 1.5. Spiral waves (left) capture the pacemaker (right) in the Belousov-Zhabotinsky reaction. Taken from [18].

The Belousov-Zhabotinsky (BZ) reaction was discovered by Boris Belousov around 1951. This reaction provides an example of an oscillating chemical process. The exact mechanism of the reaction is fairly sophisticated, with a couple of dozens intermediate reactions; however, the recipe and the fact that the reaction happens in a periodic fashion are well known. The work of Belousov was followed up by Anatol Zhabotisky who together with Albert Zaikin considered spatially distributed reaction in a thin layer in a Petry dish [15]. Immediately afterwards, existence of the spiral waves was reported for that set up by Arthur Winfree [16] and Zhabotisky [17] himself.

The BZ reaction gave the scientists of that time a perfect model for studying active media in general and spiral waves in particular. There were two reasons for that. On the one hand, the reaction is slow, with characteristic time of the order of minutes. The length of the wave fronts is large, of the order of millimeters. Therefore, the BZ reaction is very visual. On the other hand, the reaction is much easier to carry out in comparison, for instance, to biological experiments or clinical investigations. A thing one should keep in mind is that the results obtained on the BZ reaction should be applied to cardiac tissue with a bit of caution. This is because the BZ reaction is an oscillating active medium, whereas the cardiac tissue is an excitable medium. For some cases this difference is negligible. For example, if one studies spiral waves in excitable medium, then the excitable medium effectively becomes oscillating since any element of the medium spends almost no time in the recovery phase.

The BZ reaction was a genuine breakthrough for studying the active media.

In their original paper [15], Zaikin and Zhabotinsky discovered the generators of rhythm: the *pacemakers*. In 1982, Konstantin Agladze showed that the rhythm is captured by the fastest pacemaker. The same effect occurs in the heart where, in the norm, the cells of the SA node are the pacemakers. If these cells are not available anymore, slower cells of the AV node capture the rhythms. Should they be not available, slower Purkinje cells become in control. Another effect studied by Agladze was *overpacing*: capture of a pacemaker by a faster external stimulation. Nowadays, this effect is used for removing a spiral from cardiac tissue both in experiments and in clinics. A picture illustrating spiral waves, a pacemaker and the process of capturing is shown in Fig. 1.5.

With some modifications to the BZ reaction, its excitability can be controlled externally, by illuminating. This was used to study a *resonant drift*: moving of a spiral wave by applying periodic modulation of the medium. This effect was first predicted in kinematic models of spiral waves by Alexander Mikhailov and later studied on the BZ reaction in [19]. Resonant drift can be used for the same purpose as overpacing: removing a spiral wave from the medium.

The mechanisms of spiral wave formation have also been studied firstly on the BZ reaction [20]. One of the fundamental concepts discovered is the concept of *wavebreak*. An excitation wave can break on an obstacle or on local heterogeneity. In case of the BZ reaction, the wave can be broken "manually" by physically shaking a part of the wave front. It has been shown that if such a wavebreak is formed, it can result in formation of spiral waves provided the excitability of the medium is relatively low. These discoveries led to the concept of the *refractoriness heterogeneity* mechanism of arrhythmia induction [21]. The effects of heterogeneity are difficult to study with the BZ reaction, and most of the earliest results were obtained with mathematical models. Besides the aforementioned effect on promoting the wavebreaks, heterogeneity can govern the dynamics of spiral waves. In 1983, Rudenko and Panfilov showed that a gradient in heterogeneity causes a drift of spiral waves in a mathematical model of cardiac tissue [22].

Despite the significant progress done on the BZ reaction, there are several features of cardiac tissue and, in general, excitable media that cannot be captured by the BZ reaction. One of these features is the critical size for stimulation.

In 1937, William Rushton introduced a concept of "liminal length" for his mathematical model model of a nerve [23]. He described that a stimulation needs to have at least a certain length for raising an excitation wave. Fifteen years after that, in 1951, G. Markstein investigated a model of a trigger medium for flame propagation in two dimensions [24]. He derived that the velocity of propagation of a circular front decreases linearly with an increase in the radius of the front. Although these two effects may look different at the first glance, there is a deep connection between them. From the results of Markstein it follows that there is a limit radius when the velocity becomes zero. Zero velocity effectively means a propagation block. Therefore, a circular stimulation cannot raise an excitation wave if the radius of the stimulation is smaller than a certain critical radius.

The dependency of the conduction velocity on the radius of the circular wave fronts can be generalized on the fronts of any shape. In this case one introduces a concept of *curvature*—a measure how a particular front diverges from the plain front. For the plain front the curvature is zero and for a radial front the curvature is the inverse radius. Curvature can also be negative meaning that the front is concave. Using the concept of curvature, we can formulate the result mentioned above as: fronts with high curvature propagate slower and are less stable.

The dependence of the conduction velocity on the curvature of the wave front is known as the *sink-source mismatch* in cardiac physiology. The qualitative understanding for this effect is that an excited element of the medium can transmit its excitation to only a limited number of neighboring recovered elements. If the excited element tries to pass its excitation to a larger amount of recovered elements, the stimulation fades away and does not excite *any* neighbor. Thus, if an excitation wave propagates in a narrow pathway that starts to enlarge, the wave may be blocked. For cardiac tissue, this effect was first demonstrated in experiments of Cabo in 1994, who studied whether a wave can pass through a small isthmus *in situ* [25]. The most interesting effect that the sink-source mismatch can have on a wave propagation is breaking the propagation symmetry: if a wave emitted from some point A reaches some point B, it does not follow that the wave emitted from the point B will reach the point A. This is known as a *unidirectional block*. In case of the narrow pathways, the wave propagation is stable when the pathway narrows, but the wave can be blocked in the other direction when the pathways enlarges. Unidirectional blocks can be responsible for reentry formation: if we position a unidirectional block in a ring, a single stimulation near the position of the block will trigger reentry.

In this section we briefly reviewed the focal points of the theory of excitable media. Now we shall reformulate the main problem of cardiology—arrhythmia initialization—in terms of spiral waves in excitable media. This connection allows us to use a well established theory to partially reveal the answer to the main problem of the field: initialization of arrhythmia.

1.5 Cardiac Arrhythmia as Spiral Waves

Types of cardiac arrhythmias number in more than two dozens. The most dangerous types among them are arguably *tachycardia* and *fibrillation*. These types of arrhythmia are further subdivided by their location, where the most common cases are in the atria or in the ventricles. Tachycardia is characterized by a rapid activation rate with synchronous contraction. Fibrillation is also characterized by a rapid activation rate but with asynchronous contraction. Ventricular fibrillation is the most life-threatening arrhythmia: when the contraction of cardiac muscle in the ventricles is asynchronous, the net ejection volume is too small to support the demand of oxygen and nutrients. Ventricular tachycardia is

almost equally dangerous due to the ability of this arrhythmia to spontaneously turn into ventricular fibrillation. Atrial fibrillation is less dangerous since the only electrical link between the ventricle and the atria filters the high frequency atrial activation such as the ventricles can still contract reliably. However, chronic atrial fibrillation causes long-term structural remodeling of cardiac tissue and facilitates the development of more life-threatening arrhythmias.

There are two important features that relate tachycardia to spiral waves. First, tachycardia is driven by a pacemaker that is not the sinoatrial node, while a spiral wave is a persistent activity that can be considered as a pacemaker. Second, the frequency of activation during tachycardia is very fast, up to 4–5 Hz, while a spiral wave rotates with almost the maximal activation frequency possible in the medium. This relation allows suggesting that a spiral wave can be the main factor responsible for tachycardia. In a similar fashion, fibrillation can be explained by the presence of *multiple* spirals which effectively corresponds to a presence of multiple pacing sites, each with its own domain of influence. This makes activation asynchronous, resulting in the absence of proper contraction. There are several other hypotheses on the nature of tachycardia and fibrillation (e.g *ectopic beats*), but the mechanism due to spiral waves or reentry is arguably the most widely accepted nowadays.

Given the fact that the spiral waves are responsible for the life-threatening arrhythmia, the central problem of the cardiac electrophysiology can be reformulated in terms of excitable media: *what leads to formation of spiral waves?*

In the previous section we considered several possible scenarios for a spiral wave to be triggered: the S1S2 protocol, wavebreaks due to heterogeneity, and unidirectional blocks. Now we shall describe physiological conditions where these scenarios become possible.

The S1S2 protocol or *cross-field stimulation* is a widespread method for inducing spirals in experiments and in numerical simulations. However, in the norm, there is a limited possibility that an extra S2 pulse occurs since the natural pacemakers do not generate such rapid rhythms. Nevertheless, under a presence of a pathology named *early after depolarization* the cardiac action potential has an extra bump after the plateau phase. This extra bump can potentially trigger the S2 stimulation which results in formation of a spiral wave. Conditions when it is possible are subject of intensive studies nowadays.

The appearance of the wave breaks due to tissue heterogeneity is often considered to be the main mechanism for spiral formation. Heterogeneous tissue has different refractory period at different sites. If the tissue is stimulated with a high frequency then it is possible that the regions with longer refractory periods do not have sufficient time to recover which leads to formation of the wave breaks. This high frequency pacing is referred to as the *burst pacing* protocol. This protocol is used predominantly in clinical studies to induce ventricular tachycardia.

The heart possesses intrinsic heterogeneity, for example, the cells of ventric-

ular endocardium have longer refractory period than the cells of ventricular epi-cardium. However, in the norm, this heterogeneity does not trigger the forma-tion of spiral waves. Several pathological conditions, such as *ischemia*, *infarction* or *fibrosis* can both enhance the natural heterogeneity and create effective obsta-cles or regions with long refractory periods.

Ischemia is a lack of proper blood supply to the tissue. This can happen be-cause of occlusion of the artery perfusing the heart (*coronary artery*). Ischemia results in changing of the properties of cellular ionic channels. Infarction is a partial death of tissue caused by a shortage of blood supply that can occur as a result of ischemia. The dead muscle tissue promotes activation of structural cells—*fibroblasts*—which replace the dead tissue with connective tissue forming an inexcitable scar. Fibrosis is a state characterized by formation of excess con-nective tissue and increased population of fibroblasts. This leads to structural and ionic remodeling of the cardiac tissue. All these effects are interconnected and all of them can potentially result in arrhythmia triggering [26, 27].

The unidirectional block also does not happen in the norm since there are no narrow pathways that are responsible for this effect. However, in the presence of infarction and fibrosis, the narrow passes can be formed inside the scars or in the border zone of the scars [28, 29]. Besides forming the narrow passes fibrosis contributes to slowing down the conduction, further facilitating the sink-source mismatch effect. This can result in formation of a unidirectional block [30].

1.6 Pathological Conditions

From the previous section one can conclude that such cardiac arrhythmias as tachycardia and fibrillation are rare events that almost never happen under normal conditions. Indeed, if the life expectancy is about 70 years the heart is ca-pable of performing more than 2 billion beats with triggering no life-threatening arrhythmia. Therefore, if arrhythmia is not related to congenital defects it is as-sociated with pathological conditions.

Pathological conditions by themselves are the consequence of failure in adap-tation. A universal property of living beings is *homeostasis*, that is an ability to maintain a system at equilibrium under changing external environment. This ability is present at all levels of organization of living matter. Homeostasis is implemented as set of negative feedback mechanisms and compensatory reac-tions. For instance, under ischemia conditions, the ratio of ATP to ADP in a cell remains remarkably constant for the first few minutes despite the lack of oxygen and nutrition components. One of the regulatory mechanism to maintain the constant ratio is activation of anaerobic glycolysis. The glycolytic pathways are activated via at least three different enzymes that sense the drop in the ratio of ATP to ADP concentrations [26].

However, the compensatory mechanisms are often unable to function over a

longer time scale. In the example with cellular ischemia, the activation of gly-colytic pathways leads to increase in concentration of lactic acid which deacti-vates glycolysis unless washed out. Moreover, the compensatory mechanisms can have a positive feedback on the effects that trigger them. For instance, under ischemia conditions, the ATP synthase (which produces ATP in the norm) can consume ATP to restore the mitochondrial transmembrane potential, which re-sults in further decrease in the ratio of ATP to ADP concentrations. Positive feed-back leads to loss of stability of the given state and to a rapid self-accelerating transition to a new state. Ischemia eventually leads to death of the cells, how-ever, the final state may be the death of the organism due to triggering a lethal arrhythmia. This lethal arrhythmia is the final manifestation of failure in adap-tation.

Regarding this connection, it is possible to explain why lethal arrhythmias are sudden. When the stability of a state is lost, the transition to a new state happens with self-amplifying, catastrophic rate. Often, the pathological condi-tion that triggered an arrhythmia is amplified in the presence of the arrhythmia. For instance, if a ventricular fibrillation is triggered by ischemia, it leads to a secondary ischemia since the heart is unable to pump the blood properly. Such positive feedback is also presented for chronic arrhythmias like atrial fibrillation. For instance, it is difficult to determine whether atrial fibrillation is the cause or the effect of ionic remodeling [31, 32].

To sum up, cardiac arrhythmias should only be considered in connection with pathology. In this thesis we focus on the effects of two pathological states that are known to cause acute cardiac arrhythmias: fibrosis and ischemia.

1.7 Mathematical Models in Cardiac Physiology

Creating models is an intrinsic property of intelligence. The process of per-ception, cognition, memory, making decisions, communication, and problem solving implies operating with models. A model of a system is another sys-tem that is analogical to the prototype. By analogical, we mean that the model shares some features of the prototype and lacks some other features. In a more narrow sense, a model is defined as an analogy that is both (a) simpler than the prototype and (b) allows to investigate the features of the prototype that we are interested in.

A mathematical model is a description of a system in terms of abstract con-cepts, such as state and transitions between states. Modern mathematical mod-els are usually (but not always) formulated in terms of *differential equations*. A system of differential equations is a description of how change of the state of the system depends on the state of the system. A mathematical model of a particular system can be based on already known physical laws (e.g. Maxwell's equations for the electromagnetic field), or based on known experimental data. In the latter
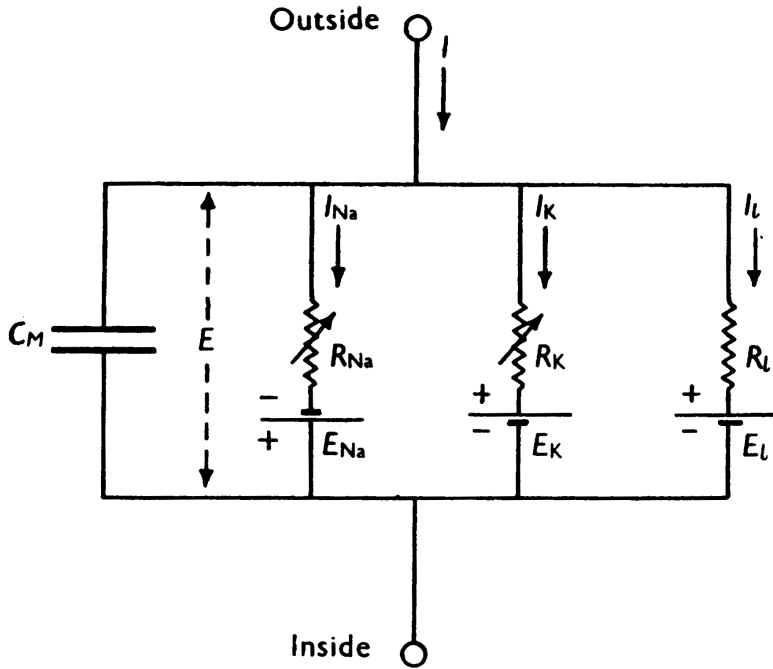
Figure 1.6. Electrical circuit representing the membrane in the Hodgkin-Huxley model. Taken from [33].

case the model is called *phemenological*.

The modern approach for building electrophysiological models was established by Alan Hodgkin and Andrew Huxley in 1952. In their work [33] they used a semi-phemenological approach to describe the kinetics of Na and K channels for a squid giant axon. In the Hodgkin-Huxley model the membrane with ionic channels is represented as an electrical circuit with a capacitor (the membrane) and active elements consisting of rheostats and seats of electromotive force (emfs), which correspond to the ionic currents. This circuit is shown in Fig. 1.6. Each emf corresponds to the *reversal* potential of a particular ionic current which is determined by the concentration ratio between the intracellular and the extracellular compartments. The resistance of the rheostats is determined by phemenological dynamics. The Hodgkin-Huxley model allowed to quantitatively describe the action potential generation as a reply to external stimulation and transition to oscillatory behavior as a result of a large constant external current injection. Spatially distributed Hodgkin-Huxley systems allowed to describe propagation of the action potential.

The Hodgkin-Huxley model is a nonlinear model with 4 state variables, which

makes its analytic analysis quite difficult. In 1961 Richard FitzHugh presented a two-variable simplification of the Hodgkin-Huxley model [34], and a year later Jinichi Nagumo published an equivalent electrical circuit [35]. The FitzHugh-Nagumo model captured all the qualitative features of the Hodgkin-Huxley model being much simpler for both analytic investigation and performing simulations with analogous computers that existed that time.

With the advance of digital electronics the advantage of being easy to perform simulations had rapidly become less relevant. Evolution of computational electrophysiology did not take the path of development simplified phemenological models that capture only the necessary effects. Instead, the subsequent models tried to archive the goal of including as many physiological details as possible. The first generation of cardiac electrophysiology models are direct offspring of the Hodgkin-Huxley model, with the parameters tuned to reproduce the shape of the cardiac action potential [36–38]. This approach had an issue that it was necessary to introduce either a very complex kinetics for the Na current or a second Na current to describe the plateau phase of the action potential. As it was discovered later, there is another inward current, namely the Ca L-type current, that is responsible for the plateau phase.

The next generation of cardiac electrophysiology models include the formulation of calcium currents as well as ionic exchangers and pumps. The Ca^{2+} dynamics turned out to be much more complex than the dynamics of Na^+ and K^+. The reason for that is that Ca^{2+} concentration inside the cell changes by orders of magnitude during generation of the action potential. This huge change is due to the presence of internal Ca store that gets released upon external Ca injection. The first model that include a simplified Ca dynamics was by DiFrancesco and Noble in 1985. A famous descent of this model that captures a more precise formulation of Ca dynamics that also includes buffering is the LR2 model by Luo and Rudy [39]. A further improvement was archived by ten Tusscher and Panfilov who incorporated new physiological data and eliminated several artificial dependences in the LR2 [40, 41]. In this thesis the model of ten Tusscher and Panfilov (the TNNP model) is used as the primary method of investigation of cardiac arrhythmias.

Creation of the Hodgkin-Huxley model was the greatest advance of computational biophysics. This model predefined the direction of development of mathematical models in neural and cardiac electrophysiology for at least the next 60 years. The modern development trends include incorporating more geometry and metabolism details to the models, eliminating the level of phenomenology in the dynamics of ionic channels by Markov chains, and creation of patient-specific models from the clinical data.

Currently, there are more than hundred models of cardiac cells designed for different species and for different cell types. There are at least two dozens published models that one can use to describe human ventricular cardiomyocytes. The difference between these models lies in the amount of details the models

try to capture, or in the other words, in the complexity of the models. The complexity of a model can be roughly estimated by the number of the state variables the model has. For example, a one-variable model (e.g. the KPPF model) can describe the propagation of excitation, but will fail to describe recovery. A two-variable model (e.g. the FitzHugh-Nagumo model) can also describe recovery but will fail to reproduce the shape of the action potential. The shape of the action potential can be reproduced with models of a larger amount of the state variables but these models would fail to describe dynamics of a particular ionic current. Therefore, having more variables potentially allows us to describe the system more precisely. On the other hand, with increasing amount of details one loses a property of being general, that is applicable to a broad class of phenomena. For instance, the effect of curvature on propagation velocity is described by the KPPF model, and is applicable to any reaction-diffusion system, not only cardiac tissue.

Models with larger number of the state variables often contain larger number of parameters, which impacts the stability of the model with respect to small changes of the parameters. This is known as "overfitting", when a model lacks predictive power but describes the phenomena that it was fitted for perfectly. In addition, models with larger number of the state variables also complicate both analytic and numerical analysis. An ideal model for a particular effect would contain the things that are important for this effect and nothing else. In practice, it is often difficult to highlight the important features, especially if one tries to describe the process of arrhythmia formation. Arrhythmia formation is a transient process which means it is easier to capture by having many state variables, since it makes the model more susceptible to noise. Removing of a single component might stabilize the model which would result in the absence of arrhythmia. In this light, one needs some general models designed with many details.

The TNNP model used in this thesis is known to reproduce the shape of the action potential, the dependency of the action potential duration on the stimulation frequency and the dynamics of most of the known ionic currents.

1.8   Thesis Outline

This thesis is dedicated to investigation of the effects of several pathological conditions on the onset of arrhythmia, dynamics of arrhythmia, and methods of prevention and termination of arrhythmia. We use the TNNP mathematical model of ventricular tissue and numerical methods for solving the partial differential equations given by this model.

In **chapter 2** we study the impact of global cardiac ischemia on dynamics of ventricular fibrillation. As it was mentioned, global ischemia always accompanies ventricular fibrillation and also can serve as a trigger for this condition. We show that global ischemia makes arrhythmia more stable and persistent, but on

the other hand it prevents new arrhythmia source from emerging. We analyze the effect of global ischemia on the period of the activation pattern and the number of arrhythmia source, and make estimation on how ischemia develops in the first few minutes based on a clinical data.

In **chapter 3** we investigate the effect of another pathological condition: fibrosis. Fibrosis is known to be a pro-arrhythmic factor but the exact mechanisms for arrhythmia formation and the methods of preventing the arrhythmia are still under extensive research. We study the effect of heterogeneity in fibrosis distribution with respect of these two questions. We show that a tissue with heterogeneous fibrosis layout is more susceptible for arrhythmia triggering. We describe the types of the resulting arrhythmia and provide an insight of how ablation therapy can be used for termination of arrhythmia. We show what determines the period of the activation pattern, and demonstrate a correlation of the positions of the rotors with a particular fibrosis layout.

In **chapter 4** we propose a rule-based approach for determining of fiber orientation for the left human ventricle from MRI data on geometry of the left ventricle for a patient. We designed this approach for creating patient specific models that we used in **chapter 5**. The fiber orientation is crucial for matching the results of simulations with the clinical data.

In **chapter 5** we perform a detailed study that reveals the mechanism of the correlation between the positions of the arrhythmia sources and tissue architecture that we introduce in **chapter 3**. We describe how an arrhythmia source gets attracted by a region with higher fibrosis levels. We provide the conditions for this effect to occur. Using the patient specific models that we introduce in **chapter 4**, we describe the same effects for physiological fibrosis layout. We characterize the effect of attraction in terms of ECG and provide clinical data where this effect can take place. In addition, we describe a link between the attraction effect and the impact of the fibrosis border zone in clinics.

Finally, in **chapter 6** we summarize the results.

Chapter 2

Effect of Global Cardiac Ischemia on Human Ventricular Fibrillation

Ivan V. Kazbanov[1], Richard H. Clayton[2,3], Martyn P. Nash[4,5], Chris P. Bradley[4], David J. Paterson[6], Martin P. Hayward[7], Peter Taggart[7], and Alexander V. Panfilov[1]

[1]Department of Physics and Astronomy, Ghent University, Belgium
[2]INSIGNEO Institute for In-Silico Medicine, University of Sheffield, UK
[3]Department of Computer Science, University of Sheffield, UK [4]Auckland Bioengineering Institute, University of Auckland, New Zealand
[5]Department of Engineering Science, University of Auckland, New Zealand
[6]Department of Physiology, Anatomy and Genetics, University of Oxford, UK
[7]Departments of Cardiology and Cardiothoracic Surgery, University College Hospital, London, UK

Abstract

Acute regional ischemia in the heart can lead to cardiac arrhythmias such as ventricular fibrillation (VF), which in turn compromise cardiac output and result in secondary global cardiac ischemia. The secondary ischemia may influence the underlying arrhythmia mechanism. A recent clinical study documents the effect of global cardiac ischaemia on the mechanisms of VF. During 150 seconds of global ischemia the dominant frequency of activation decreased, while after reperfusion it increased rapidly. At the same time the complexity of epicardial excitation, measured as the number of epicardical phase singularity points, remained approximately constant during ischemia.

Here we perform numerical studies based on these clinical data and propose explanations for the observed dynamics of the period and complexity of activation patterns. In particular, we study the effects on ischemia in pseudo-1D and 2D cardiac tissue models as well as in an anatomically accurate model of human heart ventricles.

We demonstrate that the fall of dominant frequency in VF during secondary ischemia can be explained by an increase in extracellular potassium, while the increase during reperfusion is consistent with washout of potassium and continued activation of the ATP-dependent potassium channels. We also suggest that memory effects are responsible for the observed complexity dynamics. In addition, we present unpublished clinical results of individual patient recordings and propose a way of estimating extracellular potassium and activation of ATP-dependent potassium channels from these measurements.

Author Summary

Cardiac arrhythmias are an important cause of death in the industrialized world. The most dangerous type of cardiac arrhythmias is ventricular fibrillation. If left untreated, it leads to death within just few minutes. In most of the cases ventricular fibrillation occurs as a result of cardiac ischemia, which is a shortage of blood supply to the heart muscle. Furthermore ventricular fibrillation leads to decreased cardiac output, which in turn results in secondary ischemia. A recent clinical study investigated the effect of secondary ischemia on the organization of ventricular fibrillation in the human heart. However, in the clinical study it was not possible to obtain the whole picture of activation of the heart and to separate the relative roles of different processes induced by ischemia in the alterations to the cardiac electrical activity. In this study we use computer modeling to address these problems and to complement the results of the clinical study. Our results allow us to explain the change of electrical activation pattern in the heart during the first minutes of ischemia and to estimate the relative rates of those ischemia-induced physiological processes. We also present previously

unpublished data on individual patient recordings from the clinical study.

2.1   Introduction

The heart is an electromechanical pump, where contraction is triggered and synchronized by electrical activation originating from the sinoatrial node. Abnormal initiation or conduction of the electrical impulses could result in a cardiac arrhythmia. Cardiac arrhythmias are an important cause of sudden and premature death in the industrialized world. In many cases the lethal event is ventricular fibrillation (VF). During VF, rapid and self-sustaining electrical activity in the ventricles acts to suppress the natural pacemaker, resulting in uncoordinated, weak and rapid contractions, which lead to death within several minutes [42].

VF often occurs as a result of acute regional cardiac ischemia, which is a condition when blood flow to part of the heart is substantially decreased, for example by reduced flow through a coronary artery [43]. In addition, global ischemia unavoidably accompanies VF, because the abrupt fall in cardiac output resulting from VF also results in compromised myocardial perfusion. Thus an episode of spontaneous VF will result in a progressively ischemic heart. The effect of this secondary ischemia on electrical activity during VF is important clinically, because defibrillation typically occurs several minutes after the onset of VF, and thus the mechanism is likely to have been modified by ischemia [44, 45].

It is known that ischemia profoundly affects the electrophysiological properties of cardiac cells and tissue [26]. During VF, the rapidly changing patterns of electrical activity in the ventricles are sustained by re-entry, in which waves of electrical activation continually propagate into regions of recovered tissue [46]. Re-entry is seen as a spiral wave on the surface of the heart, and a scroll shaped activation wave in 3D cardiac tissue [47]. The question of how ischemia influences the behaviour of re-entrant activity during VF is important, and has been addressed by clinical, experimental and modeling studies.

Two important characteristics of VF are the frequency and spatiotemporal complexity of activation patterns, and these have been studied in animal heart experiments. Experiments on canine hearts [46] have shown that both activation rate and pattern complexity (measured as the number of wave fronts) increase slightly during the first minute of VF, followed by a decrease over periods of up to 10 minutes, associated with progressive global cardiac ischemia. Studies in porcine hearts, [48], demonstrated a monotonic decrease of the activation rate of VF during the first 5 minutes of ischemia, with a decrease in complexity for the first two minutes followed by a rapid increase.

In spite of the significance of these animal studies, the most valuable question for clinical practice is how global ischemia modulates the mechanism of VF in the human heart. Both clinical and modelling studies have established that the organization of VF in the human heart is quantitatively different to that in canine and

porcine hearts [49, 50], with VF in the human heart shown to be characterized by a much lower VF complexity compared with animal hearts of similar size. For this reason, experimental studies on human hearts are extremely important for understanding underlying mechanisms. Recently this gap has partially been filled by studies in isolated myopathic hearts [51, 52], and studies in the in-situ human heart [53].

In the in-situ study [53], electrical activity was mapped on the heart surface during VF in ten patients undergoing routine cardiac surgery with cross-clamp fibrillation. Following the commencement of cardiopulmonary bypass to support the systemic circulation, the following protocol was used: (1) VF was induced by burst pacing, (2) after 30 s, global cardiac ischemia was initiated by applying an aortic cross-clamp, (3) after 2.5 min. ischemia, cardiac perfusion was restored by release of the cross-clamp, (4) recording continued for 30 s during reperfusion. During all 3.5 minutes of VF, electrical activity was recorded using 256 unipolar electrodes sewn into an elasticated sock placed over the entire ventricular epicardium by the surgeon. Consistent with studies in animal hearts, the activation rate of fibrillation gradually decreased during global ischemia and increased abruptly after reperfusion. In contrast with animal hearts, the complexity of fibrillation patterns (measured as the number of phase singularities) continued to increase gradually during ischemia, although the data showed large variation.

The above mentioned study [53] had several important limitations, in common with other studies in human and animal hearts. First, electrical activity was recorded only on the epicardial surface, whereas electrical activation patterns in the ventricles are 3-dimensional. Second, ischemia is a complex process which involves several separate mechanisms including hyperkalemia, hypoxia and acidosis, and each of these components has its own time course in ischemia [26]. However, it is not generally possible to measure the relative contribution of these individual components to the excitation patterns *in vivo*.

Because it is difficult to measure all of the quantities of interest, even in animal hearts and tissue, detailed mechanistic and multi-scale models of cardiac electrophysiology at cell, tissue, and whole organ scales are becoming important research tools for the study of arrhythmia mechanisms. It was shown previously that the combination of modeling with experimental and clinical studies can provide valuable insights into arrhythmia mechanisms [49, 50, 54].

In this paper, we describe a detailed and comprehensive modeling study, which seeks to establish mechanisms that are consistent with the changes in activation patterns observed during VF in the human heart with global ischemia [53]. In addition, we present previously unpublished clinical results from [53], namely the changes in dominant frequency (DF) for individual patients. The model we use is a representation of human ventricular tissue, with cellular electrophysiology described by the TNNP06 model [41]. This model was adapted to enable us to investigate the effects on VF of three components of ischemia [26] both

separately and in combination. Briefly the effects of these three components on the eletrophysiological processes can be characterized as follows. Hyperkalemia is elevation of the extracellular potassium concentration, which leads to a shift of the resting potential of cardiac cells. Acidosis is an increase in intracellular pH, which results in smaller fast sodium and L-type calcium currents during depolarization. Hypoxia is a reduced oxygen supply, which impairs cellular metabolism and changes the ratio of ADP to ATP concentration inside the cell. In turn, this change results in the opening of specific ATP-dependent potassium channels. To describe them in our simulations, we developed a new model of the human K_{ATP} channel based on experimental data from human cardiac cells [55].

We first determined the effect of each of the three components of ischemia on action potential duration (APD) and conduction velocity (CV) restitution in 1D models, along with the effects on re-entry in 2D models. Then we performed simulations of VF using a 3D anatomical model of the human ventricles [50], where the dependency of the activation rate of VF on each component of ischemia was determined.

Next, we used these dependencies to interpret the clinical recordings for individual patients. We showed that the predominant factor responsible for the change in activation rate during ischemia is hyperkalemia, and estimated the magnitude of this effect in each individual patient recording. Then we studied how the three ischemic components affect the complexity of VF expressed by the number of scroll wave filaments. Although there was a big variation, the results we obtained were qualitatively similar to the clinical recordings and we concluded that the main factors important for the observed dynamics were memory effects. We also proposed a simple algorithm to estimate the dynamics of hyperkalemia and the activation of the K_{ATP} current using individual patient recordings. Overall, we demonstrated that taking into account the electrophysiological changes caused by hyperkalemia and hypoxia, the results of [53] can be fully explained, indicating that acidosis has only a minor effect on VF activation during the first few minutes of ischemia.

2.2 Methods

2.2.1 Electrophysiological Model

Cardiac cellular electrophysiology was modeled using the TP06 model of human ventricular cardiomyocyte [41, 56] coupled into a monodomain model for cardiac tissue. In this model the main equation determining the propagation of transmembrane voltage is given by:

$$\frac{\partial V}{\partial t} = \sum_{i,j} \frac{\partial}{\partial x_j} \left(D_{ij} \frac{\partial V}{\partial x_i} \right) - I_{\text{ion}}(V, \ldots) \tag{2.1}$$

where V is transmembrane voltage, D_{ij} a diffusion tensor and I_{ion} is the sum of ionic currents:

$$I_{\text{ion}} = I_{\text{Na}} + I_{\text{K1}} + I_{\text{to}} + I_{\text{Kr}} + I_{\text{Ks}} + I_{\text{CaL}} + I_{\text{NaCa}} + I_{\text{NaK}} + I_{\text{pCa}} + I_{\text{pK}} + I_{\text{bCa}} + I_{\text{bNa}} + I_{\text{KATP}}$$

$$(2.2)$$

where all currents except I_{KATP} were described by the equations from [40, 41], and I_{KATP} was a new current that we introduced to take the effects of hypoxia into account. For most parameters we used the values listed in Table 1 and Table 2 of [41] corresponding to epicardial cells. For the five parameters listed in Table 2 of [41] we used the values corresponding to "Slope 1.8" for 3D simulations, and "Slope 1.1" in 2D simulations for finding the restitution curves. We used parameters corresponding to all three different slopes: 1.1, 1.4 and 1.8, for analyzing the stability of re-entry in 2D.

Ischemia was introduced to the model by changing the parameters corresponding to each of the three ischemia components described above. To model hyperkalemia we varied $[\text{K}^+]_\text{o}$ in the range 5–10 mM. Acidosis was taken into account by decreasing the maximum conductivity of sodium and L-type calcium currents within the limits of 20–100%. The effect of hypoxia was represented by a novel description of the ATP dependent potassium current in the human heart.

Table 2.1 summarizes the changes to the TP06 model due to ischemia.

2.2.2 ATP-dependent Potassium Current

We developed our model of the I_{KATP} current based on the results of *in vitro* experiments [55]. Fig. 2.1 shows measured current-voltage dependencies of I_{KATP} for two different extracellular potassium concentrations. We fitted these data using functions with a power dependency on $[\text{K}^+]_\text{o}$ concentration and exponential functions of voltage, similar to functions used in [57, 58] for I_{KATP}. Our expression for human I_{KATP} was:

$$I_{\text{KATP}} = G_{\text{KATP}} f_{\text{ATP}} \left(\frac{[\text{K}^+]_\text{o}}{5.4} \right)^{0.3} \frac{1}{40 + 3.5 e^{0.025V}} (V - E_{\text{K}}) \qquad (2.3)$$

where $[\text{K}^+]_\text{o}$ is in mM, V is transmembrane voltage measured in mV, and E_{K} is the Nernst potential for potassium also in mV. Our function reproduces well the current-voltage dependency in a range between -80 and 40 mV. We also see some small deviations for lower and higher values of voltage, which, however, should not be essential as they are outside the important physiological range.

The fraction of open I_{KATP} channels (or the probability for a channel to be open) is expressed by the factor f_{ATP}. It depends on the energy capabilities of the cell. For our model we left this dependency unspecified, changing the value f_{ATP} directly to induce hypoxia. The scaling coefficient G_{KATP} was fitted following the approach of [58], where the value of APD decreases twofold if $f_{\text{APT}} = 0.55\%$ of
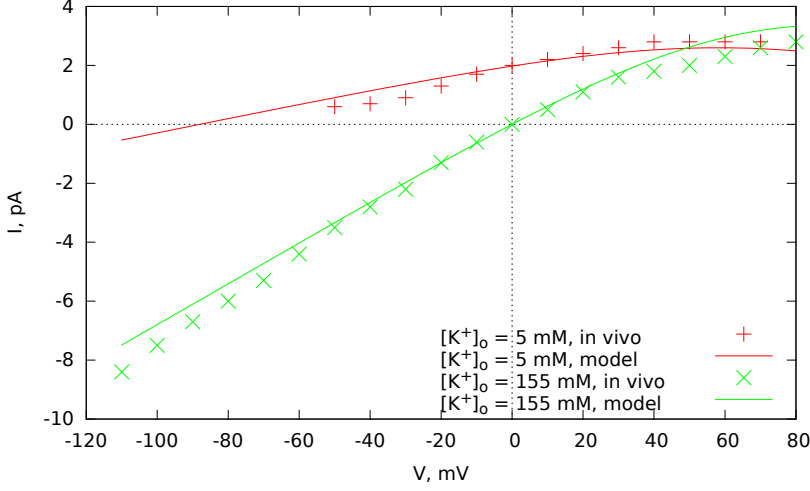
Figure 2.1. Current-voltage dependency for the K_{ATP}^+ current in our model. The experimental data is from [55].

Ischemia component	Modeled by	Within range
Hyperkalemia	$[K^+]_o$	5–12 mM
Acidosis	G_{Na}, G_{CaL}	20–100% of base values
Hypoxia	f_{ATP}	0–0.05%

Table 2.1. Summary of changes applied to the TNNP06 model.

channels are open, which led to $G_{\text{KATP}} = 155$ nS/pF.

2.2.3 Numerical Methods

For 1D and 2D simulations we solved equation (5.1) for homogeneous and isotropic tissue with the diffusion tensor $D_{ij} = D_l \delta_{ij}$ where D_l was taken to be 1.54 cm^2/s and δ_{ij} is the Kronecker delta. For these parameter values, the velocity of propagating plane waves at a stimulation frequency of 1 Hz was 72 cm/s.

For 3D whole heart simulations we used an anatomically based model of human ventricles presented in [59]. This model takes anisotropy into account by reconstructing the fiber direction field described in [60] and assuming that the diffusion coefficient across (transverse) the fibers D_t is 4 times less than the diffusion coefficient along fibers D_l, which was set to 1.54 cm^2/s. For 3D simulations the components of the diffusion tensor were given by:

$$D_{ij} = (D_l - D_t)\tau_i \tau_j + D_t \delta_{ij}$$

37

where τ_i are the coordinates of a normalized vector oriented along the fibers.

For all types of the media we used 'no flux' boundary conditions:

$$\sum_{i,j} n_i D_{ij} \frac{\partial V}{\partial x_i} = 0$$

where n_i are the coordinates of a vector that is normal to the boundary.

To solve the differential equations we used a finite difference approach. For both 2D and 3D simulations we introduced a rectangular mesh of about one million points. To approximate the diffusion term we used a stencil of 5 grid points for 2D and 19 points for 3D. We used an explicit first order Euler method to solve the discretized system, which for 2D tissue was:

$$\frac{\tilde{V}_{ij} - V_{ij}}{\tau} = \frac{1}{h^2} \sum_{i'j'} w^{ij}_{i'j'} V_{i+i',j+j'} - I_{\mathrm{ion}}\left(V_{ij}, \dots\right) \tag{2.4}$$

where the time step $\tau = 0.02$ ms, h was the space step, and $w^{ij}_{i'j'}$ weights corresponding to the diffusion tensor at location i, j. The space step was 0.25 mm for 2D simulations, and 0.5 mm for 3D simulations [61]. The gating variables in the TP06 model were integrated using the Rush and Larsen approach [62]. To cache the results returned by functions that were only voltage dependent we used pre-computed look-up tables.

The model was implemented using the C and C++ programming languages with OpenMP extensions for parallelization. We mainly used the Intel ICC compiler toolkit. The code for 2D was run on an Intel Core i7-3930K (3.20 GHz) machine, and the 3D code for human ventricles was run on dual-processor Intel Xeon E5-2650 (2.0 GHz) machines.

2.3 Results

2.3.1 APD and CV Restitution

In a model of a thin strip of human cardiac tissue, we studied how the different components of ischemia influence APD and CV restitution, a dynamic property of cardiac tissue important for the onset of re-entry and for the stability of re-entrant waves [63, 64]. We followed the same approach as in [54], but with a different formulation of I_{KATP}.

Restitution and dispersion curves were obtained using an S1S2 protocol, in a 10×2.5 cm sheet of 2D simulated tissue. Superthreshold stimuli were delivered along one short edge of the sheet, and measurements of APD were made at a distance of 2.5 cm from the stimulated edge. The basic cycle length (BCL) for S1 stimuli was 1000 ms. The ten S1 stimuli were followed by a single S2 stim-

ulus. The duration between the last S1 and S2 was decremented from 1000 ms until there was no response to the S2 stimulus at the point of measurement. The restitution curves are shown in Fig. 2.2.

In Fig. 2.2A the effect of hyperkalemia on APD restitution is shown, indicating that APD decreases with increasing $[K^+]_o$. This effect is due to I_{K1} and I_{Kr} currents, which depend directly on $[K^+]_o$ and become larger once $[K^+]_o$ is increased, accelerating the repolarization process. The effect of hyperkalemia on conduction velocity is shown in Fig. 2.2D. We see that the conduction velocity decreases with increasing $[K^+]_o$. This is because an increase in $[K^+]_o$ shifts the resting potential to more positive values suppressing the sodium current and, consequently, reducing the excitability of the cell.

Fig. 2.2A and Fig. 2.2D also show how the minimal APD—APD_{min}—value (the left most point of the restitution curve) depends on $[K^+]_o$. APD_{min} increases substantially with hyperkalemia. This fact can be important as APD_{min} is considered as one of the main factors determining the complexity of pattern of excitation during fibrillation [59, 65].

Fig. 2.2B and Fig. 2.2E illustrate the effect of acidosis (modeled as reduction of I_{Na} and I_{CaL}) on APD and CV restitution. Both APD and CV decrease with acidosis, because acidosis diminishes the depolarizing currents available to the cell. However, the value of the APD_{min} showed almost no dependency on acidosis, unless the conductance of the I_{Na} and I_{CaL} channels was reduced to 20% of their default values.

Fig. 2.2C and Fig. 2.2F show the effect of hypoxia, modeled as activation of I_{KATP}. Both APD and APD_{min} become substantially shorter since hypoxia activates a strong depolarizing current. The value of CV showed almost no dependency on hypoxia because hypoxia does not affect I_{Na}.

Fig. 2.2 shows that each component of ischemia acted to reduce the slope of restitution. Steep restitution is considered as one of the main mechanisms contributing to the breakup of re-entry in VF [63, 64]. According to the restitution hypothesis, flattening restitution prevents possible spiral wave breaks from happening, and therefore prevents formation of new arrhythmia sources.

2.3.2 Effect of Ischemia on Arrhythmia Sources in 2D

We studied how the different components of ischemia influence the dynamics and stability of re-entrant waves in 2D—spiral waves. In these simulations we varied the slope of the restitution curve for non ischemic conditions by changing five parameters of our model, as described in the Methods. We used three different sets of parameters, which correspond to a slope of 1.1, 1.4 and 1.8 under normal conditions. For initiation of a spiral we used an S1S2 protocol: at first, the S1 stimulus was delivered along one side of the medium, then the S2 stimulus was applied after the wave had passed half of the medium.

Fig. 2.3 shows the resulting patterns of transmembrane voltage after 10 s of
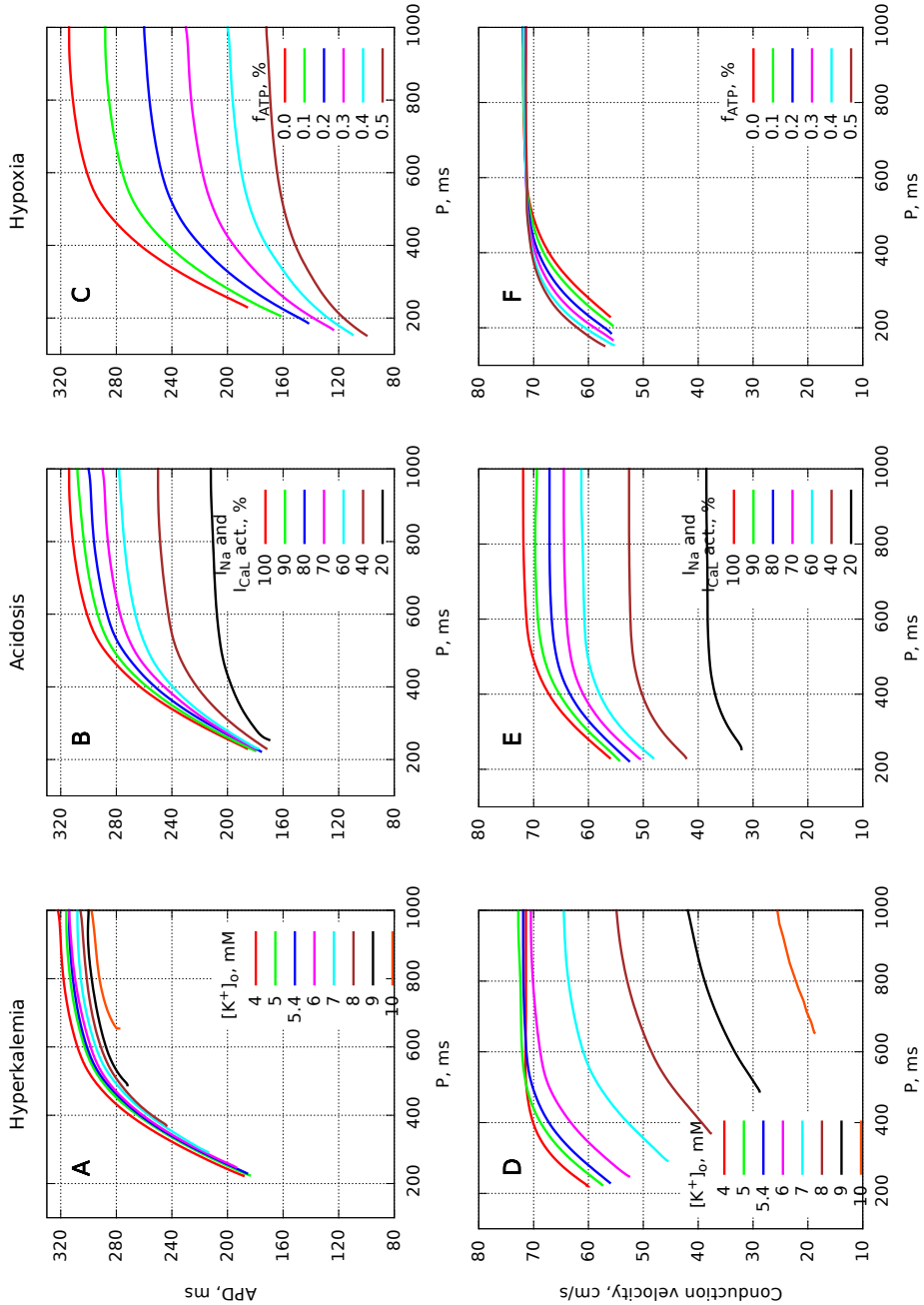
Figure 2.2. A, B, C: APD restitution curves for hyperkalemia, acidosis and hypoxia respectively. D, E, F: CV dispersion relations for hyperkalemia, acidosis and hypoxia respectively. P denotes the sum of diastolic interval (DI) and APD at the point of measurement for the pulse generated by the S2 stimulus.
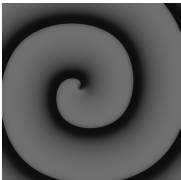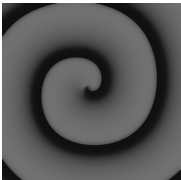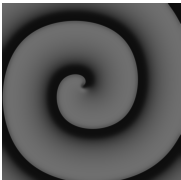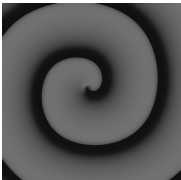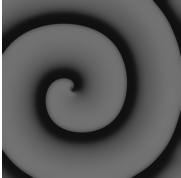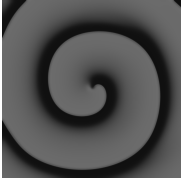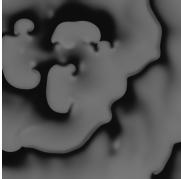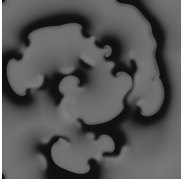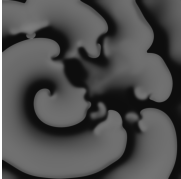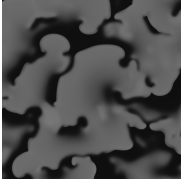
Rest. slope for normal conditions	Normal conditions	Hyperkalemia $[K^+]_o = 6$ mM	Acidosis $G_{Na,CaL} = 80\% \cdot G_{Na,CaL}^0$	Hypoxia $f_{ATP} = 0.1\%$
1.1				
1.4				
1.8				

Rest. slope for normal conditions	Normal conditions	Hyperkalemia $[K^+]_o = 7$ mM	Acidosis $G_{Na,CaL} = 60\% \cdot G_{Na,CaL}^0$	Hypoxia $f_{ATP} = 0.3\%$
1.8				

Figure 2.3. Stability of spirals under ischemic conditions. Greyscale shows membrane voltage, with light grey indicating depolarized tissue.

simulated activity for each parameter set and under each component of ischemia. For tissue with a restitution slope of 1.1 under normal conditions, the spiral remained stable regardless of ischemia. For a restitution slope of 1.4 (the second row), a complex fibrillatory pattern developed under normal conditions resulting from breakup of the initial spiral wave, however each ischemia factor prevented breakup. The third row gives an example for a relatively high restitution slope of 1.8 under normal conditions. In this case the spiral wave broke into fibrillation under both normal and ischemic conditions. However, it was still possible to stabilize the spiral rotation by further increasing the ischemia parameters. The bottom row in Fig. 2.3 corresponds to that case: as ischemia became more severe the activation pattern did not evolve into fibrillation.

Overall, all three components of ischemia acted to stabilize re-entry, and to prevent the breakups that can happen under normal condi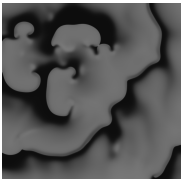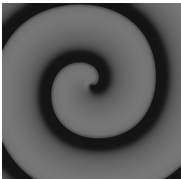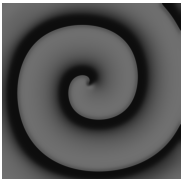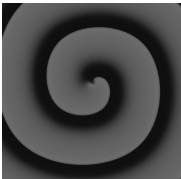tions. This is in line with the prediction that we derived from analyzing the restitution curves in the previous section, which was based on flattening of the restitution curves due to ischemia.

Our next step was to understand the change of the main dynamical characteristics of cardiac tissue with ischemia and to compare these with the activation patterns observed in the human heart [53]. Therefore, we performed simulations using an anatomically detailed model of the human ventricles developed in [59]. To explain our results we shall use information on 1D and 2D wave propagation collected in the previous sections.

2.3.3 VF in an Anatomical Model of the Human Ventricles Incorporating Simulated Global Ischemia

Wave Patterns

The three components of ischemia were modeled as described in Table 2.1. VF was induced using an S1S2 protocol which resulted in a subsequent spiral wave breakup and onset of the fibrillatory pattern as described in [59]. It was shown that this protocol reproduces the main features of VF in the human heart [50, 59]. The resulting state after 5 s of initialization was saved and used as an initial condition for subsequent simulations to investigate the effect of ischemic components on VF dynamics.

Fig. 2.4 shows example snaphots of activation in the anatomically detailed model for both normal and ischemic conditions, with each ischemic component set to values corresponding to those obtained from the human recordings, as we will show later.

Fig. 2.4A–D show typical excitation patterns during simulated VF, both in terms of wave fronts (A: front view, B: lateral view) and activated regions for which the voltage is higher than APD_{90} level (C, D). Here we have a complex fibrillatory pattern characterized by multiple re-entrant waves. For every sub-
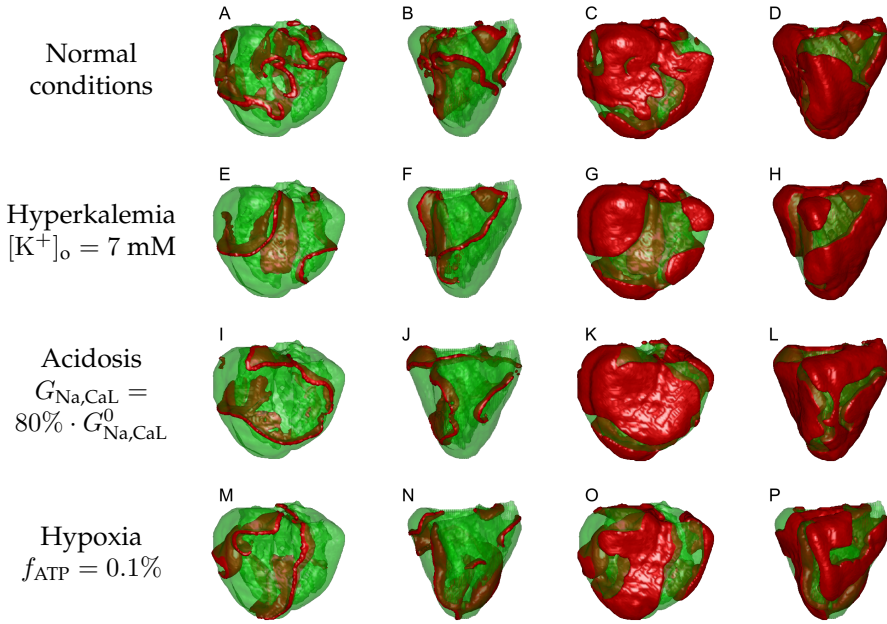
Figure 2.4. Fibrillation patterns: A–D: normal conditions, E–H: hyperkalemia, I–L: acidosis, M–P: hypoxia. In the first two columns the red color shows the location of wavefronts, and in the last two columns it shows exited tissue where the transmembrane voltage is higher than APD_{90} level. Columns 1, 3 show the frontal view and columns 2, 4 show the lateral view.

sequent simulation, we started from this initial state and gradually (within 200–800 ms) changed the corresponding parameters from their normal values to the values corresponding to the different ischemic conditions, and then computed for a further 15 s of model time. Examples of fibrillation patterns we obtained are shown in Fig. 2.4E–P.

Fig. 2.4E–H give the resulting picture for hyperkalemia with $[K^+]_o = 7$ mM. The complexity of activation was slightly lower in comparison with the initial state, with fewer wavefronts. Fig. 2.4G–H show the amount of activated tissue for this snapshot. The ratio of green to red was larger for hyperkalemia, which indicates that the tissue became less excitable. Similar results can be seen for hypoxia $f_{ATP} = 0.1\%$ in Fig. 2.4M–P. The medium was less excitable and the complexity of VF was slightly lower compared to normal.

Acidosis had a less pronounced effect on both excitability and pattern complexity. Fig. 2.4I–L give an example of fibrillation under acidosis conditions where the conductivity of I_{Na} and I_{CaL} were reduced to 80%.
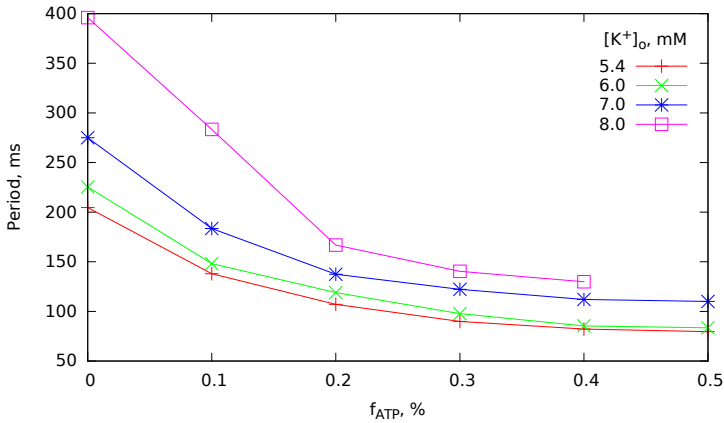
Figure 2.5. The effect of hyperkalemia and hypoxia on period of simulated VF in anatomically detailed 3D model.

Period of VF

The period of VF in each simulation was determined using a discrete Fourier transform of time series of transmembrane voltage obtained from 10000 locations in the heart model for the last 7 s of model time, and obtaining the period from the frequency of the largest peak in the spectrum.

We found that the period of fibrillation showed almost no dependence on acidosis. Even for a severe drop of I_{Na} and I_{CaL} conductivity (5-fold) the change of the period was less than 5% compared to normal (not shown). This effect can be also seen on the restitution curves in Fig. 2.2: the APD_{min} value, which is believed to determine the frequency of VF [50], is almost unchanged with acidosis. For this reason acidosis was excluded from further analysis and the following results describe a two parameter space of hyperkalemia and hypoxia.

The dependence of the average period of VF on hypoxia and hyperkalemia is shown in Fig. 3.8. The period of fibrillation increased under hyperkalemia, and decreased under hypoxia. The effect of hyperkalemia was more pronounced for smaller values of f_{ATP}. Also, a saturation effect can be seen: for larger values of f_{ATP} the effect of additional hypoxia was relatively small.

At the first glance, our observation that hyperkalemia acted to increase the period of VF contradicts the results of our 1D studies, which showed that APD decreased with increase of $[K^+]_o$. However, as in the case of acidosis, the most important factor here is APD_{min}, which increases with hyperkalemia (Fig. 2.2A) and, therefore, explains the observed increase in the period of VF.

Explanation of the observed decrease of period under hypoxia is straightforward. The main effect of hypoxia is shortening of the action potential. Indeed, we see in Fig. 2.2C that APD_{min} becomes smaller under hypoxia. This shorten-
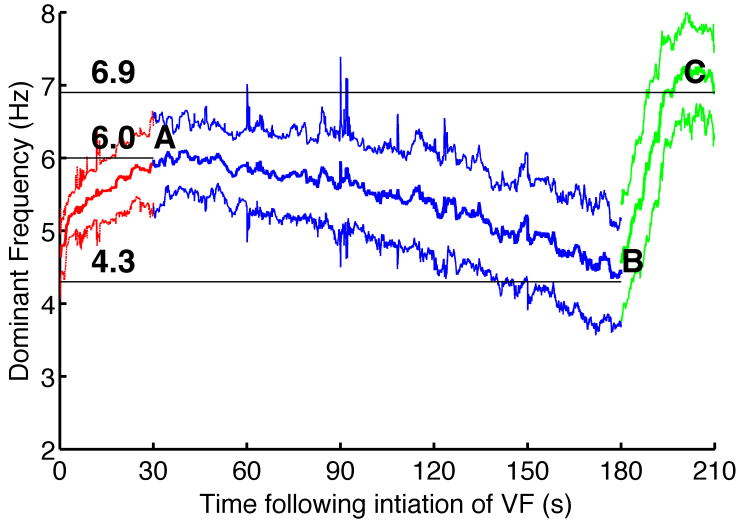
Figure 2.6. Change of DF over time for one patient (H066). Red denotes DF recorded with the heart perfused, blue denotes ischemia, and green reflow. The middle line shows mean DF, averaged over electrodes, and the top and the bottom lines show one standard deviation either side of the mean.

ing of APD results in a decrease of the period of VF. The effect of hyperkalemia turned out to be more pronounced for smaller values of f_{ATP}.

We used the data of Fig. 3.8 to estimate the effects of these two factors of ischemia on the period change during ischemia observed in [53].

2.3.4 Estimation of the relative contribution of hyperkalaemia and hypoxia to patient data

Our results allowed us to estimate the extent of hyperkalemia and hypoxia for each patient involved in the clinical study [53]. We used the dependency of how DF (1/period) changes throughout experimental VF for individual patients. One of these recordings is shown in Fig. 2.6. The red region corresponds to normal perfusion of the heart, blue to global ischemia and the green to reperfusion. As one can see, DF gradually decreases during ischemia and then increases abruptly after reperfusion to an even higher level that it was initially.

For each patient we used three points on this graph: DF at the beginning of ischemia (30 s, point A), DF at the end of ischemia (180 s, point B) and DF at the end of the experiment (210 s, point C). Ischemia takes place in between points A

45

| | Regular fit | | | | | | Alternative fit | |
| | 0% | | 25% | | 50% | | 0% | |
Patient	$[K^+]_o$	f_{ATP}	$[K^+]_o$	f_{ATP}	$[K^+]_o$	f_{ATP}	$[K^+]_o$	f_{ATP}
H055	7.2	0.024	7.3	0.032	7.5	0.049	7.2	0.076
H057	7.2	0.020	7.3	0.027	7.5	0.041	7.2	0.055
H058	7.6	0.029	7.7	0.039	7.9	0.058	7.9	0.141
H059	6.9	0.049	7.1	0.065	7.4	0.098	7.0	0.102
H060	7.0	0.031	7.1	0.041	7.3	0.062	7.0	0.053
H062	6.7	0.012	6.8	0.016	6.9	0.025	6.8	0.098
H063	7.4	0.010	7.4	0.013	7.5	0.020	7.3	0.076
H064	6.7	0.019	6.8	0.025	7.0	0.038	6.7	0.047
H065	8.0	0.072	8.2	0.096	8.8	0.144	8.4	0.157
H066	7.4	0.046	7.6	0.061	7.8	0.092	7.5	0.096

Table 2.2. Estimated values of extracellular potassium concentration and number of activated K_{ATP} channels for the patients studied in [53]. The estimate for the 'regular fit' is based on graphs from Fig. 3.8 scaled to the value of the period at point A. For the 'alternative fit' we scaled our results to the value of the period given at the beginning of the clinical recordings. The percentages correspond to the ratios of K_{ATP} channels recovered during reperfusion. Further explanations are in the text.

and B, thus $[K^+]_o$ and f_{ATP} are increasing there. At point B we expect to have the highest values for these quantities.

At point B reperfusion starts, resulting in a rapid elevation of DF. Fig. 3.8 indicates that hypoxia acts to shorten the VF period, thus it is likely to be responsible for this change. Therefore we assumed that the recovery of hypoxic K_{ATP} channels during reperfusion is slower than the recovery of extracellular potassium concentration. We assumed that $[K^+]_o$ had returned to a normal value by the point C whereas f_{ATP} remains at the same level as at point B. Thus, knowing DF at point C, we can find the fraction of open K_{ATP} channels at that moment. Using this value and the value of DF we can estimate $[K^+]_o$ at point B. The results we obtained using this algorithm are given in first three columns of Table 2.2. The results shown in columns 4–7 of the table deal with a possible partial recovery of f_{ATP} and will be described in the discussion section. The results in the last two columns are based on the assumption that K_{ATP} channels open even before the beginning of ischemia. This will also be described in the discussion section.

We see that the estimated $[K^+]_o$ concentrations for different patients vary in the range from 6.5 to 8.0 mM, while the fraction of activated K_{ATP} channels f_{ATP} does not go beyond 0.1%.

We also estimated how hypoxia and hyperkalemia change in the course of ischemia. This problem of fitting does not have a unique solution because the period of fibrillation depends on two parameters, while we have only one period dependency for each patient. To account for that we assumed that the depen-

dencies of $[K^+]_o$ and f_{ATP} are monotonic with time, and these values can never decrease during ischemia. Then we wrote the relation between the rate of change of these values:

$$\frac{dT}{dt} = \frac{\partial T}{\partial [K^+]_o} \frac{d[K^+]_o}{dt} + \frac{\partial T}{\partial f_{ATP}} \frac{df_{ATP}}{dt}, \tag{2.5}$$

where $T(t)$ is the period of fibrillation over time (from the clinical results) and $T([K^+]_o, f_{ATP})$ is the dependency of VF period on the ischemia components, obtained from Fig. 3.8. Our goal was to determine the patient specific functions $[K^+]_o(t)$ and $f_{ATP}(t)$, based on known $T(t)$, $T([K^+]_o, f_{ATP})$ and boundary conditions from Table 2.2. To solve (2.5) we needed to impose an additional constraint on our functions. Thus we assume that

$$\frac{d[K^+]_o}{df_{ATP}} = \frac{[K^+]_{o,B} - [K^+]_o}{f_{ATP,B} - f_{ATP}}, \tag{2.6}$$

where $[K^+]_{o,B}$ and $f_{ATP,B}$ are the values we fitted for point B. This constraint ensured the values of hypoxia and hyperkalemia tended to reach those values at point B. The results we obtained using this approach are shown in Fig. 2.7 and Fig. 2.8. We see that we can fit the clinical data with smooth monotonic functions using our approach. However, as our constraint (2.6) cannot be justified from biological background, these fits can be considered as a conjecture rather than established results.

2.3.5 Number of Reentrant Sources

The study of [53] describes how the number of epicardial phase singularities and the number of wave fronts change during the course of ischemia. These values have approximately the same dynamics and to understand the results we studied the change in the number of phase singularities. Phase singularities are points where filaments intersect the surface of the heart [47, 50]. As was shown in [50], the number of filaments obtained from simulations in an anatomically detailed model of human ventricles provides a good estimate of the number of phase singularities on the surface of the heart. We counted the number of filaments in our model in normal conditions and under different factors of ischemia.

Fig. 2.9 shows four examples of how the number of filaments depends on time under conditions that we expect to correspond to those observed for the first 2.5 minutes of ischemia. Fig. 2.9A shows filament numbers during normal conditions. We see dynamics similar to that reported in [59]. Fig. 2.9B and C correspond to hyperkalemia $[K^+]_o = 7$ mM and hypoxia $f_{ATP} = 0.1\%$, respectively. We see that compared to normal condition there is a tendency for decreasing of the number of filaments. Finally, Fig. 2.9D gives an example where simulated VF terminated spontaneously, although the number of filaments stayed relatively high until immediately prior to termination. For that simulation we
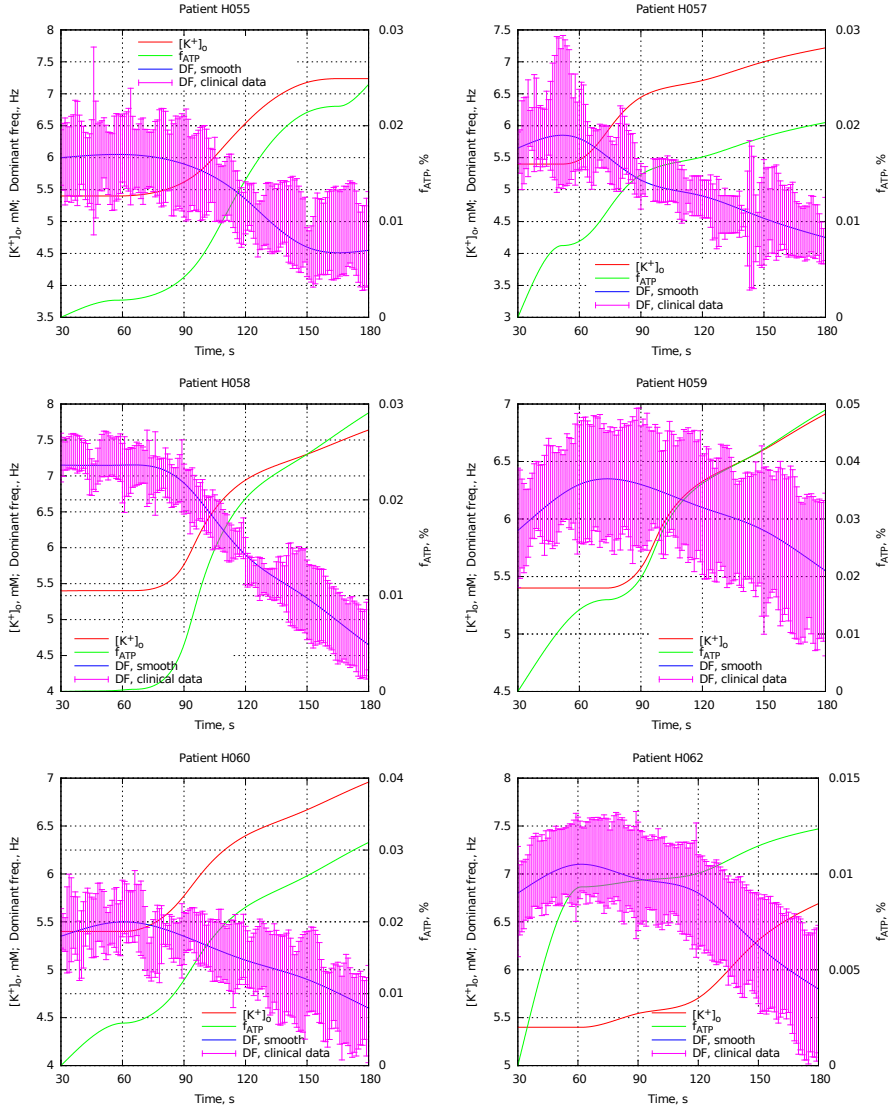
Figure 2.7. Evolution of hypoxia and hyperkalemia in the course of global ischemia. Pink: clinical data on the dominant frequency, averaged over 1 s window with standard deviation. Blue: smoothed curve that we used for our fitting. Red: extracellular potassium concentration. Green: fraction of activated K_{ATP} channels.
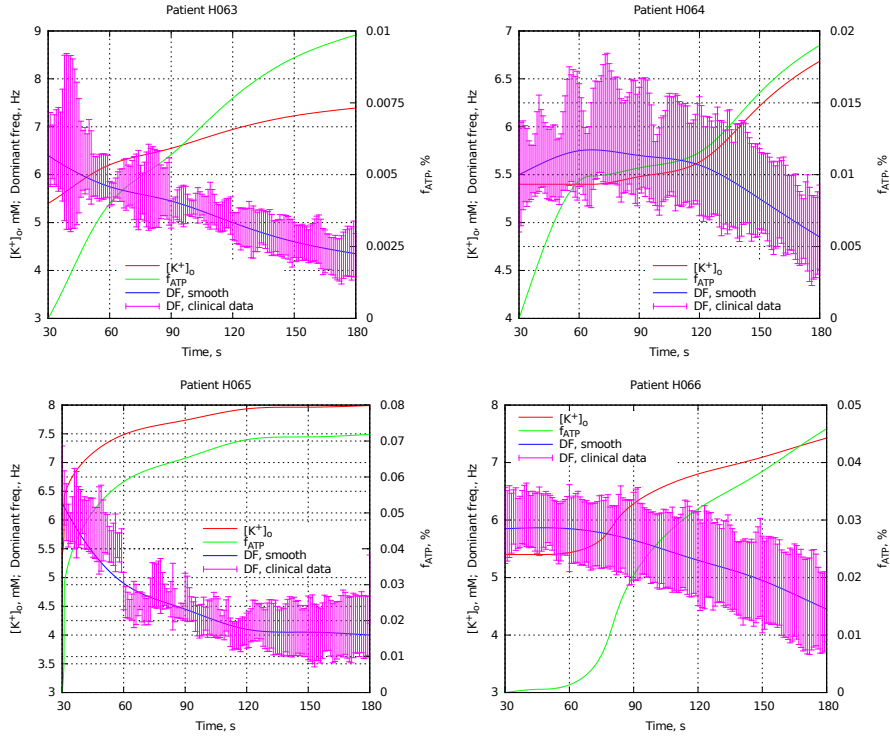
Figure 2.8. Evolution of hypoxia and hyperkalemia in the course of global ischemia. Pink: clinical data on the dominant frequency, averaged over 1 s window with standard deviation. Blue: smoothed curve that we used for our fitting. Red: extracellular potassium concentration. Green: fraction of activated K_{ATP} channels.
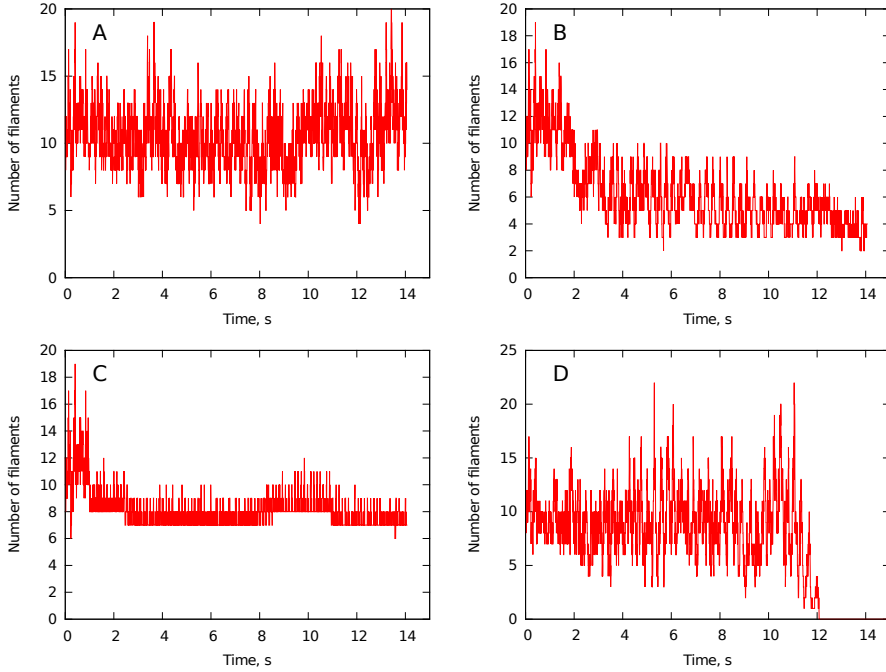
Figure 2.9. Change of the number of filaments in course of time under different ischemia factors obtained from numerical simulations. A: normal conditions, B: hyperkalemia, C: hypoxia, D: example of spontaneous fibrillation stop.
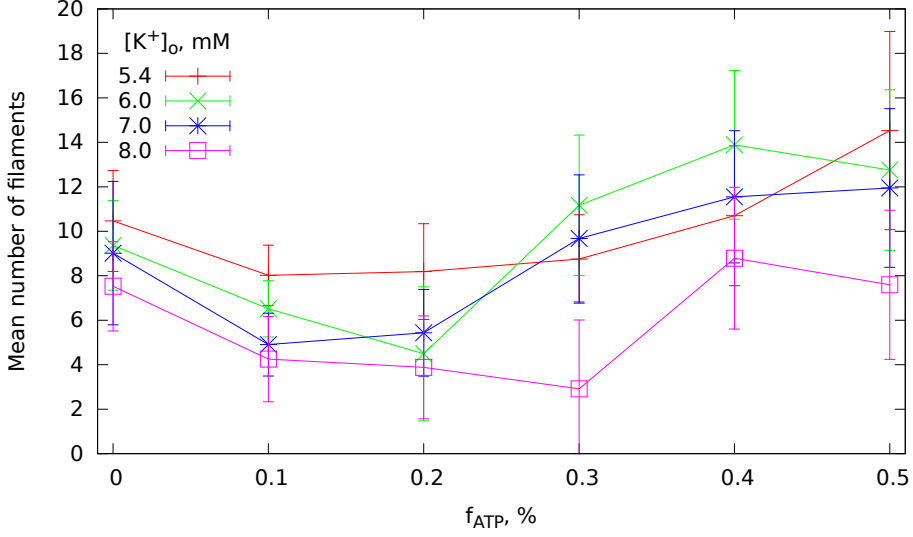
Figure 2.10. The mean number of filaments of a fibrillation pattern averaged over time of simulation after applying ischemic conditions. The error bars indicate the standard deviation of root mean square.

used $[K^+]_o = 8$ mM and $f_{ATP} = 0.4\%$.

The mean number of filaments in the two parameter space—hyperkalemia and hypoxia—for a wider range of parameters is given in Fig. 2.10. The error bars in this figure correspond to the standard deviations of root mean square. The point with $[K^+]_o = 5.4$ mM and $f_{ATP} = 0$ corresponds to normal conditions. We can see that for values of hypoxia $f_{ATP} < 0.1\%$ the complexity of the pattern slightly decreases. However, it increases for larger values of hypoxia. All these results differ substantially from our observation from the 2D patterns (see Fig. 2.3). In 2D, we observed that every single component of ischemia suppressed breakup, which would correspond to a decrease of filament numbers and termination of fibrillation in our whole heart simulations. However, this figure shows that for 3D an increase in fibrillation complexity as the degree of ischemia increases.

This is a surprising result that can be explained in the following way. The 2D simulations always started from a single spiral, and breakup was self induced. In 3D, however, we started from an initial pattern with multiple re-entrant waves. This complex pattern was able to maintain itself in spite of the presence of simulated ischemia. To confirm this observation, we performed simulations in 2D, starting from a developed VF pattern. These simulations showed that even in 2D, the complex pattern can persist compared with initiation with the S1S2 pro-

Patient	Before ischemia	After ischemia
H055	2–17	1–18
H057	2–15	2–20
H058	3–22	4–25
H059	2–22	3–26
H060	2–15	2–18
H062	4–22	5–24
H063	1–14	1–19
H064	1–13	2–15
H065	1–11	1–18
H066	2–18	2–22

Table 2.3. Minimal and maximal values of the number of phase singularities during the first and the last ten seconds of ischemia for the patients studied in [53].

tocol of Fig. 2.3.

The results of the clinical research are presented in Table 2.3. The minimal and maximal value of the number of phase singularities on the surface of the heart are given there for both the beginning and the end of ischemia. As shown, there are large deviations in PS numbers making it difficult for us to give conclusive statements from these data. However, they do indicate relative conservation on PS numbers during ischemia.

If we now compare these results with results on filament numbers shown in Fig. 2.10 we can conclude the following. In the range of ischemic components which we estimated for the individual patients ($[K^+]_o < 8$ mM, $f_{ATP} < 0.1\%$) we see some tendency for a decrease in the filament numbers in our simulations. However, this decrease is minimal and to some extent can be considered as conservation of filament numbers in a way similar to that we see in clinical data. However, our simulations indicate that we can expect an increase in filament numbers if ischemia is more prolonged or if I_{KATP} channels open to a greater extent.

2.4 Discussion

The aim of this study was to use a model of cardiac electrical activity to gain insight into the mechanism underlying the organization of ventricular fibrillation observed in the in-situ human heart with global cardiac ischemia. We performed numerical simulations using a detailed electrophysiological model of cardiac cells and tissue under normal and ischemic conditions. This model was examined in pseudo-1D and 2D tissue geometries, and in an anatomical model of human ventricles which takes the geometry and anisotropy of cardiac tissue into account. As in [26, 57, 58] we subdivided the effects of ischemia into three

main syndromes: hyperkalemia, acidosis and hypoxia. To represent the activation of K_{ATP} channels in hypoxia, we developed a new model of the human K_{ATP} channel, based on recordings of [55].

Our 1D and 2D studies demonstrated that each component of ischemia results in a shortening of APD under the same base cycle length, which is in accordance with the results of other modeling research [57]. Our results for CV restitution (dispersion relation) are similar to those obtained in [58] with a small difference: the CV does not depend monotonically on hyperkalemia. As can be seen in Fig. 2.2D, in our simulations CV increases with hyperkalemia for lesser values of $[K^+]_o$ whereas for higher ones it decreases. This supernormal conductance effect was not observed in studies of [58], which may be due to a different stimulation protocol. Overall, the restitution curves we obtained are very similar to [54].

According to the restitution hypothesis, our observation that the steepness of APD restitution curves decreases with ischemia makes dynamical instabilities less likely to occur, and wavebreak leading to multiple wavelet VF less probable [64]. We confirmed this in our 2D simulations. In particular, we found that it was sufficient to increase any of the ischemic factors within their physiological range to prevent break up that can occur under non ischemic conditions. This is also in line with the simulations on effects of activation pattern due to restitution steepness by [64, 66].

The main part of the present study deals with simulations in a 3D anatomically accurate model of the ventricles of the human heart for situations that resemble the clinical set up used in [53]. Our aim was to describe how the organization of simulated VF is altered due to cardiac ischemia. We found that acidosis had almost no effect on the activation rate, while hyperkalemia decreased and hypoxia increased the frequency of VF. Studies of this effect were not previously performed in anatomical models, although they are similar to 2D simulations and experiments in animal models. The effect of hyperkalemia on the period of spiral wave rotation was studied by [67] who obtained similar dependency but only for concentrations of $[K^+]_o$ larger than 8 mM. The same effect of hypoxia was investigated by [68] on canine ventricular slices and later by [69] on swine hearts. The results obtained in their experiments are in accordance with our simulations.

The dependence of activation rate on ischemic factors could be predicted by looking at our APD restitution curves. Fibrillatory excitation patterns have a very high activation rate, and thus the leftmost regions of restitution curves are of considerable importance since they correspond to high activation rate and short diastolic interval. If we look, for instance, at Fig. 2.2A we see that the leftmost points shift to the right with hyperkalemia. Thus the activation frequency of fibrillation decreases. The minimal possible values of APD, which are given by the left most points, are called APD_{min}. Thus this finding once again emphasizes a particular importance of these APD_{min} on VF organization which has also been

demonstrated in other studies [61, 65]. Note, that the APD_{min} point is achieved at the minimal possible period of stimulation, which is, perhaps, more directly related to the period of excitation during VF.

With our 3D simulations we were able to construct a model of the dependency of VF period on both hyperkalemia and hypoxia. This model, along with additional assumptions about the relative rates at which the different components of ischemia develop allowed us to propose a way to estimate the extacellular potassium concentrations and the fraction of open K_{ATP} channels for the recordings in the clinical study [53]. The estimated external potassium concentrations correspond to experimental data showing a rate of $[K^+]_o$ change of about 0.5–1 mM per minute [43].

The most important assumption in this study was that the rate of recovery from hypoxia during reperfusion is slower than the rate of recovery from hyperkalemia. Experimental data from porcine hearts [70] show that the complete recovery of $[K^+]_o$ during reflow can occur within less than one minute. Unfortunately the data available on the recovery of K_{ATP} are controversial which makes it difficult to assess whether our assumption is correct. Data from the the human heart [53, 71] obtained at the whole organ level show that, even after 5 minutes of reflow, less than 70% of the APD shortening (which was assumed to be an effect of K_{ATP} opening) had been reversed. On the other hand, experimental data from single cells demonstrate that recovery can be very fast, of the order of a few seconds [72, 73].

To investigate an effect of this possible partial recovery of hypoxia we estimated how our estimates change if we assume that after 30 seconds of reperfusion either 25% or 50% of K_{ATP} had been recovered. These estimates are shown in the columns 4–7 of Table 2.2. The second and the third columns are given for the case of no recovery. As we can see, partial recovery does not have a pronounced effect on the estimated values of hyperkalemia during ischemia. Indeed, for most of the patients the error in $[K^+]_o$ estimation due to this partial recovery is about 0.3–0.4 mM.

We have also proposed a method of fitting the change in $[K^+]_o$ and f_{ATP} for each individual patient during global cardiac ischemia. Note, however, this problem is nontrivial because its exact solution requires more experimental details on the speed of various processes during ischemia. The approach that we followed is based on solving a boundary problem for an ordinary differential equation (ODE), expanded with one artificial ODE that provided a relation between relative change of the hyperkalemia and hypoxia factors. We also tried other, less sophisticated methods to target this problem, such as linearly varying one of the factors and finding the time course for the other one. The deficiency of these simple methods was that they violated the assumption that ischemia factors grow monotonically for some of the data. Therefore we followed our approach, although it is not based on any mechanistic background. As soon as more data on the effects of ischemia in the human heart are available, our ap-
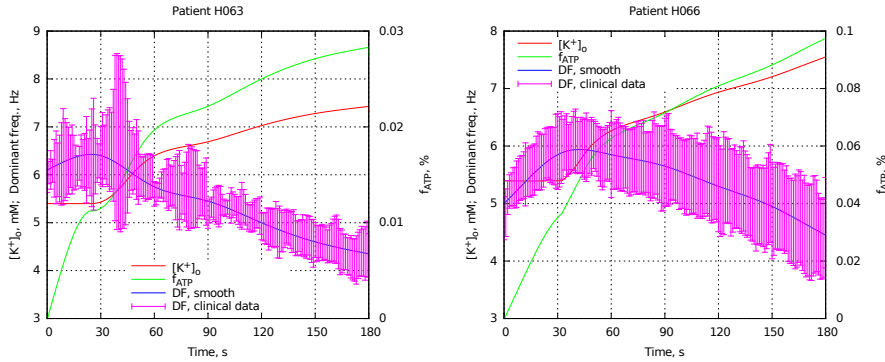
Figure 2.11. Two examples of how hypoxia and hyperkalemia evolve during ischemia assuming that the K_{ATP} channels open before the beginning of ischemia due to energy depletion. The legend is the same as in Fig. 2.7 and Fig. 2.8.

proach could be improved by adding more constraints on the solution.

Our clinical data show that in all recordings there was an initial increase of the dominant frequency that happens during the first 30 s of the study under normal perfusion. This effect was also obtained in other studies [49, 74]. A possible explanation for this effect is the following. Since ventricular fibrillation is an energy consuming process, it may shift the [ADP] to [ATP] ratio, and hence diminish the energy capabilities of the cells. This would lead to opening of K_{ATP} channels, and result in an increased DF. To examine this possible explanation, we modified our fitting method, taking the DF at the beginning of the recording as corresponding to normal conditions. The maximum values for hypoxia and hyperkalemia for this case are shown in the last the columns 8–9 of Table 2.2. We see that this alternative assumption leads to an increased number of activated K_{ATP} channels, whereas the extracellular potassium concentration remains relatively unchanged. We also adapted this assumption for our fitting algorithm describing how hypoxia and hyperkalemia evolve in the course of ischemia. The results for two patients: H063 and H066 are given in Fig. 2.11.

Finally, we studied the effects of global cardiac ischemia on the complexity of activation patterns during simulated VF. For that we used an established VF activation pattern as an initial condition for the simulations. This type of initial condition differs from most of the previous studies of the restitution based fibrillation, where a single spiral is used for the initial condition and the conditions under which this spiral develops into fibrillation are in question. We found that using established VF as an initial condition showed that flattening of the restitution curve caused by ischemia does not usually lead to VF termination, but rather results in a small number of stable re-entrant sources. We think that this finding does not contradict to the results obtained on spiral breakups in 2D. Indeed, flattening of restitution curves just prevents the onset of VF, however,

this process is not directly related to the elimination of multiple existing spirals. In fact, flattening of the restitution curves decreases dynamical instabilies and makes the rotation of spirals more stable, thus it is even more likely to stabilize multiple spirals in the tissue. The tendency for a fibrillation pattern to become more organized due to global ischemia was first demonstrated experimentally by [75] on rabbit hearts. In addition, a recent experimental study on the effects of hypoxia in swine hearts by [69] has also shown that activation of K_{ATP} channels makes the fibrillation pattern more stable and stops rotors from meandering. However, a study by [64], performed also on swine hearts, argues that flattening of the restitution curve does favour VF termination, though, to achieve that flattening they used a potassium channel antagonist—bretylium—which has an effect opposite to hypoxia.

Limitations

There are several factors that were not taken into account in this study. We used a homogeneous model of the heart which does not take into account the differences between epicardial, endocardial and M-cells. However, as it is shown in [76] the differences between these cell types decrease substantially at the high frequency of excitation typical for VF patterns. Note that the differences between different cell types are not that pronounced in tissue due to the electrotonic effect. Next, we used a monodomain model, to represent the cardiac tissue. Bidomain models are of considerable importance when describing defibrillation phenomena but in the absence of applied external currents the difference between these two types is extremely small [77].

Due to numerical limitations, we were not able to reproduce full 3.5 minutes of the clinical study in our model and limited ourselves by only 20 seconds. We did not check if the effects we studied are also presented in other detailed electrophysiological models of cardiomyocyte, such as [78] and [79], nor did we take into account effects due to mechanical activity of the heart during VF.

We did not consider the change in the gap junction conductance caused by ischemia. There are several experimental studies on animal models that demonstrate that the effect on gap junction uncoupling is relatively small in first minutes of ischemia. The investigations in a rabbit papillary muscle [80] show that under ischemic conditions the intracellular resistance stays constant within the first 10–15 minutes, whereas the extracellular resistance slightly changes immediately following the onset of ischemia. However this change was not associated with a significant decrease of the conduction velocity within the first 4 minutes of ischemia. Another result obtained in isolated rat hearts [81] indicates that the absolute value of the impedance of the tissue changes for about $3\,\mathrm{Ohm}\cdot\mathrm{cm/min}$ with the initial value of about $150\,\mathrm{Ohm}\cdot\mathrm{cm}$. Finally, another set of experiments on rabbit papillary muscle [82] also shows that the tissue resistance stays remarkably stable for the first 10 minutes of acute ischemia. These data allow us to

assume that the process of gap junction uncoupling does not have a significant effect on the conduction velocity for the time scale of 2.5 minutes of ischemia.

We did not consider either the heterogeneity of the tissue response to ischemia nor heterogeneity in ionic channels distributions. As shown in other studies [83], heterogeneities in I_{KATP} distribution can lead to a transmural gradient of the DF in myocardium. There are several studies that show that this gradient occurs in experimental models [51, 52, 84]. Furthermore, global ischemia may lead to different depths of ischemia in different regions of the heart, since the endocardium is in contact with a large volume of oxygenated blood in the ventricular cavities, at least in the early stages of VF. We expect that these heterogeneities can lead to a different fibrillation mechanism (to so-called mother rotor fibrillation) as well as increase in the number of filaments [85, 86]. This factor may also contribute to increasing the number of phase singularities localized at the surface of the heart.

The role of Purkinje system was not considered in this study. There are several experimental studies in dog hearts [84, 87], which show that the Purkinje system can play an important role in early termination of VF because it acts to increase the transmural activation rate gradient. However, a computer modeling study [83] shows that this effect is not that prominent in comparison with the effect of heterogeneity in I_{KATP} distribution.

Finally, we omitted several other effects that may occur during ischemia. In our case, depletion of ATP results only in activation of the K_{ATP} channel. We did not consider the effect of ATP on other important processes, such as functioning of the K/Na pump, the processes occurring at the mitochondria membranes and their effect on calcium dynamics. We did not take into account any changes of cell size or extracellular medium size occurring as a result of osmosis, and possible changes of the ionic concentrations due to it. It would be valuable to extend existing cell models to incorporate a more detailed description of ischemia, and to study the effects of ATP depletion using such a model.

Chapter 3

Effects of Heterogeneous Diffuse Fibrosis on Arrhythmia Dynamics and Mechanism

IVAN V. KAZBANOV[1], KIRSTEN H. W. J. TEN TUSSCHER[2], AND ALEXANDER V. PANFILOV[1,3]

[1]Department of Physics and Astronomy, Ghent University, Belgium
[2]Department of Biology, Utrecht University, Utrecht, the Netherlands
[3]Moscow Institute of Physics and Technology (State University), Dolgoprudny, Moscow Region, Russia

Abstract

Myocardial fibrosis is an important risk factor for cardiac arrhythmias. Previous experimental and numerical studies have shown that the texture and spatial distribution of fibrosis may play an important role in arrhythmia onset. Here, we investigate how spatial heterogeneity of fibrosis affects arrhythmia onset using numerical methods. We generate various tissue textures that differ by the mean amount of fibrosis, the degree of heterogeneity and the characteristic size of heterogeneity. We study the onset of arrhythmias using a burst pacing protocol.

We confirm that spatial heterogeneity of fibrosis increases the probability of arrhythmia induction. This effect is more pronounced with the increase of both the spatial size and the degree of heterogeneity. The induced arrhythmias have a regular structure with the period being mostly determined by the maximal local fibrosis level. We perform ablations of the induced fibrillatory patterns to classify their type. We show that in fibrotic tissue fibrillation is usually of the mother rotor type but becomes of the multiple wavelet type with increase in tissue size. Overall, we conclude that the most important factor determining the formation and dynamics of arrhythmia in heterogeneous fibrotic tissue is the value of maximal local fibrosis.

3.1 Introduction

Cardiac arrhythmias remain one of the largest causes of death in the industrialised world. In many cases, cardiac arrhythmias occur in a structurally abnormal heart where the properties of cardiac tissue have changed. The problem of substrate, that is, of identification of properties of cardiac tissue that predispose to cardiac arrhythmias, is of great interest. Structural changes of cardiac tissue, also called remodeling, occur as a result of many cardiac diseases. For example, in the ventricles of the heart, remodeling occurs after myocardial infarction and during heart failure [88, 89]. In atria, it occurs during sustained atrial fibrillation [89, 90] and under many other pathological conditions. Typically, tissue remodeling has several components: change in the properties of ionic channels (ionic remodeling), a reduced number of gap junctions, changes in cell size, and changes in overall tissue structure. The latter mainly occurs as a result of the proliferation of non-excitable cardiac fibroblasts and an increase in the collagen fibres secreted by these fibroblasts, together called fibrosis. Interstitial fibrosis accompanies tissue remodeling in most of the aforementioned cases, and the percentage of fibrotic tissue can increase up to 40% [91]. As the presence of non-excitable cells substantially affects cardiac wave propagation, it is not surprising that fibrosis affects the onset of cardiac arrhythmias and is considered an arrhythmogenic condition [27].

The relation of fibrosis and arrhythmias has been investigated in several ex-

perimental studies. It has been shown that the inducibility of ventricular arrhythmias increases in a nearly linear fashion with the amount of fibrosis [92]. In addition, studies [91, 93, 94] have shown that the structure and spatial distribution of fibrosis play a crucial role in arrhythmogenesis. However, as discussed above, tissue remodeling affects many properties of cardiac tissue simultaneously. Indeed, the importance of heterogeneity in distribution of other factors involved in excitation wave propagation has also been demonstrated experimentally. For example, De Bakker [95] showed that in human and in mice hearts, the onset of cardiac arrhythmias is associated with heterogeneity in Cx43 distribution rather than its mean levels. In addition, it was shown that remodeling induced decreases in I_{Na} [96] play an important role in the onset of arrhythmias. Since many factors involved in tissue remodeling appear to have an arrhythmogenic effect, it is hard to experimentally determine the exact role of fibrotic tissue in arrhythmogenesis. Furthermore, the spatial variation of fibrosis is difficult to control in experiments. Therefore, alternative approaches are needed to determine the importance of heterogeneity in fibrotic patterns on arrhythmia onset. Mathematical modeling of cardiac excitation is a particularly suitable approach since it allows one to study fibrosis independently from the other remodeling factors, to precisely control levels and patterns of fibrosis, and study a large number of different fibrosis patterns.

Mathematical modeling has been widely used to study the effects of fibrosis on cardiac arrhythmias. In a series of papers [97–100], the effect of diffuse fibrosis on the onset of arrhythmias due to steep APD restitution was studied. This research led to the paradoxical finding that while diffuse fibrosis promotes spiral wave formation, it suppresses spiral wave fragmentation. It was shown that fibrosis reduces the possibility of steep-restitution induced spiral breakup due to an increase in the period of spiral wave rotation. Furthermore, it was shown that this period increase can result in the onset of 3D instabilities, such as negative filament tension [101]. Thus, while diffuse fibrosis suppresses steep restitution induced spiral breakup it promotes alternative 3D spiral breakup mechanisms [102].

In addition, a lot of research has focused on the effect of possible myocyte-fibroblast coupling on the conduction velocity and spiral wave dynamics [103, 104]. The relation of fibrosis and extracellular electrograms was studied in [105] in a model of human atrial tissue. It was shown that the presence of fibrotic tissue in the atria may be responsible for complex fractionated electrograms. Furthermore, it was demonstrated that ablation of the fibrotic areas producing the fractionated electrograms may terminate atrial fibrillation. The role of fibrosis in the initiation and maintenance of atrial fibrillation was also demonstrated in an anatomically accurate setup using detailed fibrosis models in [106–108].

Although some of these computational studies have investigated the effect of different types of fibrosis on wave propagation (e.g. [105]), so far no systematic study has been performed on the effects of the heterogeneity of fibrosis on

wave propagation and arrhythmia generation. In addition, none of the afore-mentioned studies have targeted the question regarding the type of fibrillation occurring in fibrotic tissue (whether it is of a multiple wavelet or of the mother rotor type) and how this depends on the properties of the cardiac tissue.

In this paper, we use a human ventricular cardiomyocyte model to study the effect of spatial heterogeneity of diffuse fibrosis on the onset of cardiac arrhyth-mias. For that, we developed a generic spatial model of fibrosis, which allowed us to change the degree of heterogeneity of fibrosis (amount of difference in lo-cal fibrosis levels) and the characteristic size of the heterogeneity (size of tis-sue patches with a constant fibrosis level). Our study focuses on the question whether heterogeneity in the distribution of fibrosis is an important additional factor contributing to the onset of cardiac arrhythmia. In addition, we aim to answer how this depends on both the degree and the characteristic size of the heterogeneity. Finally we study how heterogeneous fibrosis affects spatiotempo-ral arrhythmia dynamics and characterise whether fibrillation is of the mother rotor or of the multiple wavelet type, and how this may depend on tissue char-acteristics.

3.2 Methods

3.2.1 Mathematical Model

We used the ten Tusscher and Panfilov model [40, 41] for simulating the be-haviour of a ventricular cardiomyocyte:

$$C_m \frac{dV}{dt} = -I_{\text{ion}}(V, \ldots),$$

where V is the transmembrane voltage for the cardiomyocyte, C_m is the mem-brane capacitance, and I_{ion} is the sum of all ionic currents, which depends on V, on the gating variables, and on the concentrations of intracellular calcium. We used the set of parameters that corresponds to a slope of 1.1 of the restitution curve as described in [40, 41].

Fibroblasts were assumed to be inexcitable and electrically disconnected from the myocytes, causing them to be passive obstacles for wave propagation.

For our spatial model of a 2D cardiac tissue with fibrosis, we used a rectan-gular grid with a size of 512×512 nodes, where each node can be occupied by either a cardiomyocyte or a fibroblast. Thus, we assume that the area occupied by a cardiomyocyte is the same as the area occupied by a fibroblast—a square with the size of 250 μm.

Following these assumptions the spatial model can be described as:

$$C_m \frac{dV_{ik}}{dt} = \sum_{\alpha,\beta \in \{-1,+1\}} \eta_{ik}^{\alpha\beta} g_{\text{gap}} \left(V_{i+\alpha,k+\beta} - V_{ik}\right) - I_{\text{ion}}(V_{ik}, \ldots), \qquad (3.1)$$

where (i, k) is a position of a node occupied by a cardiomyocyte (because of the non-conducting character of fibroblast, computation of voltage is not needed in points occupied by fibroblasts), g_{gap} is the conductance of the gap junction channels that couple two neighboring myocytes, and $\eta_{ik}^{\alpha\beta}$ is the connectivity tensor that describes the presence of electrical coupling between neighboring myocytes and the absence of coupling between myocytes and fibroblasts:

$$\eta_{ik}^{\alpha\beta} = \begin{cases} 1, & \text{if the node } (i+\alpha, k+\beta) \text{ is occupied by a myocyte} \\ 0, & \text{otherwise.} \end{cases} \qquad (3.2)$$

Conductance of the gap junctions g_{gap} was taken to be 103.6 nS, which results in a maximum velocity planar wave propagation in the absence of fibrotic tissue of 72 cm/s at a stimulation frequency of 1 Hz, in agreement with clinical data [109].

3.2.2 Fibrosis Distribution

To generate a uniform fibrosis distribution with a mean level of fibrosis of f, we set each node of the grid to be either a fibroblast with the probability f or a myocyte with the probability $(100\% - f)$.

For generating a heterogeneous distribution of fibrotic tissue, we used two extra parameters: the extent of heterogeneity σ and the spatial size of heterogeneity l. We divided the 2D tissue into squares of the size $l \times l$. For each square, we assigned a certain local fibrosis level. We used 4 possible values for to assign local fibrosis levels:

$$\left\{ f - \frac{\sigma}{2}, f - \frac{\sigma}{6}, f + \frac{\sigma}{6}, f + \frac{\sigma}{2} \right\}.$$

Thus, the meaning of σ is the difference between the maximal and the minimal possible local fibrosis levels. After assigning the local fibrosis level f_{loc} for a square, we set each node within that square to be a fibroblast with the probability f_{loc} or a myocyte with the probability $(100\% - f_{\text{loc}})$.

As one can see, our choice of representing the degree of heterogeneity σ implies the following restriction:

$$\sigma \leq \min\left(2f, 100\% - 2f\right),$$

since the local fibrosis level can be neither smaller than 0% nor larger than 100%.

3.2.3 ECG Computation

The (pseudo-)ECG was computed using the following formula:

$$\text{ECG} = \sum_{0 \leq i,k < 512} z(i,k) \sum_{\alpha,\beta \in \{-1,+1\}} \eta_{ik}^{\alpha\beta} (V_{i+\alpha,k+\beta} - V_{ik}),$$

where the transfer function $z(i,k)$ was determined by:

$$z(i,k) = \left[(i - i')^2 + (k - k')^2 + d^2 \right]^{-\frac{1}{2}}$$

and the measuring point (i', k', d) was positioned at $(256, 256, 100)$, that is, at a distance of 2.5 cm along the z-axis above the centre of the 2D tissue.

3.2.4 Ablation Modeling

The (pseudo-)ablations were modelled by changing the connectivity tensor η. If a node occupied by a cardiomyocyte underwent an ablation procedure, the cardiomyocyte was replaced by an empty node, and the connectivity tensor η was recomputed in accordance with (3.2).

3.2.5 Implementation

The system of coupled ordinary differential equations (5.1) was solved by the forward Euler integration method, using the timestep of 0.02 ms, similar to previous studies [40, 41]. The equations for gating variables were integrated using the Rush-Larsen algorithm.

The numerical solver was implemented with the C and C++ programming languages, using the CUDA toolkit for performing the majority of computations on graphical processing units. The auxiliary tools for manipulating the connectivity tensor, visualisation, and computing the ECG were implemented using the OCaml programming language. Computations were performed with single precision and run on an Intel Core i7-3930K machine with two GeForce GTX 780 Ti graphics cards.

The random number generator was taken from [110]. The seed for the random number generator was taken independently for each simulation.

3.3 Results

3.3.1 Heterogeneous vs Homogeneous Fibrosis

We studied the induction of arrhythmias by high frequency pacing for homogeneous and heterogeneous distributions of diffuse fibrosis. We applied a burst pacing protocol of 10 stimuli with a period of 240 ms and monitored the

$t = 2.3\ s$ $t = 2.7\ s$ $t = 3.1\ s$
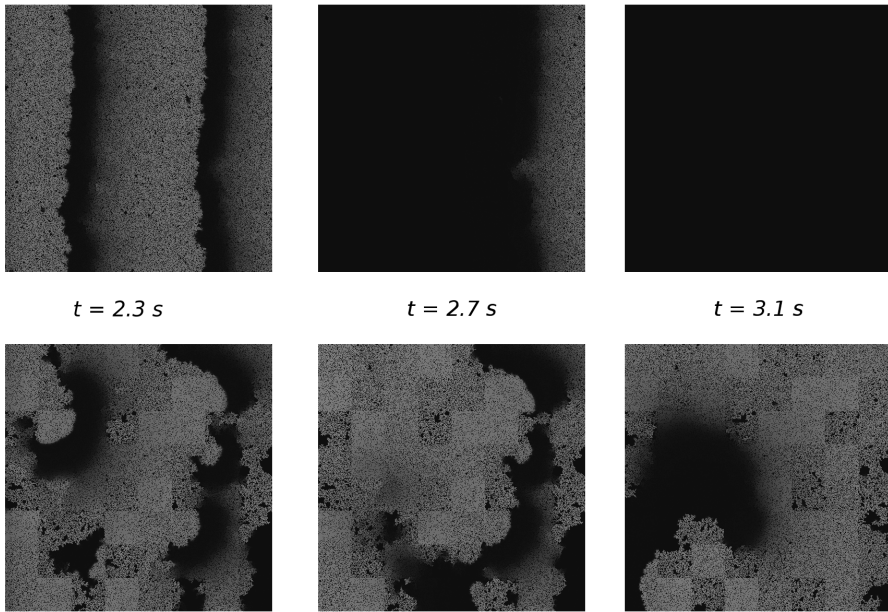
Figure 3.1. Induction of reentry by burst pacing. The electrical activity is given for the moment when the last stimulus is delivered ($t = 2.3$ s), for 0.4 s after that, and for 0.8 s after that. The shade of grey shows the transmembrane voltage. Top row: homogeneous fibrosis of 25%; bottom row: the same amount of mean fibrosis distributed heterogeneously ($\sigma = 25\%$, $l = 16$ mm). Left column: the state of the medium after delivery of the last stimulus. Middle column: the state of the medium when the last pulse leaves it. Right column: the activation pattern established after termination of stimulation.

induced activity. Fig. 3.1 shows the results of typical simulations. The top row corresponds to a homogeneous fibrosis distribution with a mean level of fibrosis $f = 25\%$. The bottom row shows the results for a heterogeneous distribution of fibrosis with the same mean level f, an extent of heterogeneity of $\sigma = 25\%$ and a heterogeneity size $l = 16$ mm. For the homogeneous distribution, the electrical activity vanished with the termination of pacing (shown in the top right part of Fig. 3.1). However, for the heterogeneous distribution, we observed sustained electrical activity.

To study the effects of mean fibrosis level (f), extent of heterogeneity and (σ) and spatial size of heterogeneity (l) we performed a large series of simulations for different combinations of parameter values (f, σ, l). However, we observed that the outcome of our simulations, whether or not sustained electrical activity occurs, was highly stochastic in nature. The results depended not only on the mean value of fibrosis and the pattern of heterogeneity, but also on the specific locations of randomly distributed fibrotic cells. Because of this stochasticity, we generated for each specific (f, σ, l) parameter setting 50–100 different fibrosis patterns, by using different seeds for the random number generator before creating the pattern. We subsequently performed a statistical analysis of our simulation results, determining the boundary between parameter settings for which at least 25% of simulations results in persistent spiral wave activity and parameter settings for which fewer simulations result in persistent electrical activity.

In the top panel of Fig. 3.2, we show two phase diagrams illustrating the effect of heterogeneity of fibrosis on reentry generation. In each of the diagrams, there are two regions marked with "reentry" and "no reentry" which correspond to parameter settings for which the probability of inducing reentrant activity is higher or lower than 25% respectively. In Fig. 3.2a, this phase diagram is shown for the σ—f parameter space when $l = 12.5$ mm. We can see that reentrant activity occurs for homogeneous fibrosis ($\sigma = 0$) if the mean fibrosis level $f \approx 28\%$ and higher. With the increase of heterogeneity σ, the minimal value of the mean fibrosis level f required for reentry formation decreases linearly. In Fig. 3.2b, a similar phase diagram is given in the σ—l parameter space with fixed $f = 25\%$. We see that reentrant activity is more difficult to trigger for smaller values of the size of heterogeneity l. The boundary separating the two regions has a hyperbolic shape.

To further investigate the effect of heterogeneity size l on reentry generation, we calculated phase diagrams in the σ—f parameter space for two additional values of l. Fig. 3.3 shows the results of these simulations. We see that for a smaller size of l, the boundary becomes less steep, whereas for a larger l, the slope becomes steeper (more negative). We can interpret these results as follows. If we consider the case of a very small value of l the difference between heterogeneous and homogeneous fibrosis disappears due to spatial averaging. Therefore, we expect that the probability of arrhythmia induction for this case is the same as for the case of homogeneous fibrosis and does not depend on the extent of het-

(a)

(b)
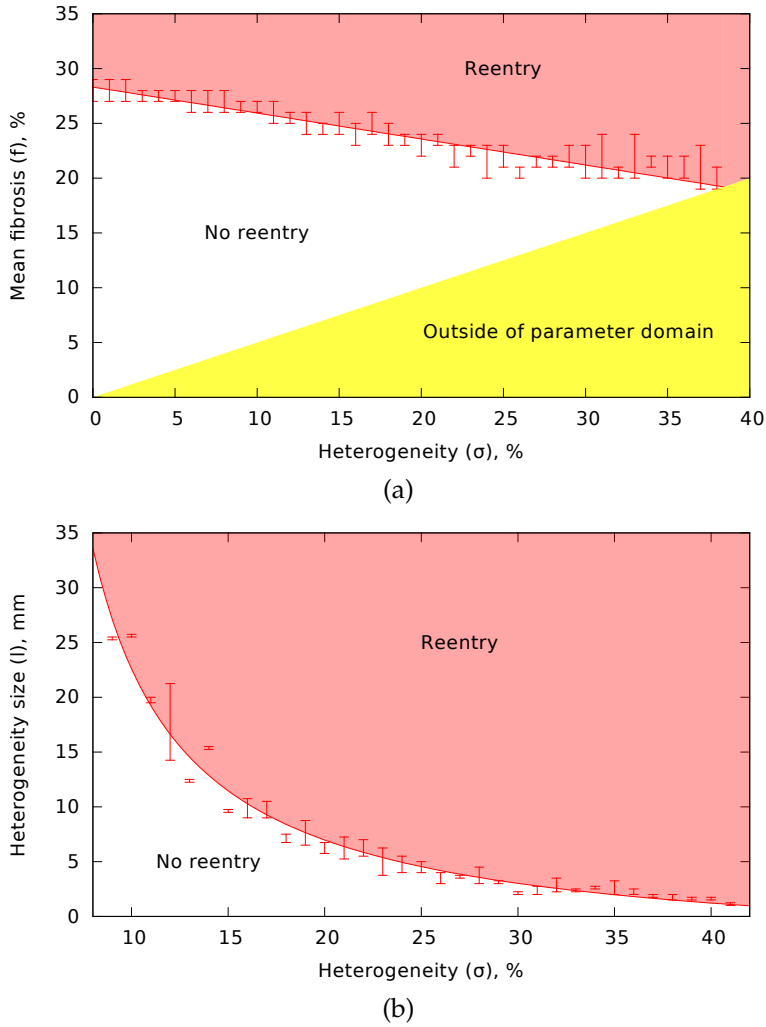
Figure 3.2. Effect of the mean fibrosis f, the width of fibrosis distribution σ, and the size of heterogeneity l on the probability of reentry generation: (a) phase diagram for σ and f when $l = 12.5$ mm; (b) phase diagram for σ and l when $f = 25\%$. In the regions labelled "reentry" the induced activity occurs in more than 25% of cases. The yellow region shows undefined parameter combinations where $\sigma < 2f$ (see Methods).

(c)

Figure 3.3. Same as Fig. 3.2a but also include different values of l. The dark green and the dark blue lines are theoretical estimations for the boundary for very small or very large l respectively. The light green and the light blue points are the results of simulations for $l = 8.0$ mm and $l = 64.0$ mm respectively. The red line is the fit to the simulation data.

(a)   (b)

Figure 3.4. Two examples of persistent activation patterns emerged in the heterogeneous fibrotic medium by burst pacing: (a)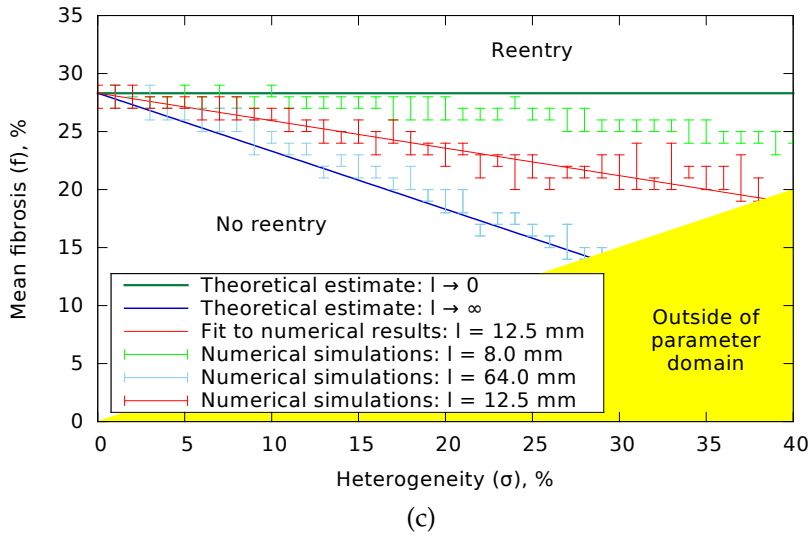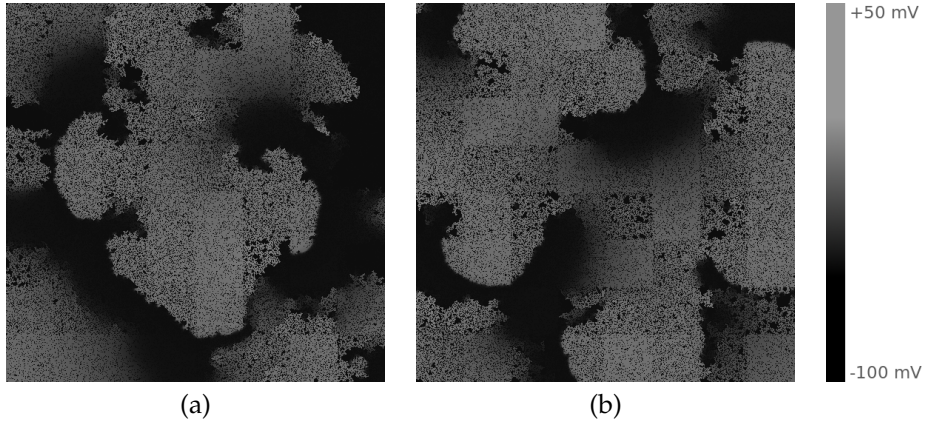 arrhythmia mediated with a single independent spiral (Pattern A); (b) multiple wavelets fibrillation (Pattern B). For these simulations, the values of the parameters are the same as for the simulations presented in Fig. 3.1: $f = 25\%$, $\sigma = 25\%$, $l = 16$ mm.

erogeneity σ. This corresponds to the horizontal green line in Fig. 3.3. We indeed see that the boundary computed for $l = 8$ mm (light green points) approaches that line. This indicates that heterogeneity at a small spatial scale has much less influence on the probability of spiral wave formation.

On the other hand, if we consider the case of a relatively large l, then the patches of fibrosis can be considered independent, in the sense that each of them can be considered as a region with homogeneous fibrosis. The value of such local fibrosis ranges from $(f - \sigma/2)$ to $(f + \sigma/2)$. As the probability of reentry initiation increases with an increase in fibrosis level, the wavebreaks most often occur in the regions with the highest fibrosis density, which is $(f + \sigma/2)$. For reentry initiation this percentage should be larger than 28%; therefore, we expect that for a very large value of l, the reentry in heterogeneous tissue will occur if $f + \sigma/2 \geq 28\%$. This line is shown with the dark blue colour in Fig. 3.3. We see that our numerical results for $l = 64$ mm (light blue points) are in agreement with this theoretical prediction.

Overall, the phase diagrams demonstrate that a heterogeneous distribution increases the likelihood of arrhythmia onset relative to a homogeneous distribution. Furthermore, they show that the main mechanism of this dependency is the presence of localised tissue patches with larger level of fibrosis.

3.3.2 Spatiotemporal Characteristics of the Activation Patterns

The induced activation patterns can comprise either only a single spiral (as in Fig. 3.1) or multiple wavebreaks. Two representative examples of the latter

(a)   (b)

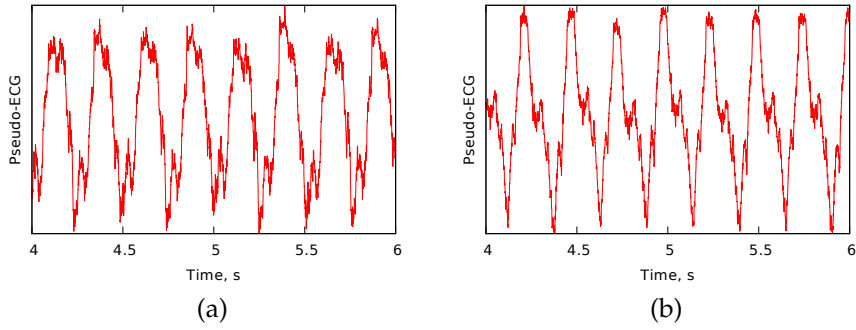**Figure 3.5.** Pseudo-ECG for (a) Pattern A and (b) Pattern B.

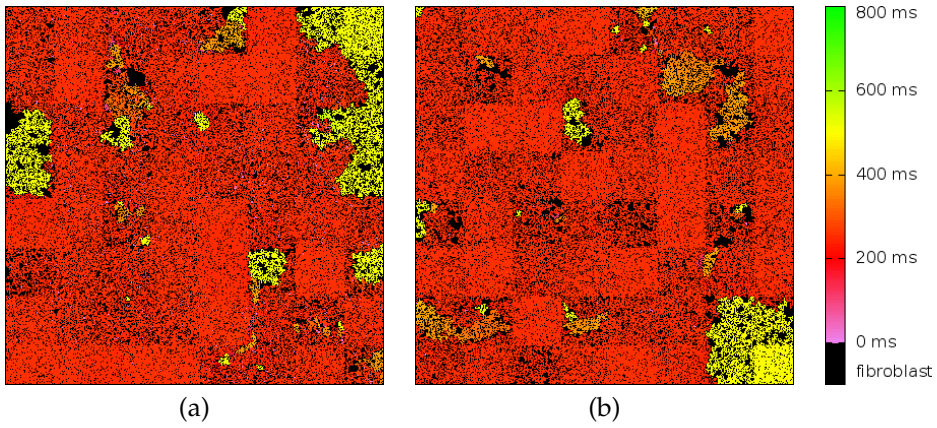(a)   (b)

Figure 3.6. Maps of the interbeat interval for (a) Pattern A and (b) Pattern B. Positions of inexcitable fibroblasts are shown in black.

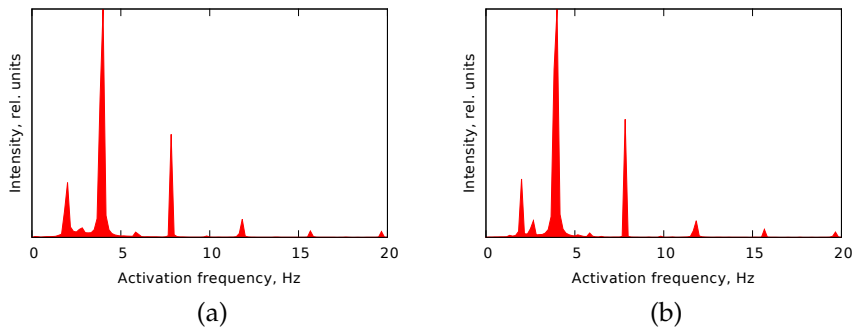(a)   (b)

Figure 3.7. Frequency distibution profiles for (a) Pattern A and (b) Pattern B.

case are demonstrated in Fig. 3.4. We see that the patterns resemble fibrillatory activity. These patterns look fairly similar but, as we will show later, there is a difference between them with respect to the ease of terminating their activity by means of an ablation procedure. We will refer to these representative patterns as Pattern A (Fig. 3.4a) and Pattern B (Fig. 3.4b).

The spatial patterns in Fig. 3.4 look irregular and chaotic. We investigated whether this holds for the overall electrical activity by three approaches. As a first approach, we calculated the ECG generated by these excitation patterns, shown in Fig. 3.5. As it can be observed from the figure, even though the ECG for both patterns is slightly irregular, the ECG is highly periodic in nature. As a second approach we computed spatial interbeat interval maps produced by the two activation patterns (Fig. 3.6). In the figure we see that in spite of the heterogeneity in local fibrosis density, the interbeat intervals distribution is largely homogeneous across space, except for a few regions where the interbeat interval is twice as long as in the adjacent areas. This type of spatial interbeat interval distribution is similar to the frequency domains reported during ventricular and atrial fibrillation [111, 112] and indicate regions of 1:2 Wenckebach block [113]. Finally, as a third approach we computed mean distribution profile of the activation frequency, shown in Fig. 3.7. As we can see, the two profiles look almost identically. The dominant frequency peak is at about 4 Hz with a smaller peak at about 2 Hz corresponding to Wenckebach period doubling. This Wenckebach doubling is responsible for the 1:2 component that can be observed in the ECG signal. Based on these results, we conclude that the activation patterns are highly periodic. Similar observations have been reported in experiments with cell cocultures of myocytes and fibroblasts [65, 104].

Because of the periodicity of the resulting patterns, it was possible to measure the period and investigate its dependency on the fibrosis distribution.

Period of the Activation Patterns

We investigated how the period of the activation patterns depends on the amount and distribution of fibrosis. The dependency of the period on the size of heterogeneity for a constant mean fibrosis level of $f = 25\%$ is given in Fig. 3.8a. We see that period increases with the increase of l and saturates for $l \geq 20$ mm. Similar to our earlier results, the excitation period for the small sized heterogeneity is the same as for homogeneous fibrosis with the same average level. To study what determines the saturated plateau level, we investigated how the period for a constant sized heterogeneity of $l = 40$ mm depends on the extent of heterogeneity σ and the average fibrosis level f. These results are given in Fig. 3.8b. For the uniform fibrosis distribution (the red line), we see that period increases superlinearly with the increase of the average fibrosis level f, so the rotation of the spiral waves is slowed down in the presence of fibrosis. This is consistent with the earlier studies [100, 104]. We also see that for heterogeneous fibrosis

patterns, the increase in period with average fibrosis levels becomes stronger as the extent of heterogeneity in fibrosis levels increases.

As the shapes of the graphs obtained for different heterogeneity values look similar to each other, we tried to characterise this similarity formally. We found that the graphs will reasonably well match one another if there are all shifted horizontally by $\sigma/2$ (Fig. 3.9). This shift means that to obtain the same period of activation for homogeneous fibrosis as for fibrosis with a heterogeneity of σ, we need to use an average fibrosis level of $(f + \sigma/2)$ for the homogeneous case versus an average fibrosis level of f for the heterogeneous case. As $(f + \sigma/2)$ corresponds to the maximal level of fibrosis in heterogeneous tissue, we can conclude that the period for heterogeneous fibrosis is mostly determined by the maximal local fibrosis level, or in other words, by the region where the spiral rotation is slowest.

3.3.3 Underlying Mechanism of the Activation Patterns

As we showed, despite irregular appearing of spatiotemporal wave patterns, the electrical activation patterns are highly periodic and regular. As the tissue is heterogeneous, these findings may indicate that fibrillation is driven by a single periodic source of excitation, and that the arrhythmia is of the mother rotor type [114]. In the case of mother rotor fibrillation, it is assumed that all wavelets originate from the interaction of a single persistent high frequency source with tissue heterogeneity [114]. To prove that a pattern is of the mother rotor type, one needs to find and remove the mother rotor and demonstrate that fibrillation terminates. This is rather difficult to achieve in experiments but can be done easily in numerical simulations. by applying highly targeted virtual ablation of cardiomyocytes.

To classify the type of the activation patterns, we first performed "local ablations". For this we subdivided the 2D tissue into 64 equally sized squares of size 16×16 mm. During an individual local ablation experiment, we "removed" one of these squares, similar to performing a clinical point ablation procedure, replacing the active cardiomyocytes in this region of the tissue by passive "dead" cells.

The results of applying this procedure for our representative examples are demonstrated in Fig. 3.10. The top pictures correspond to Pattern A. We see that some ablations do not affect the activation pattern (top middle), maintaining the previous number of waves. However, in other cases (top right), the pattern changes drastically, and reduces to a single spiral wave anchored to the ablation site. For Pattern B (bottom row), similar results were obtained. To represent the results of all 64 possible ablation locations, in Fig. 3.11, we show the period of rotation after performing each of these ablations. As we can see, for Pattern B (the blue line), the ablations do not affect the period of activation. On the other hand, for Pattern A (the red line), while most ablation sites still do not alter the
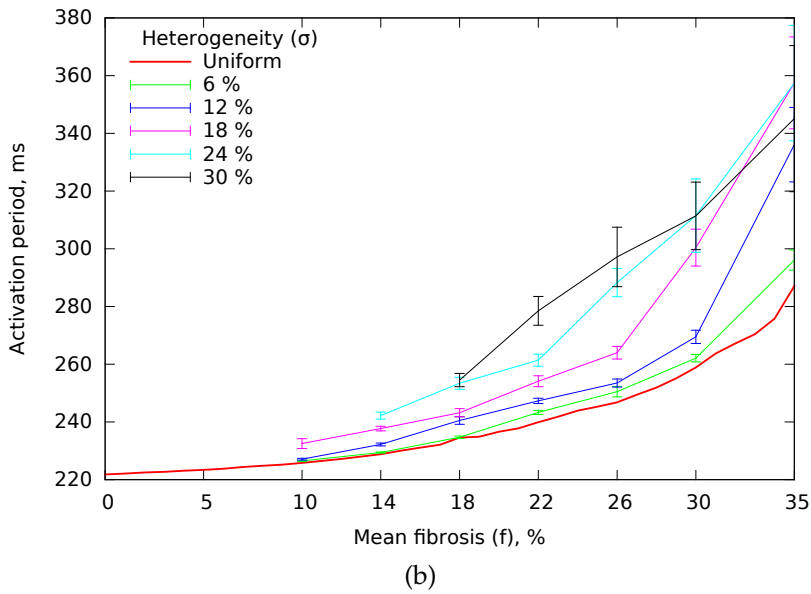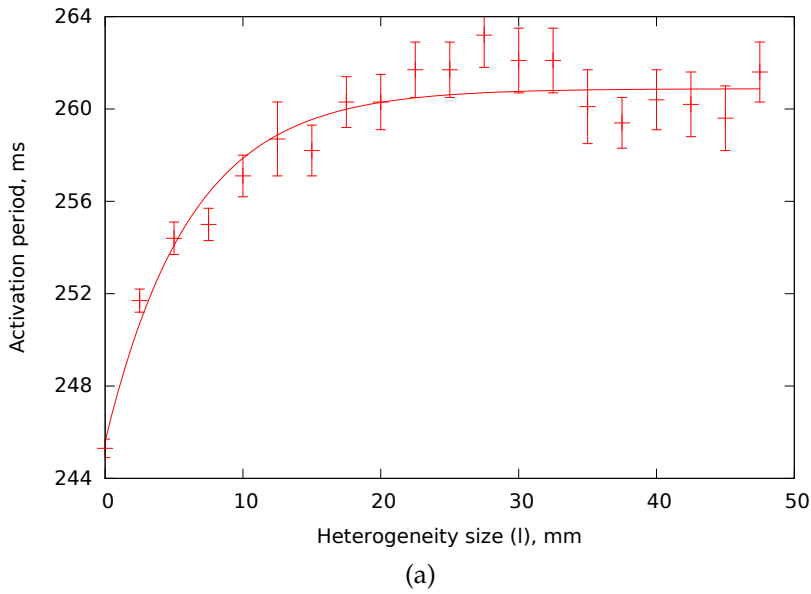
(a)

(b)

Figure 3.8. Period of the activation pattern depending on the fibrosis distribution: (a) dependence of the period on the size of heterogeneity l for $f = 25\%$ and $\sigma = 18\%$; (b) dependence of the period on the mean fibrosis f for different values of heterogeneity σ and $l = 40$ mm.
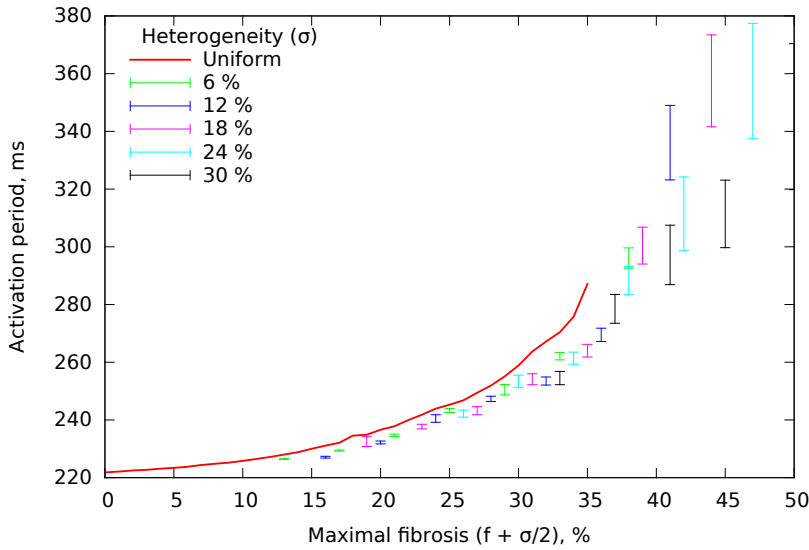
Figure 3.9. Dependence of the activation period on the value of maximum local fibrosis level ($f + \sigma/2$) for different values of heterogeneity σ; for these simulations $l = 40$ mm.

period, a subset of ablation sites exist that result in a significant increase in period of activation, indicative of a substantial slowing down of wave patterns.

In the case of rotors, small, localised ablations are unlikely to remove them. Indeed to terminate spiral wave rotation it is necessary to connect the core of the rotor to the boundary of the medium [115], effectively forcing the rotor to drift out of the tissue. Therefore, we also performed "line ablations", a procedure in which a line-shaped ablations was performed that connected a certain place in the tissue to the nearest boundary. We again performed this procedure for the 64 possible locations corresponding to the centres of the 64 squares we previously used for local point ablations.

A few examples of the application of this line ablation procedure are given in Fig. 3.12. The top row corresponds to Pattern A. We see that there are ablations that do not change the activation pattern (the middle part of the figure). However, for other positions, where the ablation line connected the core of the spiral to a tissue boundary, we observed termination of the arrhythmia (top right part) as a result of the ablation. The three bottom pictures correspond to Pattern B. Here, we never the observed termination of the arrhythmia for any ablation position we chose. These results allow us to conclude that Pattern A is of the mother rotor type and Pattern B is of the multiple wavelet type.

These methods for determining the type of fibrillation can easily be implemented as an automatic procedure, allowing us to perform a large number of
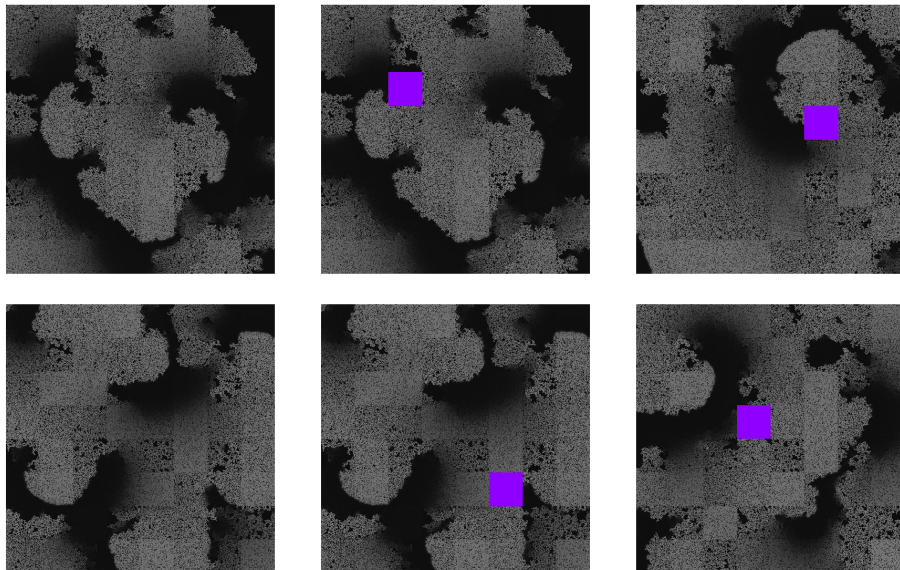
Figure 3.10. Changes in activation patterns as a result of "square ablation": removing a small square-shaped part of the tissue. The shade of grey corresponds to the transmembrane voltage. The ablated parts of the tissue are shown in violet. The top row is for Pattern A, and the bottom is for Pattern B. Left column: the activation picture without applying ablation; middle column: ablation performed at a distance from the spiral core; right column: ablation performed at the location of the spiral core.
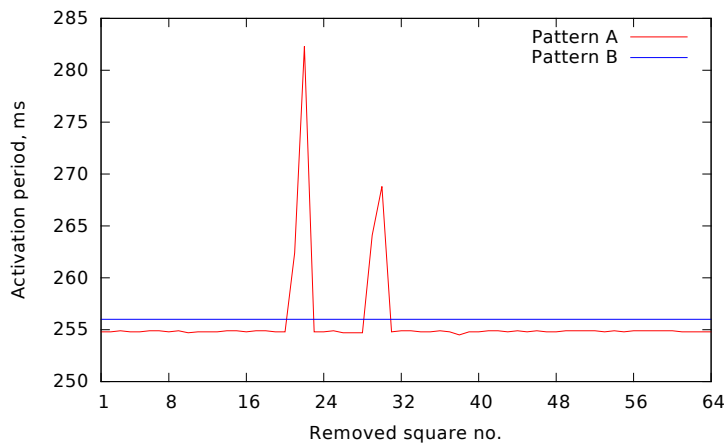
Figure 3.11. The effect of "square ablation" on the period of Pattern A and Pattern B. The x axis corresponds to the number of the removed part from the 64 possible subdomains.
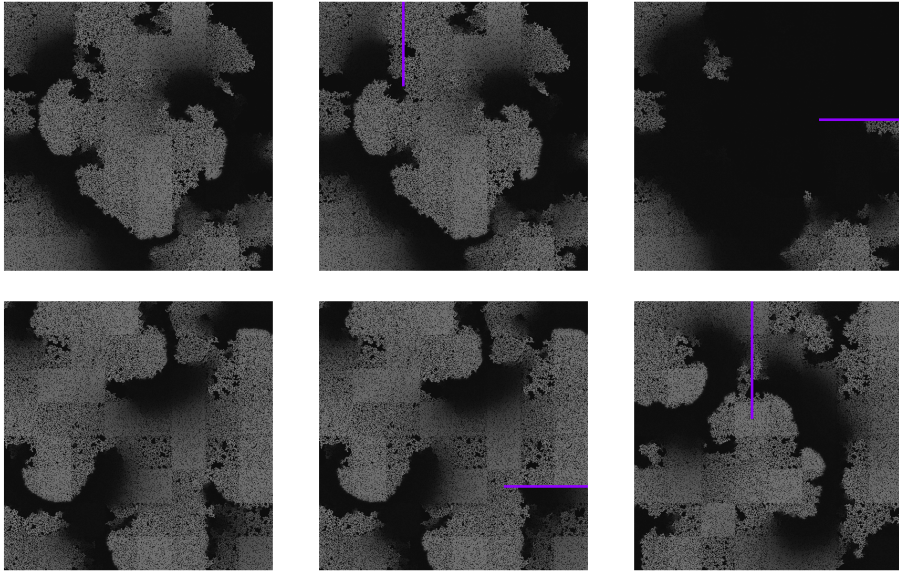
Figure 3.12. Changes in activation patterns as a result of "line ablation." Shade of grey corresponds to the transmembrane voltage. Ablations are shown with violet. The top row corresponds to Pattern A and the bottom row to Pattern B. Left column: the activation picture without applying ablation. Middle column: the line ablations where the lines do not go to the cores of the spirals. Right column: line ablations where the lines connect the cores with the boundary.

(a)

(b)

(c)
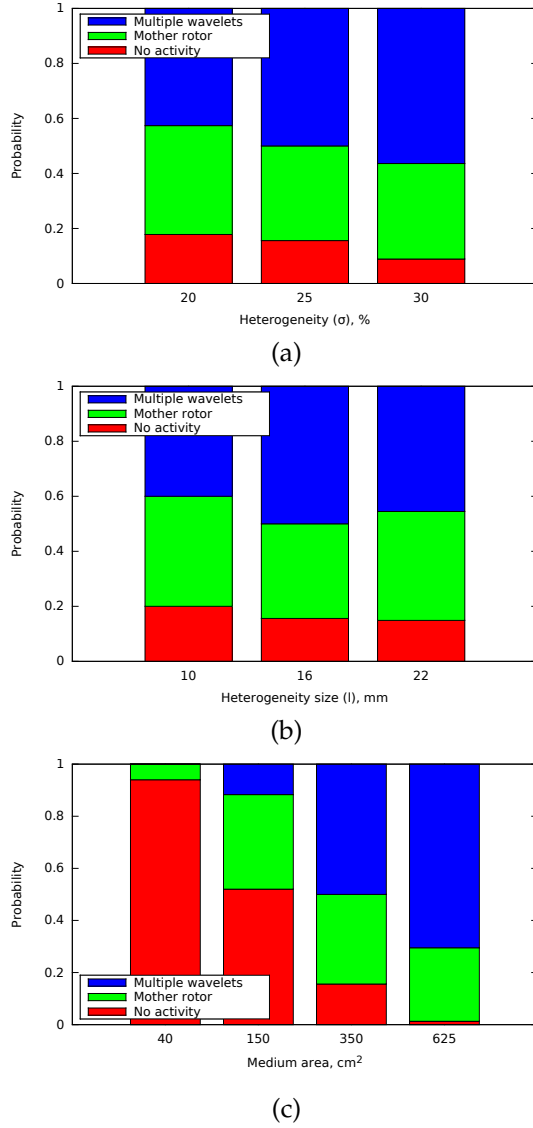
Figure 3.13. Dependency of the type of the activation pattern on (a) the value of heterogeneity, (b) the size of heterogeneity, and (c) the tissue size. The basic set of the parameter values used for these results is $f = 25\%$, $\sigma = 25\%$, $l = 16$ mm, and tissue size of 350 cm^2. "No activity" means that the burst pacing protocol did not lead to the emergence of persistent activation. The "mother rotor" type of activation pattern was possible to terminate by connecting the core with the boundary. For the "multiple wavelets" type, no cuts of the medium could terminate the arrhythmia.

such ablation procedures and subsequent classifications. We used this approach to determine how fibrillation type depends on value of heterogeneity, heterogeneity size, and the tissue size. Fig. 3.13 shows the results of our simulations. In Fig. 3.13, red indicates absence of induced activity, green indicates mother rotor type fibrillation, and blue indicates multiple wavelet type fibrillation. The sum of the green and blue parts of the column thus indicates the probability of arrhythmia induction. In Fig. 3.13a, we see that for the larger heterogeneity value the number of cases with multiple wavelet fibrillation increases. The change of the size of heterogeneity within the limits shown in the figure had no significant effect (Fig. 3.13b). The effect of the tissue size was more pronounced (Fig. 3.13c). We used values of the tissue size of 40 cm^2, 150 cm^2, 350 cm^2, and 625 cm^2. For a tissue size of 150 cm^2 the probability of arrhythmia induction is approximately 50%, and from the blue-green ratio it follows that for the subset of cases that arrhythmia induction occurs 80% of them corresponds to mother rotor type fibrillation. For a smaller tissue of 40 cm^2 we see that the probability of arrhythmia induction is significantly lower. In addition, it is no longer possible to induce multiple wavelet type fibrillation. If instead we consider larger sized tissues we observe the reverse phenomenon, with the probability of arrhythmia induction increasing and a larger fraction of induced fibrillation being of the multiple wavelet type. For example, for a tissue of 625 cm^2, arrhythmia induction occurs in almost all cases, and in 75% of these cases it will be of the multiple wavelet type.

Note, that while the larger tissue sizes studied here appear to lie outside the physiologically relevant domain (that is, the size of the human heart), we did not include tissue anisotropy in our current simulations. Adding anisotropy, that is, slower propagation in the transversal direction, is equivalent to an decrease in effective tissue size [116].

Considering a typical propagation velocity anisotropy of 1:3, an isotropic tissue of size $10 \text{ cm} \times 15 \text{ cm} = 150 \text{ cm}^2$, corresponds to an anisotropic tissue of size $10 \text{ cm} \times 5 \text{ cm} = 50 \text{ cm}^2$. On a similar note the 350 cm^2 re-scale to 116 cm^2 and the 625 cm^2 to 207 cm^2. We estimate the surface area of the left human ventricle to be around 160 cm^2 (see Appendix A).

3.4   Discussion

Fibrosis is an important risk factor for arrhythmogenesis since it affects propagation of the excitation wave. It was shown that the fibrosis texture, that is, the layout of fibroblasts, is a more important factor for the onset of arrhythmias than an average level. In this work, we investigated the contribution of the heterogeneity in the distribution of fibrosis in cardiac tissue on arrhythmia formation. We have shown that the heterogeneity of fibrosis promotes the onset of arrhythmias. This effect depends on both the spatial size and the degree of the

heterogeneity: a larger size and larger degree of heterogeneity make formation of arrhythmias more probable.

The results in Fig. 3.2a illustrate that for very small spatial heterogeneity, arrythmogenecity is the same as for homogeneous fibrotic tissue with the same average fibrosis density. Therefore, the degree of heterogeneity is not relevant for this case. For very large spatial heterogeneity arrhythmogenic potential is the same as for homogeneous fibrotic tissue with a fibrosis density equal to the maximum fibrosis density occurring in the heterogeneous tissue. Thus, for larger size of heterogeneity, not the heterogeneity itself but rather the patch with maximum fibrosis density is relevant for the arrhythmogenic potential of the fibrotic tissue. Since, for these two cases, the probability of arrhythmia induction is determined solely by local fibrosis, we assume that it is also true for the intermediate sizes of spatial heterogeneity. This assumption, taken together with the central limit theorem, allows us to explain the hyperbolic shape of the boundary in the σ—l parametric space (Fig. 3.2b). A detailed derivation is given in Appendix B.

A more detailed study revealed that not only the inducibility of arrhythmia, but also period of activation is determined by the highest level of local fibrosis. This result demonstrates that the arrhythmia sources tend to lie in the regions with the highest fibrosis level. This correlation potentially allows to predict the position of the mother rotor for ablation therapy. A similar correlation between the positions of the rotors and the fibrosis layout has been reported in [112, 117]. The mechanism responsible for this effect requires additional study.

Another result of our study is the characterisation of the nature of fibrillatory arrhythmias occurring in our model of heterogeneous fibrotic tissue. We found that while spatiotemporal wave patterns look irregular the electrical activity patterns of the arrhythmias have a quite regular, periodic structure. This result indicates that fibrillation is not caused by the type of dynamical instabilities that occur due to a steep restitution curve [63, 64]. This is in line with the earlier results [100], where it was shown that the slope of the restitution curve is lower for the values of period of spiral rotation that correspond to fibrotic tissue.

We found that in our case two types of fibrillation are possible: mother rotor and multiple wavelets. These two fibrillation types require different ablation protocols for termination of activity. For the case of multiple wavelets, in addition to normal ablation, one should consider either subdividing the tissue into smaller domains where only the mother rotor fibrillation type is possible (as shown in Fig. 3.13c) or trying to ablate the rotors by multiple ablation lines.

The mother rotor activation patterns that we obtained are different from the fast mother rotors that were observed in [118]. In Fig. 3.6a, where the spatial distribution of activation period is given, we do not see any higher frequency regions at the position where the mother rotor is located. Whereas in [118], the position of the mother rotor correlates with the maximal local activation frequency. In Fig. 3.6a, where the spatial distribution of the activation period is given, we do not see any higher frequency regions at the position where the mother rotor

is located.

The strong periodicity of the activation patterns may indicate the presence of a mother rotor [112, 119]. We indeed found that for tissue sizes less than 150 cm^2 (which corresponds to 50 cm^2 in the anisotropic case), most of arrhythmias were of the mother rotor type (Fig. 3.13). Even for the tissue as large as 625 cm^2 (≈ 208 cm^2 in the anisotropic case) we still observe mother rotor type fibrillation in 30% of the cases. Interestingly, the multiple wavelet type of fibrillation never occurred for small tissues of 40 cm^2 (≈ 13 cm^2 in the anisotropic case). Therefore, in most realistic cases, one would expect fibrillation to be of the mother rotor type. This may explain why ablations of rotors may remove atrial fibrillation [120]. However, it is still not clear why ablational targeting only the rotor core along is considered effective. In our model, only ablations that connect the spiral core with the boundary of the tissue could effectively terminate the arrhythmia.

In the current study, arrhythmias were induced by a burst pacing protocol. Another commonly used method of triggering arrhythmia is the S1S2 protocol. Our choice for the burst pacing was mainly because this way it is possible to see if arrhythmia can be induced for a particular fibrosis layout. In contrast, the S1S2 protocol always leads to arrhythmia initiation; fibrosis may only contribute to generation of additional excitation sources which may be due to a mechanism that is different from the mechanism of formation of the initial source. Nevertheless, the S1S2 protocol is required for studies targeting the transition from tachycardia to fibrillation which will be addressed in the subsequent research.

Although the probability of the onset of arrhythmias is certainly affected by the stimulation frequency, we expect that this dependency does not significantly change the main results of our paper. Indeed, the results regarding the period of the arrhythmia and its nature were studied after pacing was stopped and should, therefore, not be affected by the initiation procedure. Clearly, as it is known that higher pacing frequencies independently lead to an increase in the likelihood of arrhythmia induction, an increase in the frequency of burst pacing is expected to shift the boundaries on the phase diagrams in Fig. 3.2 downwards. We can also estimate the lower limit for the leftmost point of the graph presented in Fig. 3.2a for any value of the pacing period by the following way. As it was shown in [121–123], to generate a rotor at a geometrical obstacle one needs to pace the tissue with a period that is shorter than the period of spiral wave rotation in that tissue. Therefore, the leftmost point in Fig. 3.2a should be higher than the level of fibrosis that corresponds to the spiral rotation period equal to the given pacing period. In our case, the pacing period of 240 ms corresponds to the period of spiral wave rotation in a homogeneous tissue with a mean fibrosis level of 22%. This number is smaller than 28% of fibrosis level that is necessary for having reentry in 25% of the cases.

As it is the case for any modeling study, our model represents a simplified description of fibrotic cardiac tissue and as such it has several limitations. A first

major model simplifications is to consider solely the effects of structural remodeling. Under many disease conditions the structural remodeling is accompanied by electrical remodeling. Often, the degree of fibrosis is in correlation with the degree of electrical remodeling as well as the extent of ionic heterogeneity. Both electrical remodeling *per se* and ionic heterogeneity are additional factors enhancing the drift of spiral waves [22, 124] and the onset of wavebreaks and arrhythmias [21, 125]. Therefore, we expect that adding electrical remodeling to our model would facilitate arrhythmogenesis.

A second important limitation in the current model is the assumption that myocytes and fibroblasts are not electrically coupled, while some experimental studies indicate that this under some conditions this coupling be the case [126]. However, the issue of such coupling is controversial, with some researchers implying that it exists only in *in vitro*, while others assume that this coupling occurs in cardiac tissue and is facilitated by tissue remodeling. The effect of this coupling requires additional study, outside the scope of our current research. However, we can suggest that in accordance with experiments by [104] this coupling promotes arrhythmogenesis, therefore, it would probably shift the boundaries on the phase diagrams in Fig. 3.2 downwards.

It should be noted, however, that while the above model simplifications can be interpreted as too strong, they, in fact, are crucial to allow us to study the effect of fibrosis as obstacles to wave propagation in isolation, without other tissue remodeling factors or other characteristics of fibrosis itself obscuring the results.

A third limitation was that we considered only one type of fibrosis: diffuse fibrosis. Other types of fibrosis are: compact, interstitial, and patchy [27]. It has been reported that patchy fibrosis causes more problems for wave propagation than diffuse fibrosis. The same is valid for interstitial fibrosis if one considers propagation across the fibre direction [27]. On the other hand, compact fibrosis is considered to be the least arrhythmogenic type. Therefore we expect that both patchy and interstitial fibrosis would facilitate the induction of fibrillation, while for compact fibrosis, it might be not possible to induce the arrhythmia in our model at all. Apart from this, we still expect a strong correlation between both the probability of arrhythmogenesis and the period of activation with local fibrosis densities for patchy and interstitial fibrosis. However, to prove these hypotheses an additional study is required.

Heterogeneity in distribution of diffuse fibrosis was modelled by introduction of rectangular patches with different levels of local fibrosis. The square shape is not physiologically based, however, we assume that a particular shape of the fibrotic region has a little impact on arrhythmogenesis.

A fourth limitation was the absence of anisotropy in our model. There are evidences that fibrosis results in increase of anisotropy ratio for a tissue [127, 128]. Such increase may contribute to breakup formation as it was demonstrated for cell cultures and in simulations studies [129]. Therefore, we expect that the increase of tissue anisotropy due to fibrosis potentially facilitates arrhythmia trig-

gering.

Finally, taking into account the 3D nature of ventricular cardiac tissue would allow for additional 3D mechanisms of spiral breakup that were previously shown to occur in relation to reduced excitability and fibrosis [101]. On the other hand, for 3D tissue, the connectivity is better than for 2D tissue, therefore breakups that potentially occur in 3D are less crucial for the onset of arrhythmia than for 2D. This way we cannot make reliable predictions how the results regarding arrhythmogenesis would change in 3D.

In addition, we assumed that the fibroblasts and the myocytes are similar in size. In real tissue, the shape and the size of a fibroblast is a debate point. Although, an isolated fibroblast is a rounded cell with a diameter of 7–9 μm, a fibroblasts *in vivo* form membrane extensions, which increase its size and surface area [126]. In cell cultures, the fibroblasts tend to flatten more than the cardiomyocytes, effectively increasing their 2D size. A more detailed approach for generation the tissue texture can be found in [130]. That approach attempts to take both the size and anisotropy into account. There are also more advanced models and methods that incorporate realistic anatomical features with superimposing of fibrosis distribution [107, 108, 131]. In this study, we used the most straightforward way: the size of a node that can be occupied either by a fibroblast or a myocyte was 0.25 cm. Although this way we neglect finer details of tissue architecture, an indisputable advantage of this approach is its computational efficiency.

Overall, we expect that improving upon our model simplifications will mostly affect our outcomes in a quantitative manner, shifting the ratios between mother rotor versus multiple wavelet dynamics, or shifting the phase diagram boundaries separating reentry from non-reentry. We are confident that our qualitative results that heterogeneity of fibrosis is an additional proarrhythmic factor and that this proarrhythmicity stems mostly from the maximum local fibrosis densities occurring within the heterogeneous tissue, are also valid under alternative model settings.

Appendix A

Here, we estimate the surface of the human left ventricle. According to [132], the left human ventricle can be approximated as a part of prolate spheroid with the polar radius of $c \approx 7$ cm, the equatorial radius $a \approx 3$ cm, and the height (apex to base length) $h \approx 10$ cm. The surface area of this body can be computed as a surface of revolution about the z-axis:

$$S = 2\pi \int_{-c}^{h-c} r(z)\sqrt{1 + (r'(z))^2}dz,$$

where the radius $r(z)$ is:

$$r(z) = a\sqrt{1 - \left(\frac{z}{c}\right)^2}.$$

Thus, the integral is:

$$S = 2\pi a \int_{-c}^{h-c} \sqrt{1 - \frac{c^2 - a^2}{c^2}\left(\frac{z}{c}\right)^2}\, dz.$$

Using the eccentricity $e = \sqrt{c^2 - a^2}/c$ and denoting $l = h - c$ we can rewrite the integral as:

$$S = 2\pi a \int_{-c}^{l} \sqrt{1 - \left(\frac{ez}{c}\right)^2}\, dz = \frac{2\pi ac}{e} \int_{-e}^{le/c} \sqrt{1 - \xi^2}\, d\xi.$$

Since

$$\int \sqrt{1 - \xi^2}\, d\xi = \frac{1}{2}\left(\arcsin\xi + \xi\sqrt{1 - \xi^2}\right) + C,$$

we obtain:

$$S = \frac{\pi ac}{e}\left(\arcsin\frac{le}{c} + \frac{le}{c}\sqrt{1 - \left(\frac{le}{c}\right)^2} + \arcsin e + e\sqrt{1 - e^2}\right).$$

Therefore, substituting the numbers we get:

$$
\begin{aligned}
e &\approx 0.90 \\
\frac{le}{c} &\approx 0.39 \\
S &\approx 165\ \text{cm}^2.
\end{aligned}
$$

Appendix B

Here, we illustrate that the hyperbolic dependency of the onset of arrhythmia on the size of the heterogeneity (the boundary in Fig. 3.2b) directly follows from the assumption that the only parameter that determines the probability of spiral wave formation is the local level of fibrosis f_{loc}. Indeed, if we define the local fibrosis level f_{loc} as an average fibrosis in an area of a certain characteristic length a (a-region), then the number of heterogeneous "small squares" of the size l occupying this area is: $n \sim (a/l)^2$. The probability distribution of fibrosis in an a-region, in accordance with the central limit theorem, is given by the Gaussian function:

$$w(f_{\text{loc}}) = \frac{1}{\sqrt{2\pi}\Sigma} \exp\left(-\frac{(f_{\text{loc}} - f)^2}{2\Sigma^2}\right),$$

where Σ is the root mean square of the distribution of fibrosis in an a-region. The distribution of fibrosis in each of the n "small squares" has the variance $\sigma^2_{\text{sq}} \sim \sigma^2$, where σ is the parameter that we introduced to quantify the degree of heterogeneity. According to the central limit theorem Σ can be estimated as:

$$\Sigma \approx \sqrt{\frac{\sigma^2_{\text{sq}}}{n}} \sim \sqrt{\frac{\sigma^2}{n}} \sim \sqrt{\frac{\sigma^2}{(a/l)^2}} \sim \frac{\sigma l}{a}.$$

Thus, we see that the distribution $w(f_{\text{loc}})$ does not change if σl is constant. According to our assumption that the probability of arrhythmia induction depends only on the local level of fibrosis, it follows that if $\sigma l = \text{const}$, then the probability of arrhythmia induction also stays constant. Since $\sigma l = \text{const}$ is an equation for a hyperbola, this explains the hyperbolic shape of the boundary in the σ—l parameter space (Fig. 3.2b).

Chapter 4

Generation of Geometry for a Patient-Specific Model of the Human Left Ventricle based on Gadolinium Enhanced MRI

Ivan V. Kazbanov[1], Nele Vandersickel[1], Qian Tao[2], and Alexander V. Panfilov[1,3]

[1]Department of Physics and Astronomy, Ghent University, Belgium
[2]Department of Radiology, Division of Image Processing, Leiden University Medical Centre, Leiden, the Netherlands
[3]Moscow Institute of Physics and Technology (State University), Dolgoprudny, Moscow Region, Russia

Study report

4.1 Introduction

Patient-specific models of the heart serve two complementary purposes in cardiac physiology. On the one hand, they allow to pinpoint to the precise cause of a given symptom for a particular patient. A recent study [133] has demonstrated that it is possible to eliminate several potential causes for the left bundle-branch block by tuning a patient-specific model. On the other hand, detailed personalized models allow to verify if a particular phenomenon discovered in simplified models can occur in clinics. Furthermore, several potentially harmful treatments, such as an ablation procedure, can be simulated first in a model. This would allow to prognosticate the most effective way of applying a given treatment [134].

One of the most important part of any patient-specific model is geometry, that is a structure and a layout of cardiac tissue in 3D space. This also includes the distribution of degree of fibrosis which is a pathological state characterized by excess of connective tissue and population of fibroblasts. Fibrosis and especially the texture of fibrosis often play a crucial role in arrhythmogenesis [27]. Fibrosis alters the conduction velocity [135] and can be associated with heterogeneous distribution of the conduction velocity [136]. Fibrosis also affects the minimal possible activation period of a tissue [100], which can lead to arrhythmia induction, especially for heterogeneous distribution [137]. The effect of fibrosis on conduction block and the contribution of this mechanism to arrhythmogenesis was demonstrated by [138].

Recent advances of in contrast-enhanced magnetic resonance imaging (MRI) resulted in apperance of a reliable nonivasive methods for precise assessment of both cardiac geometry and layout of fibrotic tissue [139, 140]. For the moment the most widespread MRI technique for such assessment is late gadolinium enhancement (LGE) MRI, which uses a gadolinium based contrast agent [141]. Agent concentration at a certain moment after injection depends on how well a particular area is perfused and on the density of extracellular matrix. Therefore, this method provides an indirect measurement of a degree of fibrosis.

Besides being structurally heterogeneous, the heart also possesses anisotropy, that is different properties in different directions. Cardiac anisotropy is due to orientation of the myocytes which form a so-called myocardial fibers. Adjacent cells within a fiber are coupled tighter than adjacent cells in different fibers. For this reason, the wave of excitation propagates faster along the fibers than across the fibers. The exact ratio of these two propagation velocities varies depending on physiological conditions albeit often taken to be 2:1 for the ventricles. Taking cardiac anisotropy into account is important for describing both myocardial excitation [142, 143] and can be of crucial importance for arrhythmogenesis, since several mechanisms of arrhythmia induction may not be present at all in the absence of anisotropy. We will shortly review these mechanisms.

First, anisotropy effectively increases the size of the heart which affects the possibility of spiral wave emergence [116]. Second, the 3D reentry sources— scroll filaments—are stable only if the filament tension is positive [144]. In this case the dynamics of the filaments can be described by the principle of minimum energy where the energy is assumed to be the length of the filament. Anisotropy changes the metric such as the shortest path lies on geodesics which are not straight lines. These geodesics determine how a filament can be positioned [145]. Third, a sufficiently large twist in anisotropy can destabilize the rotation of the scroll wave resulting in a wave breakup. This was demonstrated in [146]. Fourth, minimal possible period of activation by a sequence of pulses depends on anisotropy both in discrete models [147] and in experimental studies. Therefore, burst pacing can result in formation of breakups as it was shown in [147]. Fifth, recent studies [148] have shown that a breakup can occur in a region with abrupt anisotropy change, in particular, when a wave leaves a region where it propagates across the fibers and enters a region where it propagates along the fibers.

In this study, we describe an approach for constructing geometry for a patient-specific model from LGE MRI data and for generating anisotropy for this geometry by a rule-based approach.

4.2 Methods

4.2.1 Acquisition and Segmentation of LGE MRI data

The process of data acquisition is described in details in [149] and [150]. A representative MRI slice is shown in Fig. 4.1a. The spatial resolution of the system was $1\,\text{mm} \times 1\,\text{mm} \times 5\,\text{mm}$. The epicardial and endocardial contours were segmented semi-automatically and independently in each of the short-axis (z) slices (Fig. 4.1b). The resulting 3D image of signal intensity was interpolated into a grid with the resolution of $h_x \times h_y \times h_z = 1\,\text{mm} \times 1\,\text{mm} \times 1\,\text{mm}$. The interpolated image had the size of about $140 \times 140 \times 80$ voxels, where each voxel had a tag determining whether it belongs to the myocardium. The discrete function of signal intensity defined by this image will be referred to as $S[x, y, z]$ where $x = h_x i, y = h_y j, z = h_z k$ and i, j, k are non-negative integers. This function was normalized such as the maximal value was 1 and the minimal value was 0. We also defined a discrete "cardiac field" function $H[x, y, z]$ as:

$$H[x, y, z] = \begin{cases} 1, & \text{if } (x, y, z) \text{ is a myocardial point} \\ 0, & \text{otherwise.} \end{cases}$$

Fig. 4.1c shows the 3D reconstruction of the human left ventricle, that is the function $H[x, y, z]$.
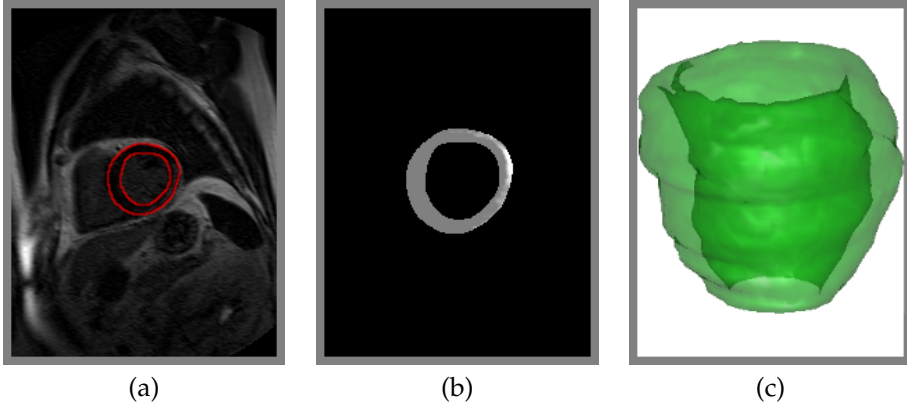
(a)   (b)   (c)

Figure 4.1. A: Representative slice of LGE MRI data. The left ventricle is shown with red. B: Segmented left ventricle. C: Reconstruction of the left ventricle in 3D.

4.2.2   Apex Recovery

Overview

As one can see in Fig. 4.1c, the original data lacks the apex area, thus resembling more a cylinder than an ellipsoid. The absence of apex can potentially lead to a presence of non-physiological activation waves, such as a plane wave circulating around the ventricle. To restore the correct topology we generated the apex taking the following assumptions:

1. The apex has a shape of paraboloid

2. All the slices of the apex in the z axis are homothetic (similar)

3. The thickness of the myocardial wall at the apex $\rho = 3$ mm.

We will describe the methodology that we used in three steps. For the first two steps we consider a continuous case. First, we will derive the paraboloid approximation of the apex. Second, we will obtain scaling coefficients for the slides of the apex. As for the last step, we will consider the discrete case and will show how we performed the scaling.

Paraboloid approximation

Our first assumption, that the apex has a shape of paraboloid, follows from the observation of Streeter [132] who described the approximation of the outer surface of the left ventricle as a prolate ellipsoid of revolution with the semimajor dimension Z_b of 5.9–7.0 cm and the semiminor dimension R_b of 3.3–3.0 cm. If we set a cylindrical coordinate system with the axis of revolution matching the z

axis and the center of the ellipsoid positioned at z', then the epicardial surface is approximated as:

$$\left(\frac{r}{R_b}\right)^2 + \left(\frac{z - z'}{Z_b}\right)^2 = 1,$$

where $r = \sqrt{x^2 + y^2}$ is the distance from the z axis. Near the bottom point $z = Z_b - z'$ the ellipsoid effectively becomes an elliptic paraboloid:

$$z = z' - Z_b + \frac{1}{2}\frac{Z_b}{R_b^2}r^2 = \text{const} + \gamma r^2. \tag{4.1}$$

The coefficient $\gamma = Z_b/2R_b^2$ can be estimated from the data of Streeter [132] that we gave above. This estimation results in

$$\gamma = 0.23\text{–}0.39 \text{ cm}^{-1}. \tag{4.2}$$

Scaling coefficients

We assumed that the apex has a shape of a paraboloid but not necessary an elliptic paraboloid: our second assumption is that all z slices at the apex are homothetic to each other. Let us consider the top slice of the missed apex part at $z = z_0$. This slice contains a contour of the epicardial surface and a contour of the endocardial surface. Suppose, we parameterize these two contours by the azimuth ϕ. For these contours we then have: $\rho = R_{\text{epi}}(\phi)$ and $\rho = R_{\text{endo}}(\phi)$. For any other z slice of the apex, our assumption of homothety combined with the assumption of the paraboloid-like shape yields:

$$1 + \frac{z - z_0}{A} = \frac{r^2}{R_{\text{epi}}^2(\phi)} \qquad (z \le z_0), \tag{4.3}$$

for the epicardial contours and

$$1 + \frac{z - z_0}{A - \rho} = \frac{r^2}{R_{\text{endo}}^2(\phi)} \qquad (z \le z_0). \tag{4.4}$$

for the endocardial contours, where A is the height of the missed apex part.

If $r = R_{\text{epi}}(\phi)$ is not much different from a circle $r = \sqrt{\bar{R}_{\text{epi}}^2 + \delta r^2(\phi)}$, then we can match the equation (4.3) to the equation (4.1), to estimate the value of γ:

$$\gamma = \frac{A}{\bar{R}_{\text{epi}}^2} \tag{4.5}$$

where $\bar{R}_{\text{epi}}$ is an average of R_{epi}. We approximated $\bar{R}_{\text{epi}}$ by the half of the maximal distance between any two points at $r = R_{\text{epi}}(\phi)$. We chose A to be 10 mm, which corresponds to $\gamma = 0.26 \text{ cm}^{-1}$. This value lies within the range given by

the estimation (4.2).

We defined the scaling factor (homothetic ratio) as $\mu(z) = r/R$. This factor gives the ratio of the length of the contour in the z_0 plane to the length of the contour in any z plane ($z \leq z_0$):

$$\mu_{\text{epi}} = \sqrt{1 + \frac{z - z_0}{A}}, \tag{4.6}$$

$$\mu_{\text{endo}} = \sqrt{1 + \frac{z - z_0}{A - \rho}}. \tag{4.7}$$

Discrete case

To use the formulas (4.6) and (4.7) directly, one needs to define the position of the center and approximate the contours in the z_0 slice as continuous functions parametrized by ϕ. We, however, used a different approach that does not require these procedures. We defined the "shrink distance" for each z slice as:

$$\Delta r = \bar{R} - r = \bar{R}(1 - \mu(z)),$$

where $\bar{R}$ is either $\bar{R}_{\text{epi}}$ or $\bar{R}_{\text{endo}}$, and μ is either μ_{epi} or μ_{endo}.

The meaning of the shrink distance is how much the contour at z slice is (linearly) smaller than the counter at z_0 slice. Next, we defined an erosion operator $\hat{e}$ that performs 1 grid point of shrinking:

$$(\hat{e}F)[x, y] = \begin{cases} 0, & \text{if any of } F[x + h_x, y], F[x - h_x, y], F[x, y - h_y], \\ & \quad \text{or } F[x, y + h_y] \text{ is zero} \\ 1, & \text{otherwise.} \end{cases}$$

Finally, we defined the function $E[x, y]$ that corresponds to the "exterior" at $z = z_0$:

$$E[x, y] = \begin{cases} 1, & \text{if the point } [x, y, z_0] \text{ belongs to or lies inside of} \\ & \quad \text{the epicardial contour in the } z_0 \text{ cross-section} \\ 0, & \text{otherwise,} \end{cases} \tag{4.8}$$

and the function $I[x, y]$ that corresponds to the "interior" at $z = z_0$:

$$I[x, y] = E[x, y] - H[x, y, z_0]. \tag{4.9}$$

For each z slice below z_0 we applied the erosion operator to E and I for the number of times $n(z)$ and $m(z)$ respectively. These numbers were determined by the shrink distance Δr:

$$n(z) = \left\lceil \frac{\bar{R}_{\text{epi}}}{h_z} \left(1 - \sqrt{1 + \frac{z - z_0}{A}} \right) \right\rceil \tag{4.10}$$

$$m(z) = \left\lceil \frac{\bar{R}_{\text{endo}}}{h_z} \left(1 - \sqrt{1 + \frac{z - z_0}{A - \rho}} \right) \right\rceil, \tag{4.11}$$

where $\lceil \cdot \rceil$ denotes the ceiling function: the smallest integer not less than the argument. The function H below the z_0 was defined as:

$$H[x, y, z] = \left(\hat{e}^{n(z)} E \right) [x, y] - \left(\hat{e}^{m(z)} I \right) [x, y] \tag{4.12}$$

where $(\cdot)^k$ denotes application of the operator for k times. The MRI signal intensity function was assumed to be zero below the z_0 plane:

$$S[x, y, z] = 0 \ \text{ when } z < z_0.$$

A brief summary of the algorithm is given in Fig. 4.2.

4.2.3 Anisotropy Generation

Overview

Our approach for generating anisotropy was based on the following two assumptions which are similar to [77] and originally derived from [132]:

1. The helix angle α_1 depends linearly on the relative distance d from the endocardium, with the value of $50°$ at endocardium and the value of $-70°$ at epicardium

2. The fiber lies in the plane orthogonal to the local epicardial surface and forms the angle α_1 with the line of latitude

We defined the relative distance from the endocardium as:

$$d = \frac{u_{\text{endo}}}{u_{\text{epi}} + u_{\text{endo}}} \tag{4.13}$$

where u_{epi} and u_{endo} are the absolute distances from the epicardial and the endocardium respectively. The normal vector to a local epicardial surface λ_1 was defined as:

$$\boldsymbol{\lambda}_1 \sim \nabla u_{\text{endo}} + \left(\nabla u_{\text{epi}} - \nabla u_{\text{endo}} \right) d.$$

This definition ensures that $\boldsymbol{\lambda}_1$ is normal to the epicardial surface at epicardium and to the endocardial surface at endocardium.

Input: $H[x, y, z]$: 3D array of binaries, discrete "cardiac field"

Output: $H[x, y, z]$: 3D array of binaries, modified to include the apex area

1. Find z_0: the minimal z when there still exist x and y such that $H[x, y, z_0] \neq 0$

2. Find all points (x, y) in the slice z_0 that have at least one neighbor (x', y') such that $H[x', y'z_0] = 0$

3. Split the obtained set into two subsets that correspond to epicardium and endocardium

4. Find $\bar{R}_{\text{epi}}$ and $\bar{R}_{\text{endo}}$: half of the distance between two farthest distant points on the epicardial and the endocardial contours

5. Define two 2D arrays $E[x, y]$ and $I[x, y]$ according to the formulas (4.8) and (4.9)

6. Set z to z_0

7. While there exists at least one point (x, y) such that $E[x, y] \neq 0$, do

    (a) Find n and m according to the formulas (4.10) and (4.11)

    (b) Set z to $z - 1$

    (c) Find n' and m' for the new value of z

    (d) Determine $\Delta n = n' - n$ and $\Delta m = m' - m$

    (e) Apply the erosion operator for Δn times to $E[x, y]$ and set $E[x, y]$ to the result of this procedure

    (f) Apply the erosion operator for Δm times to $I[x, y]$ and set $I[x, y]$ to the result of this procedure

    (g) For all x and y, set $H[x, y, z]$ to $E[x, y] - I[x, y]$

    End of the while loop

Figure 4.2. Algorithm for recovery of the apex

Boundary surfaces

The first step of the method was to find the boundary surfaces of the heart. Knowing where the boundary is located we can find the distance from the boundary to any particular point of the heart. We defined the boundary in the level-set formulation introduced in [151]. Following this formulation we should have introduced a level-set function $\psi(\boldsymbol{r})$ where the boundary was embedded as the zero-set $\{\boldsymbol{r} : \psi(\boldsymbol{r} = 0\}$. We, however, worked with a "continuous cardiac field function" $\mathcal{H}(\boldsymbol{r})$ defined such as $\mathcal{H}(\boldsymbol{r}) > 1/2$ if the point $\boldsymbol{r}$ belongs to the heart and $\mathcal{H}(\boldsymbol{r}) < 1/2$ otherwise. Therefore, the set $\{\boldsymbol{r} : \mathcal{H}(\boldsymbol{r}) = 1/2\}$ defines the boundary surface.

It is possible the continuous cardiac field $\mathcal{H}(\boldsymbol{r})$ by linear interpolation of $H[x, y, z]$. However, in this case the surface defined by the set $\{\mathcal{H}(\boldsymbol{r}) = 1/2\}$ would not be smooth, in the sense that the first derivatives would not be continuous. Instead, we chose a different approach which we implemented in two phases. First, we smoothed the initial function $H[x, y, z]$ by applying several convolutions with the Gaussian kernel. Next, we applied interpolated the results the the tricubic interpolation method. The first step has the meaning of blurring the sharp initial data to get rid of the high gradients. Essentially, when we smoothed the data, we solved the following problem:

$$\int |\nabla \mathcal{H}|^2 + w \int |\mathcal{H} - H|^2 \to \min,$$

which means that we were looking for a smooth function that approximates the data. The parameter w determined the smoothness of the the solution. The Euler-Lagrange equation for the given problem is:

$$\Delta \mathcal{H} - w\,(\mathcal{H} - H) = 0.$$

The solution of this elliptic equation can be considered as the stationary solution of the following parabolic equation:

$$\frac{\partial \mathcal{H}}{\partial t} = \Delta \mathcal{H} - w\,(\mathcal{H} - H)\,.$$

The last equation can be solved by the following numerical scheme:

$$\frac{\tilde{\mathcal{H}} - \mathcal{H}}{\tau} = \Delta \mathcal{H} - w\,(\mathcal{H} - H)\,.$$

where τ is a parameter. Instead of setting the parameter w and searching for the stationary solution, we started with the initial condition $\mathcal{H} = H$ and limited ourselves with a fixed amount of iterations, assuming that $w(\mathcal{H} - H) \ll \Delta \mathcal{H}$. Namely, we set $\tau = 0.1$ and the number of iterations to be 10 with a single itera-

tion to be as:

$$\tilde{\mathcal{H}} = \mathcal{H} + \tau \Delta \mathcal{H} = (1 + \tau \Delta)\mathcal{H}. \tag{4.14}$$

The second step was applying tricubic interpolation to the results. The advantage of the tricubic interpolation over linear interpolation is that it keeps the first derivatives continuous. As the result of these procedures we had gotten a continuously differentiable cardiac field function $\mathcal{H}(\boldsymbol{r})$ where the boundary was given by the set $\{\mathcal{H}(\boldsymbol{r}) = 1/2\}$. This function can be restricted on any rectangular grid. In our case we used a grid with the step sizes of $\sigma_x = \sigma_y = \sigma_z = 0.25$ mm.

Distance

We found the distances from the epicardial and the endocardial surfaces in two phases. First, we found the distances for the points that are neighbors to the boundary surface. Second, we solved two eikonal equations to find the distances for the rest of the grid points.

As the first step, we found the cells that contain the surface. A cell was defined a set of 8 points that form a cube of the size of $\sigma_x \times \sigma_y \times \sigma_z$. The criterion for the cell to contain the boundary surface was that there existed a cell point such as $\mathcal{H}$ was smaller than $1/2$ for this cell point *and* there existed a cell point such as $\mathcal{H}$ was larger than $1/2$. All points that belong to these cells were defined to be the boundary points. We split this set of the boundary points into two subsets: epicardial and endocardial boundary points, depending on whether they lay inside or outside the cardiac field. For each boundary point $\boldsymbol{r}_0$, we determined its distance β from the boundary surface by solving the following system of equations:

$$\begin{cases} \boldsymbol{n} = \nabla \mathcal{H}(\boldsymbol{r})/|\nabla \mathcal{H}(\boldsymbol{r})| \\ \boldsymbol{r} = \boldsymbol{r}_0 - \beta \boldsymbol{n} \\ \mathcal{H}(\boldsymbol{r}) = 1/2. \end{cases} \tag{4.15}$$

We solved this system by the Newton's method. The initial direction $\boldsymbol{n}$ was taken to be $\nabla \mathcal{H}(\boldsymbol{r}_0)/|\nabla \mathcal{H}(\boldsymbol{r}_0)|$. Using this value, we solved the second and the third equations to find β and $\boldsymbol{r}$. This point $\boldsymbol{r}$ was used to compute the new direction $\boldsymbol{n}$. After that the process was repeated unless it had converged. The resulting distance β could be positive or negative depending on whether the point $\boldsymbol{r}_0$ belonged to the heart ($H(\boldsymbol{r}_0) > 1/2$) or not respectively. As the result of this first step we were able to define a function $\beta(\boldsymbol{r}_0)$ that mapped a boundary point $\boldsymbol{r}_0$ to its distance to the closest boundary.

As the second step we determined the distances for the rest of the points. There are two values to find: the distance from the endocardium and the distance from the epicardium. The method that we have just described could have been used, in principle, for finding these distances but it is not robust if a point is relatively far away from the boundary. Furthermore, this method is computationally expensive. Instead, we used the fast marching eikonal solver described

by Sethian [152]. We solved the eikonal equation two times for different boundary conditions. For the distance from the epicardium u_{epi} we used the value of distance of the epicardial boundary points, and for the distance from endocardium u_{endo}—the endocardial boundary points. That is we solved:

$$|\nabla u_{endo}| = 1 \text{ with } u_{endo}(\boldsymbol{r}) = \beta(\boldsymbol{r}) \text{ when } \boldsymbol{r} \text{ is an endocardial boundary point,}$$
$$|\nabla u_{epi}| = 1 \text{ with } u_{epi}(\boldsymbol{r}) = \beta(\boldsymbol{r}) \text{ when } \boldsymbol{r} \text{ is an epicardial boundary point.}$$

As the result of this step we had gotten the relative distance d:

$$d = \frac{u_{endo}}{u_{epi} + u_{endo}} \tag{4.16}$$

and the normal to the local boundary surface:

$$\boldsymbol{\lambda}_1 = \frac{\nabla u_{endo} + \left(\nabla u_{epi} - \nabla u_{endo}\right) d}{\left|\nabla u_{endo} + \left(\nabla u_{epi} - \nabla u_{endo}\right) d\right|}. \tag{4.17}$$

Local coordinate system

To assign the fiber orientation for a point $\boldsymbol{r}$ we introduced a local coordinate system. The first coordinate direction was given by the normal to the local boundary surface $\boldsymbol{\lambda}_1$. The other two directions were the line of latitude (parallel) $\boldsymbol{\lambda}_2$ and the line of longitude (meridian) $\boldsymbol{\lambda}_3$. We determined $\boldsymbol{\lambda}_2$ by finding the direction outwards the apex $\boldsymbol{t}$. To find $\boldsymbol{t}$, we solved the eikonal equation:

$$|\nabla u_b| = 1 \text{ with } u_b(\boldsymbol{r}_b) = 0 \text{ where } \boldsymbol{r}_b \text{ is the lowest point of the heart.}$$

We set $\boldsymbol{t} = \nabla u_b$. After that, $\boldsymbol{\lambda}_2$ was determined to be orthogonal to $\boldsymbol{\lambda}_1$:

$$\boldsymbol{\lambda}_2 = \frac{\boldsymbol{t} - (\boldsymbol{t} \cdot \boldsymbol{\lambda}_1) \boldsymbol{\lambda}_1}{\sqrt{1 - (\boldsymbol{t} \cdot \boldsymbol{\lambda}_1)^2}}, \tag{4.18}$$

where $(\cdot)$ denotes the dot product.

Finally, $\boldsymbol{\lambda}_3$ was determined as the vector product of $\boldsymbol{\lambda}_1$ and $\boldsymbol{\lambda}_2$:

$$\boldsymbol{\lambda}_3 = \boldsymbol{\lambda}_1 \times \boldsymbol{\lambda}_2, \tag{4.19}$$

where $(\times)$ denotes the vector product. The fiber direction $\boldsymbol{f}$ was determined by

$$\boldsymbol{f} = \boldsymbol{\lambda}_2 \sin \alpha_1 + \boldsymbol{\lambda}_3 \cos \alpha_1, \tag{4.20}$$

where α_1 is the helix angle:

$$\alpha_1 = 50° - 120°d.$$

4.2.4 Fibrosis Representation

For this study we limited ourselves with the model of geometry. Thus, we considered only the structural component of fibrosis, which is an increase in the density of fibroblasts and connective tissue. The effect of fibrosis on geometry was implemented by introducing of small inexcitable obstacles of the size of $\sigma = 0.25$ mm. The initial function of the signal intensity $S[x, y, z]$ was linearly interpolated to the grid with the resolution of $\sigma = 0.25$ mm. After that the cardiac field function $H'[x, y, z]$ was defined as:

$$H'[x, y, z] = \begin{cases} 1, & \text{if } H[x, y, z] = 1 \text{ with the probability } (1 - S[x, y, z]) \\ 0, & \text{if } H[x, y, z] = 1 \text{ with the probability } S[x, y, z] \\ 0, & \text{if } H[x, y, z] = 0 \end{cases}$$

4.3 Results

The reconstruction of the left ventricle with the recovered apex is shown in Fig. 4.4a. For this picture, the scar points were defined as the points (x, y, z) where the normalized signal intensity $S[x, y, z]$ is larger than $1/2$. These scar points are shown with purple. In Fig. 4.4b, one can see how geometry of the left ventricle looks after imposing our algorithm for fibrosis representation.

The result of our fiber generation approach is shown in Fig. 4.6. The helix angle α_1 is shown with color. For two regions highlighted with rectangular boxes, there are zoomed subfigures showing the fiber orientation in the y cross-section.

We also performed a test run with this model to demonstate that a spiral wave can be induced by burst pacing. We used the TNNP model with the Na current reduced by 3 times. We paced with the period of 250 ms from the apex area of the left ventricle. On 15 stimulations, we observed initiation of a persistent spiral wave which stood in the ventricle after the arrest of pacing. An example of a spiral wave obtained with this model is shown in Fig. 4.5.

4.4 Discussion

In this study we developed a rule based method for generation of geometry and fiber orientation for patient-specific models from the LGE MRI data. Our approach is based on several *a priopi* assumptions that were mostly derived from the work of Streeter [132].

Anatomical models described in [153] and [77] also use the same definition of the relative distance (4.16) to determine the helix angle. However, the numerical algorithm for finding the distances that is used in those studies is based on [154]. The difference from the algorithm that we use is minor, since both algorithms

Input: $H[x, y, z]$: 3D array of binaries, discrete "cardiac field"

Output: $\mathcal{H}[x, y, z]$: 3D array of floating-point numbers, continuous "cardiac field", and $F[x, y, z]$: 3D array of 3-vectors, fiber orientation

1. Set $H[x, y, z]$ to its convolution with a Gaussian kernel (formula (4.14)), repeat 10 times

2. Define function $\mathcal{H}(\boldsymbol{r})$ by tricubic interpolation of $H[x, y, z]$

3. Define 3D array $\mathcal{H}[x, y, z]$ by restricting $\mathcal{H}(\boldsymbol{r}$ on a rectangular grid with the step sizes of $\sigma_x, \sigma_y, \sigma_z$

4. Find all boundary points

5. Find each boundary point $\boldsymbol{r_0}$ determine its distance to the boundary surface by solving the equations (4.15) by the Newton's method

6. Split the set of boundary points into the subset of endocardial and the subset of epicardial boundary points

7. Solve the eikonal equation for using the epicardial points with their distances from the boundary as the initial condition. Set u_{epi} to the result.

8. Solve the eikonal equation for using the endocardial points with their distances from the boundary as the initial condition. Set u_{endo} to the result.

9. Solve the eikonal equation for using the bottom boundary point with the distance from the boundary of 0 as the initial condition. Set u_b to the result.

10. For each point (x, y, z) such that $\mathcal{H}[x, y, z] > 1/2$, do

    (a) Determine d and $\boldsymbol{\lambda}_1$ according to the formulas (4.16) and (4.17)

    (b) Determine $\boldsymbol{t} = \nabla u_b$ and $\boldsymbol{\lambda}_2$ according to the formula (4.18)

    (c) Determine $\boldsymbol{\lambda}_3$ according to the formula (4.19)

    (d) Determine $\boldsymbol{f}$ by the formula (4.20) and set $F[x, y, z]$ to $\boldsymbol{f}$

    End of the for loop

Figure 4.3. Algorithm for generation of fiber orientation
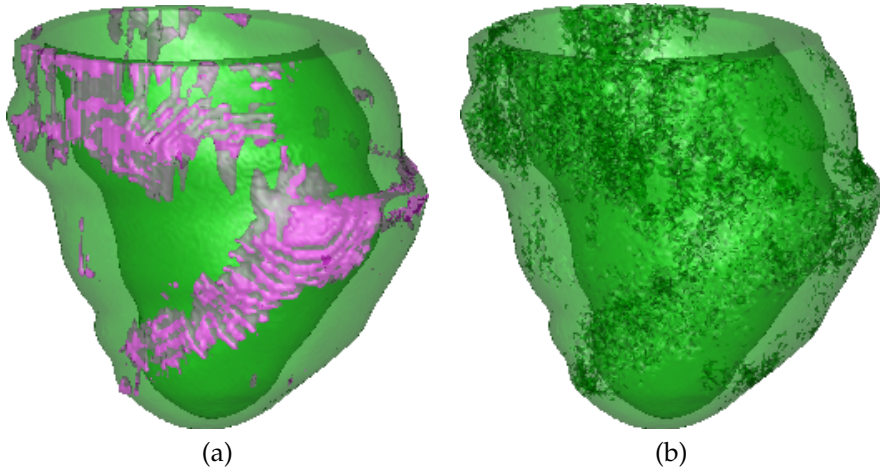
(a) (b)

Figure 4.4. Reconstruction of the left ventricle with recovered apex area. A: The scar area is shown with purple. B: Effective geometry obtained after imposing our approach for fibrosis generation.
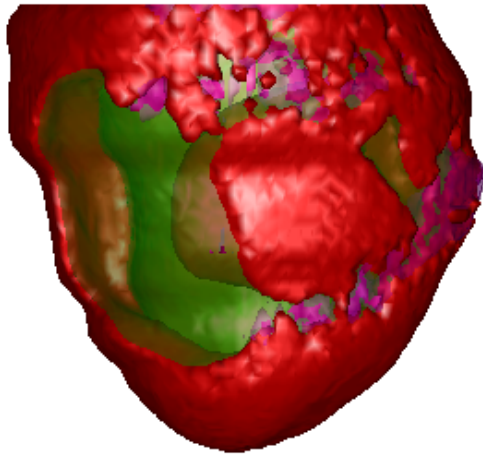

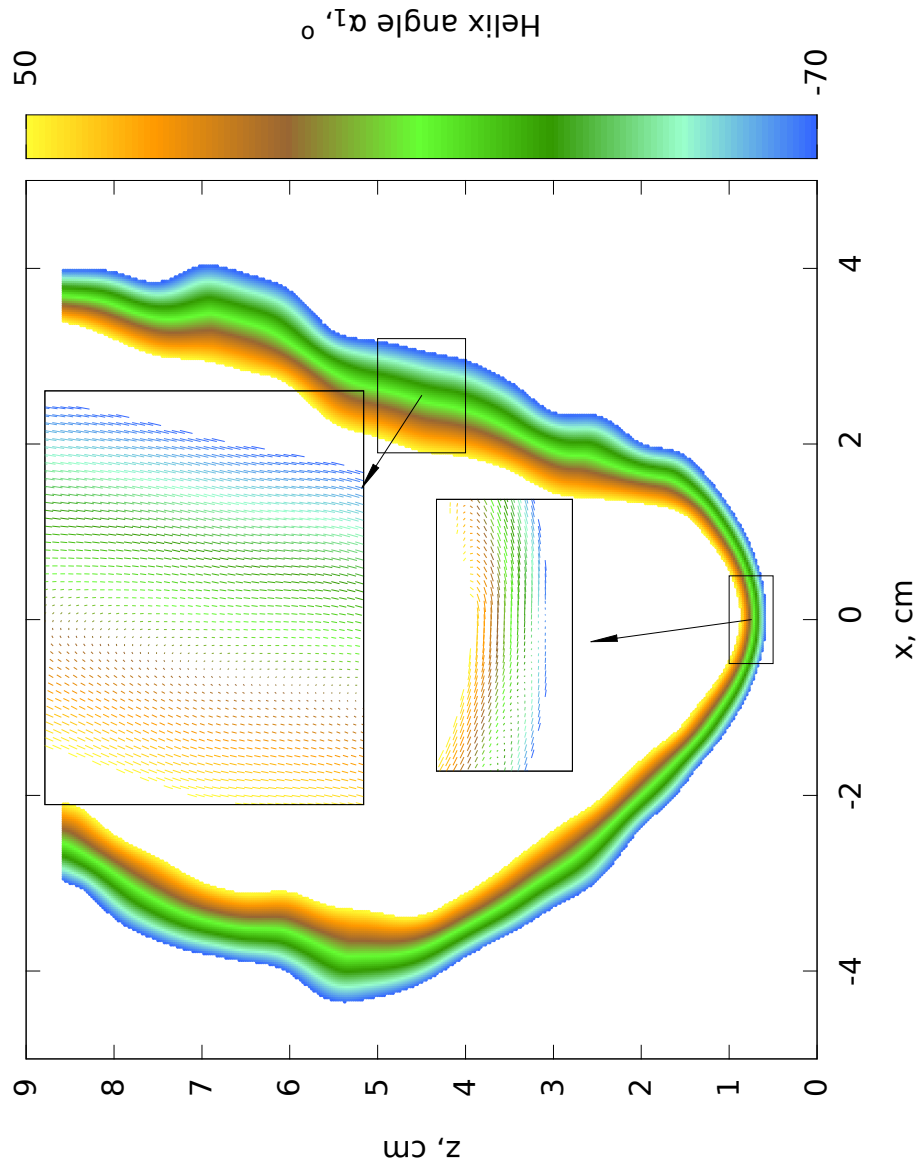**Figure 4.5.** A spiral wave initiated by the burst pacing protocol in the patient-specific model.

Figure 4.6. Helix angle distribution and fiber orientation for a y cross-section.

belong to the class of Dijkstra-like methods for the eikonal equation [155, 156]. The advantage of the Sethian's approach is that it is not required to forfeit the rectangular grid to get a sub-grid resolution. An alternative approach for determining the local distance is described, for example, in [157]. This approach is based on solving Laplace's equations with mixed boundary conditions. A solution of Laplace's equation can be considered as the relative distance provided the size of myocardial wall is much smaller than the distance from the wall to the center of the ventricle. This assumption holds for a human left ventricle.

Another approach to define the fiber orientation is, first, to define a reference geometry with known anisotropy for a heart from histology or diffusion tensor MRI measurements, and, then, define a smooth transformation of the reference geometry to the patient-specific geometry. This approach is demonstrated, for instance, in [134] and [60].

Our approach to determining the location of epicardial and endocardial boundary is very simplistic. More powerful methods acting on the same principle of energy minimization are available [158]. Instead of minimizing the square of gradient, one can minimize the surface area which leads to more realistic results. This method is know as the method of active contours and it was used in [153]. In fact, extracting the surface from the data is part of segmentation process. In our case the segmentation is done in the short-axis plane, and in Fig. 4.1c one can see a shift in between some 2D slices. Therefore, our approach could be greatly improved by adapting the active contours method for the process of segmentation to obtain a truly smooth 3D image.

There are several methods to model the effects of fibrosis [106–108]. Here, we limited ourselves with the effects of fibrosis on geometry. The geometry can be coupled to any electrophysiological model, with according modifications to fibrotic regions. For our test run we used the TNNP model [41] and assumed that fibrosis results in decrease of the Na current. For this setup, we demonstrated that persistent arrhythmia sources can be induced by burst pacing.

Chapter 5

Attraction of Arrhythmia Sources by Fibrotic Regions via Dynamical Restructuring of Activation Pattern

IVAN V. KAZBANOV[1], NELE VANDERSICKEL[1], MASAYA WATANABE[2], QIAN TAO[3], JAN FOSTIER[4], KATJA ZEPPENFELD[2] AND ALEXANDER V. PANFILOV[1,5]

[1]Department of Physics and Astronomy, Ghent University, Belgium
[2]Department of Cardiology, Leiden University Medical Center, Leiden, the Netherlands
[3]Department of Radiology, Division of Image Processing, Leiden University Medical Centre, Leiden, the Netherlands
[4]Department of Information Technology (INTEC), Ghent University — iMinds, Ghent, Belgium
[5]Moscow Institute of Physics and Technology (State University), Dolgoprudny, Moscow Region, Russia

5.1   Introduction

Radio frequency catheter ablation (RFCA) has been proved as an effective therapeutic approach to refractory ventricular tachycardia (VT) [159–161]. Recent advances in the therapeutic techniques and 3 dimensional mapping system made it possible to target those VTs not inducible during procedure and hemodynamically unstable VTs by unmasking possible substrate for VT circuit [162, 163].

However, clinical implication and the mechanism of fast VT, most of which are inducible solely by burst pacing stimulation, remains unclear [164–166]. Of importance, most of them possess monomorphic or minimally changing morphology, suggesting that it may have different substrate and mechanism from polymorphic VT and ventricular fibrillation.

It was demonstrated that if RFCA results in complete procedural success, defined as noninducibility of any VT after the last RF application, then the recurrence rate of VT inducibility is lower in comparison with the case of partial success when only clinical VTs are noninducible [165]. Therefore, understanding the mechanism of fast nonclinical VT is of importance for improving the long-term outcome of RFCA.

A clue to understanding fast nonclinical VT may lie in determining the location of arrhythmia sources. Several experimental and numerical studies suggest that fibrotic regions can anchor the arrhythmia sources in the atria in case of atrial fibrillation [108, 112, 117]. The fibrotic area is often associated with a scar border zone (or a gray zone); and anchoring of the arrhythmia sources to the border zone has also been demonstrated in clinics [167]. The exact mechanism for this anchoring remains unclear.

The aims of this study are to investigate the mechanism of anchoring of fast arrhythmia sources to fibrotic areas and demonstrate that such anchoring is possible in a post myocardial infarction left ventricle. To archive this goal we use general and patient-specific mathematical models.

5.2   Methods

5.2.1   Magnetic Resonance Imaging

The method for late gadolinium enhanced (LGE) magnetic resonance imaging (MRI) was described in details in [150]. Briefly, a 1.5-T Gyroscan ACS-NT/Intera MR system (Philips Medical Systems, Best, the Netherlands) system was used with standardized protocol. The contrast—gadolinium—was injected in 15 min before the image acquisition. Imaging was done with 24 levels in short-axis view after 600—700 ms of the R-wave on the ECG. This gave the resolution of 1 mm in long-axis and 5 mm in short-axis. The segmentation of the contours for the endocardium and the epicardium was performed semi-automatically on

the short-axis views using MASS software (Leiden University Medical Centre, Leiden, the Netherlands).

5.2.2 Electrophysiology Model

The 2D model was described in details in [137]. Briefly, for ventricular cardiomyocyte we used the ten Tusscher and Panfilov model[41], and the cardiac tissue was modeled as a rectangular grid of 1024×512 nodes nodes. The model is given by:

$$C_m \frac{\mathrm{d}V_{ik}}{\mathrm{d}t} = \sum_{\alpha,\beta \in \{-1,+1\}} \eta_{ik}^{\alpha\beta} g_{\text{gap}} \left(V_{i+\alpha,k+\beta} - V_{ik}\right) - I_{\text{ion}}(V_{ik}, \dots), \qquad (5.1)$$

where V_m is the transmembrane voltage at the (i,j) computational node, C_m is membrane capacitance, g_{gap} is the conductance of the gap junctions connecting two neighboring myocytes, I_{ion} is the sum of all ionic currents and $\eta_{ik}^{\alpha\beta}$ is the connectivity tensor whose elements are either one or zero depending on if neighboring cells are coupled or not. A similar system of differential equations was used for the 3D computations where instead of the 2D connectivity tensor $\eta_{ik}^{\alpha\beta}$ the 3D weights tensor $w_{ijk}^{\alpha\beta\gamma}$ was used whose elements are ranged in between zero and one, depending both on coupling of the neighbor cells and anisotropy due to fiber orientation.

5.2.3 Fibrosis Model

Fibrosis was modeled by introduction of small inexcitable obstacles that were electrically uncoupled from the myocytes. The local level of fibrosis determined the probability for a node of the computational grid to become an inexcitable obstacle. In addition, the effect of ionic remodeling was taken into account for several results of the paper. To describe ionic remodeling we decreased the conductance of conductance of I_{Na}, I_{Kr}, and I_{Ks} depending on local fibrosis level as:

$$G_{\text{Na}} = \left(1 - 1.55\frac{f}{100\%}\right) G_{\text{Na}}^0, \qquad (5.2)$$

$$G_{\text{Kr}} = \left(1 - 1.75\frac{f}{100\%}\right) G_{\text{Kr}}^0, \qquad (5.3)$$

$$G_{\text{Ks}} = \left(1 - 2\frac{f}{100\%}\right) G_{\text{Ks}}^0, \qquad (5.4)$$

where G_X is the peak conductance of I_X ionic current, G_X^0 is the peak conductance of the current in the absence of remodeling, and f if the local fibrosis level in percent. These formulas yield the reduction in 62% in 70% in and 80% in if the

local fibrosis f is 40%. Such value of the local fibrosis corresponds to the percolation threshold for our 2D model, therefore such values of conductance reduction correspond to the region near nonconducting scar, or the border zone.

5.2.4 Model of the Human Left Ventricle

The geometry and the layout of fibrotic tissue in the human left ventricles were determined using the LGE MRI data. The normalized signal intensity were assumed to determine the local fibrosis level.

The anisotropy due to fiber orientation was defined using a rule-based approach based on [132]. The fiber helix angle α_1 was taken to be $-70°$ at the epicardium and $+50°$ at the endocardium with linear dependency on the relative distance from the endocardium in between:

$$\alpha_1 = 50° - 120°d.$$

The relative distance for the endocardium was defined as:

$$d = \frac{u_{\text{endo}}}{u_{\text{epi}} + u_{\text{endo}}},$$

where u_{epi} and u_{endo} are the distances from the epicardium and endocardium respectively. These distances were determined by solving the eikonal equation with the corresponding boundary conditions. In addition we also determined the distance from the bottom point in the apex u_{apex} by solving the corresponding eikonal equation.

The normal to a local cardial surface λ_1 was determined by normalization of the following vector:

$$\lambda_1 \sim \nabla u_{\text{endo}} + \left(\nabla u_{\text{epi}} - \nabla u_{\text{endo}}\right) d.$$

The line of meridian λ_2 in each local cardial surface was found by orthogonalization of ∇u_{apex} with respect to λ_1:

$$\lambda_2 = \frac{\nabla u_{\text{apex}} - \left(\nabla u_{\text{apex}} \cdot \lambda_1\right) \lambda_1}{\sqrt{1 - \left(\nabla u_{\text{apex}} \cdot \lambda_1\right)^2}},$$

where the dot denotes the inner product. The line of latitude λ_3 was determined by:

$$\lambda_3 = \lambda_1 \times \lambda_2,$$

where the multiplication sign denotes the vector product.

The fiber $\mathbf{r}$ was assumed to lie in the plane orthogonal to λ_1 and to form the
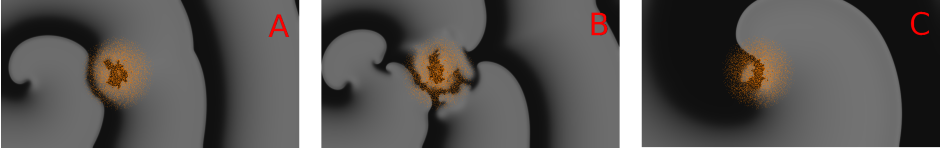
Figure 5.1. Attraction of a spiral wave to a fibrotic region in the 2D model. Inexcitable fibrotic tissue is shown with orange and the transmembrane voltage is shown in shades of gray. A: A spiral wave initiated 4.3 cm away from the border of the fibrotic region ($t = 0$ s). B: The wave front breaks on the fibrotic region and some secondary sources propagate towards the tip of the spiral wave ($t = 4.8$ s). C: One of the secondary sources merged with the tip of the spiral. This restructuring of the activation pattern resulted in emergence of a single spiral wave anchored to the scar.

angle α_1 in between the line of latitude:

$$\mathbf{r} = \lambda_2 \sin \alpha_1 + \lambda_3 \cos \alpha_1.$$

5.2.5 Numerical Methods and Implementation

The model for cardiac tissue was solved by the forward Euler integration scheme with the time step of 0.02 ms. The numerical solver was implemented using CUDA toolkit for performing the computation of graphical processing units. Computations were done with single precision on GeForce GTX Titan Black graphics cards.

The eikonal equations needed for anisotropy generation was solved using fast marching Sethian's method [152]. The eikonal solver and all of the model generation pipeline were implemented in the OCaml programming language.

5.3 Results and Discussion

5.3.1 Attraction of the Spiral Wave in the Model of Tissue

We performed several simulations where we initiated a spiral in a 2D tissue model and then imposed a fibrotic region nearby. A representative example is shown in Fig. 5.1. The initial setup is given in Fig. 5.1A where the fibrotic region had the diameter of 6.4 cm with the level of fibrosis changing linearly from 50% at the center of the scar to 0% at the scar boundary. After several seconds the activation pattern becomes less regular and a few secondary spirals appear at the fibrotic region. These secondary spirals start to propagate towards the tip of the initial spiral creating a complex activation picture in between the scar and the tip (Fig. 5.1B). Finally, when one of the secondary sources reaches the tip of the original spiral, the whole activation pattern completely restructures which results in emergence of just a single spiral rotating around the scar (Fig. 5.1C).

A more detailed investigation of the process of attraction allowed us to suggest the following mechanism. After initialization of a spiral, the waves that the spiral generates start to break up at the scar region. The wave breakups result in appearance of secondary sources. These secondary sources propagate towards the initial spiral. While the sources propagate, new secondary sources appear at the scar which also start to propagate towards the initial spiral. This leads to appearance of a fibrillatory-like pattern in between the initial spiral and the scar (Fig. 5.1B). When one of the secondary sources reaches the tip of the initial spiral, the source and the spiral annihilate. This results in deceleration of the activation pattern and promotes a sort of chain reaction of merging all the secondary sources together. This effectively leads to survival of only one secondary source located most closely to the scar. This source then becomes a primary source anchored to the scar.

The given description is only precise if the scar is relatively close to the initial spiral when all the secondary sources do not disappear at the boundary. In this case the resulting spiral has the same direction of rotation as the initial spiral, since only the sources rotating in the different directions can emerge or annihilate. However, if the scar is relatively further away, some secondary sources may be destroyed by the boundary. This changes the difference between the amount of sources rotating clockwise and counter-clockwise which can result in the following activation patterns:

- Termination of activity

- A spiral rotating either clockwise or counter-clockwise

- A two- or three-armed spiral rotating either clockwise or counter-clockwise

All these resulting activation patterns were observed in our simulations. Fig. 5.2 demonstrates the relative chance of the mentioned activation patterns to occur depending on the distance between the spiral and the border of the fibrotic region. We see, indeed, that for smaller distances the resulting activation pattern is always a single spiral. With an increase in the distance, other resulting patterns are possible. If the distance is larger than about 9 cm, there is at least 50% chance to obtain either a multi-armed spiral or termination of activity. Note that these results should depend on the size of the medium. For wider medium the amount of cases where a single spiral occurs should be higher.

Regardless the type of the resulting activation pattern, our simulations showed that the effect of dynamical restructuring is present no matter how far the spiral is away from the scar. Given enough time it was always possible to find either attraction or termination of the activation pattern. We measured the time that required for the effect to happen initializing the spiral at different distances from the scar. For each value of distance we made about 60 computations changing the seed of the random number generator. We used two models for fibrosis: with
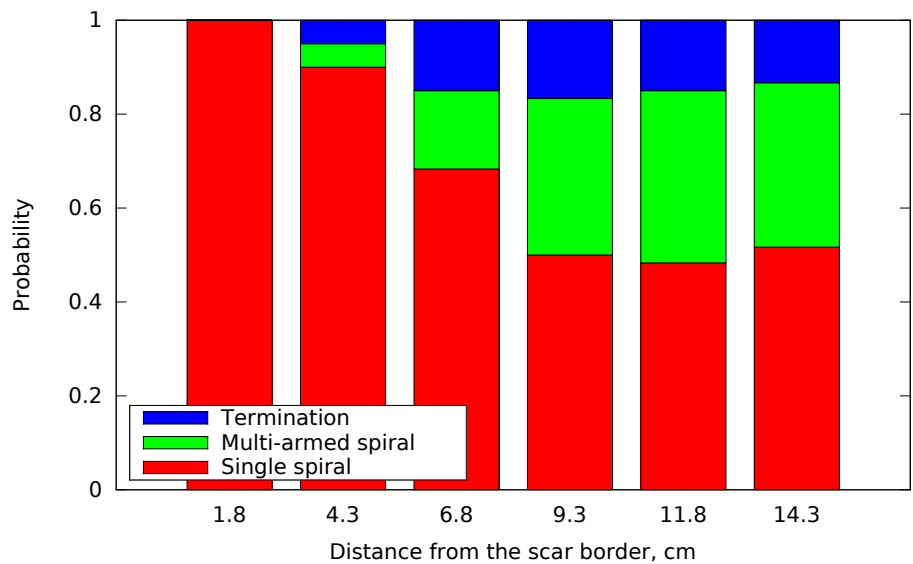
Figure 5.2. Type of the resulting activation pattern as a function of the distance between the spiral spiral and the border of the scar. Red: the resulting activation pattern is a spiral rotating either in the same direction as the original spiral or in the opposite direction. Green: the resulting activation pattern is a spiral with two or three arms. Blue: the electrical activity vanishes after dynamical restructuring of the activation pattern.
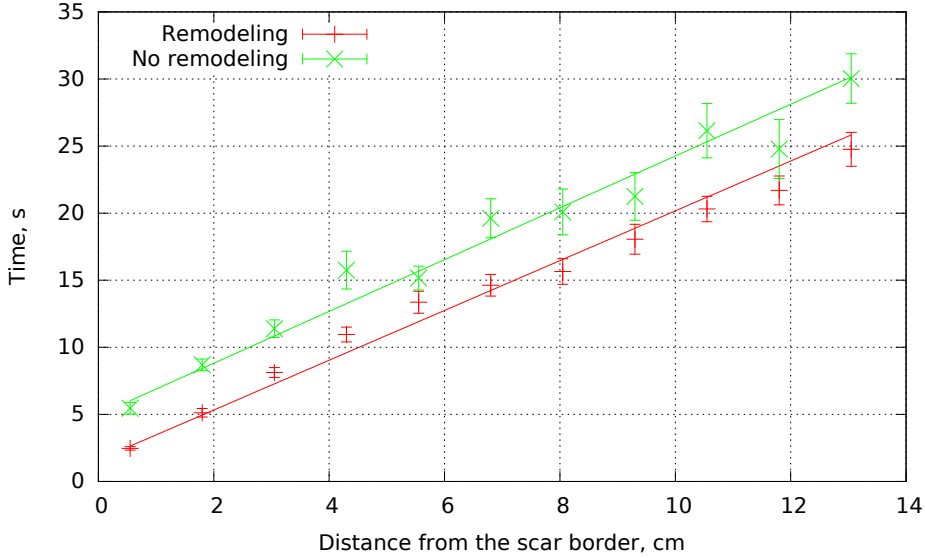
Figure 5.3. Dependency of time required for spiral attraction of termination on the initial distance between the spiral tip and the border of the fibrotic region in the 2D model. Red: the model of fibrosis take ionic remodeling into account. Greed: fibrosis is modeled only by introduction of small inexcitable obstacles. The error bars denote the standard error.

and without taking ionic remodeling into account. The results of these simulations are shown in Fig. 5.2.

In Fig. 5.3 we see that the time needed for the restructuring of the activation pattern depends linearly on the distance between the border of the scar and the initial spiral. The green line corresponds to the scar model with no ionic remodeling and the red line is for the scar with remodeling. We see that the two lines have equal slope. These results complement our description of the attraction effect in the following way. First, the propagation velocity of a secondary source is constant and does not depend on the model of the scar. This velocity is given by the inverse slope and is about of 0.5 cm/s. Second, the secondary sources are formed only after some time after the spiral initialization. This time interval is about 3.5 s longer for the model of the scar without remodeling compared with the model of the scar with remodeling. Third, as we have already mentioned, the presence of the effect has no dependency on the distance: for all simulations we performed the activation pattern restructuring had always been the case.
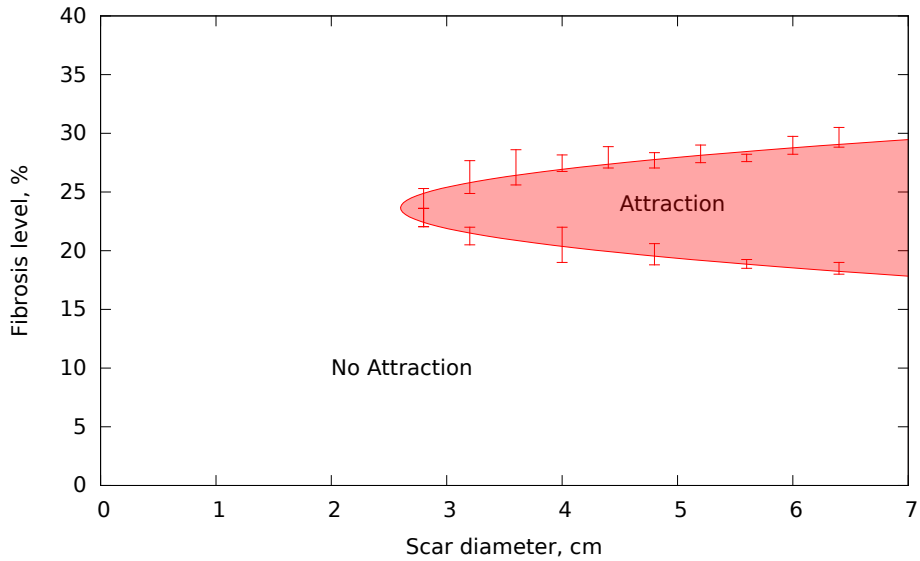
Figure 5.4. Phase diagram showing the region where the anchoring effect is present in two-parametric space: the size of the scar and the fibrosis level. The scar had a uniform fibrosis distribution. The mark "Attraction" corresponds to the region where the anchoring was obtained in more than 65% of all cases. "No Attraction" shows the region where the effect occurred in less than 65% of the cases.

5.3.2 Factors Responsible for the Attraction Effect

To study what is responsible for process of attraction, we varied the size and the fibrosis level within the scar and monitored if the attraction effect was present. Due to stochastic nature of the fibrosis layout we performed about 60 computations with different initial value of the seed for each given combination of the scar size and the fibrosis level. The results are shown as a phase diagram in Fig. 5.4.

In Fig. 5.4 one can see that attraction does not happen when the scar size is relatively small or fibrosis level is either too low or too high. For low fibrosis levels we can explain the absence of the breakup in the following way. As it shown, for example, in [100] the period of the spiral wave increases with increase in fibrosis level if fibrosis is applied uniformly. Therefore, one can expect that the minimal possible period of pacing also increases with increase in fibrosis level since for highly excitable media like cardiac tissue the period of spiral wave rotation is approximately the same as the minimal possible period. If we pace a fibrotic region with a certain period, the wave front will break only if the minimal period of pacing is higher than the pacing period, that is the front will break not for lower fibrosis levels but for higher. Therefore, at lower fibrosis levels the

breakup is not formed and the attraction does not happen.

On the other hand, attraction does not happen for high values of fibrosis as well. In this case, we observed that the block is formed inside the scar but it cannot leave the fibrotic region. In simulations, it looked as if the fibrotic region had been separated from the healthy region by a semipermeable boundary which effectively disconnected activation within the scar from the rest of the activation pattern. We think that this effect may be due to the unidirectional block that happens on the boundary in between a low and a high diffusivity. This unidirectional block prevents the waves from the region with low diffusivity (e.g. fibrotic region) go to the region with high diffusivity. If the fibrosis level is about or above of the percolation threshold (approximately 40% in our model), then the scar effectively becomes a large obstacle that is incapable of breaking the wave front.

Finally, we observed the absence of both the breakup and attraction for small sizes of the scar. We explain it by the fact that the breakup should be a certain size in order to develop. If the breakup size is small, the two secondary sources that are form from it are merged immediately repairing the wave front shape.

5.3.3   Attraction in the Model of the Left Ventricle

To verify that the attraction effect takes place in a more realistic geometry we developed and investigated a patient-specific model of the human left ventricle. This model was based on the contrast-enhanced MRI data of a patient with a scar. Cardiac anisotropy was generated by a rule-based approach which described in details in the Methods section. The size of the scar for this model was about 7 cm with fibrosis level changing gradually from low values of the boundaries to high values ($> 50\%$) at the middle of the scar. The remodeling of ionic channels at the scar region was also included to the model. We did several numerical experiments varying the initial position of the scroll wave.

A representative example of our 3D simulations is given in Fig. 5.5. We followed the same protocol as for the 2D simulations. The scroll wave is initiated 5 cm away from the scar (Fig. 5.5A), then the secondary sourced start to appear (Fig. 5.5B), and finally the spiral attaches to the scar and persistently rotates around it. To see how this effect can potentially be registered in clinics we computed the ECG for our 3D simulations. The ECG that corresponds to the example in Fig. 5.5 is given in Fig. 5.6. We see that for the first 3 seconds the ECG is relatively irregular but becomes of a more regular structure afterwards. This change in morphology in associated with attraction of the scroll wave which takes place around the third second of the simulations. The initial irregularity is due to the presence of the secondary sources that have a slightly higher period than the original scroll wave. After the scroll is anchored the pattern becomes relatively stable which corresponds to a regular ECG morphology.

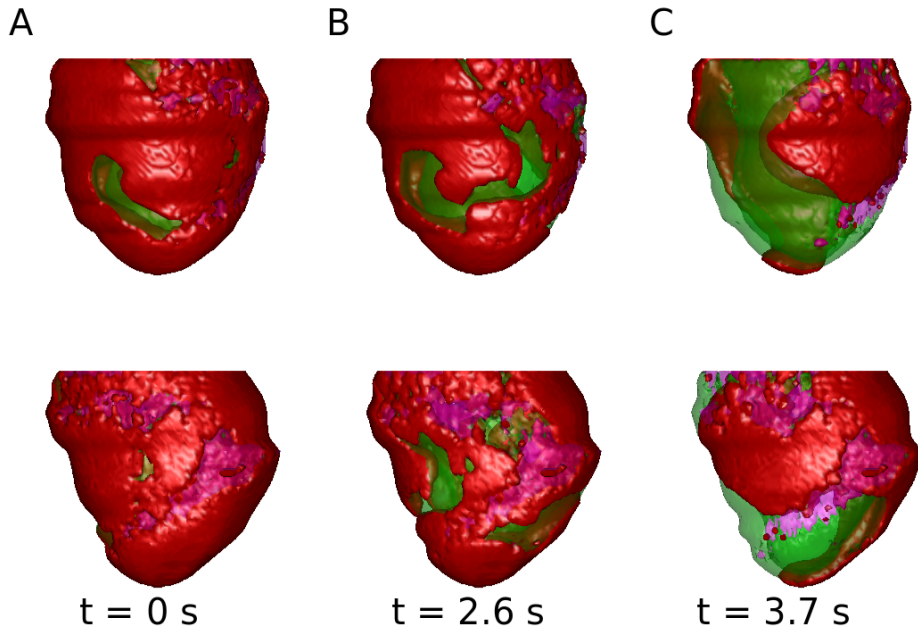The blue points in Fig. 5.6 show the value of the coupling interval—the time

Figure 5.5. Effect of spiral wave attraction for a patient-specific model of the left ventricle. Red color corresponds to high transmembrane voltage, pink color shows the scar. The top and the bottom rows correspond to different view points. A: A spiral wave initiated 5 cm away from the scar region. B: The breakups form making the activation pattern less regular (2.6 s after the initialization) C: The spiral gets anchored to scar and rotates around it persistently (3.7 s after the initialization).
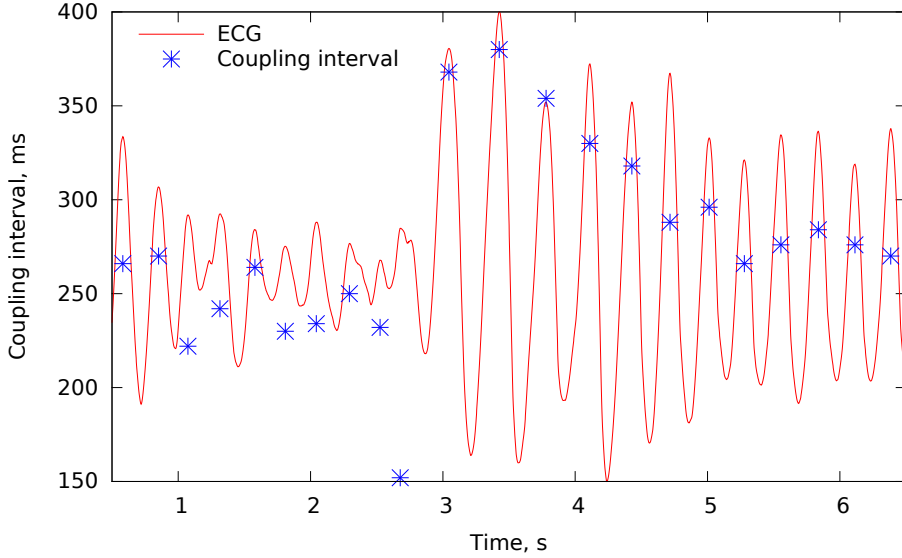
Figure 5.6. A representative example of ECG for the anchoring effect in the 3D model. Red: ECG in relative units. Blue: coupling interval for two subsequent peaks in ms. The anchoring happens approximately at the end of the third second.

difference between two subsequent peaks. We see that the attraction effect is accompanied by the increase of the coupling interval. The reason for this effect is that the spiral rotation around an obstacle—anatomical reentry—is usually slower than the rotation of the spiral around its own tip—functional reentry. These results allow us to assume that the attraction effect has the following manifestation in ECG: a sudden change from polymorphic to monomorphic ventricular tachicardia which may be accompanied by an increase in the coupling interval.

5.3.4 Transition from Mono- to Polymorphic VT in Clinical ECG

We found clinical examples when a change from monomorphic to polymorphic VT happens during induction of fast VT. The examples for two patients are given in Fig. 5.7; only V2, V3, and V4 leads are shown. Both patients underwent ventricular ablation and had scars in their hearts. The tachyarrhythmia was induced by applying the S1S2 protocol in the right ventricle. In Fig. 5.7 we see that immediately after the induction, the ECG had a polymorphic structure but became more regular afterwards. For the patient A this change was accompanied with an increase in the coupling interval but for the patient B it was not. Although it is not a explicit proof that attraction to the scar area was the case for those clinical studies, it is an indirect evidence that attraction may take place for
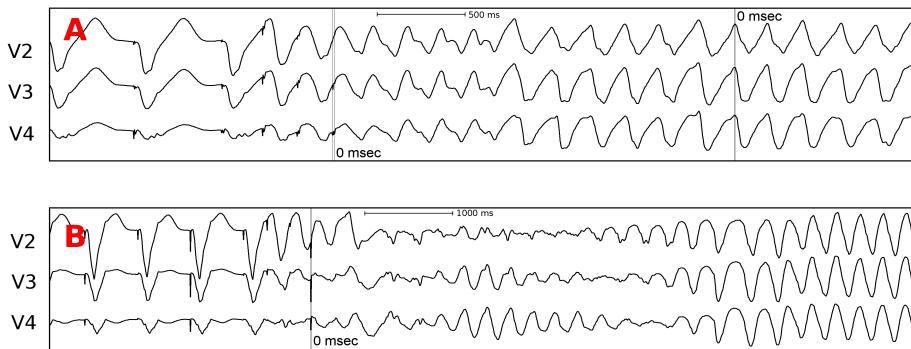
Figure 5.7. Leads V2, V3, and V4 of clinical ECGs obtained during induction of ventricular tachycardia for two patients with scars in the left ventricle. First several beats until the mark "0 msec" correspond to external pacing.

fast VT.

5.4 Concluding Remarks

In this study we investigated the dynamics of arrhythmia sources—spiral waves—in presence of fibrotic regions using mathematical modeling. We showed that anchoring of the spiral waves to fibrotic regions happens because of attraction of the arrhythmia source to the fibrotic region. Attraction process is due to dynamical restructuring of the activation pattern: formation and merging of secondary activation sources.

In [168] it was demonstrated that heterogeneity in ionic channel distribution can attract the spiral waves. In this study we demonstrate that structural heterogeneity is enough to trigger this type of attraction. Apart from [168], we show that the presence of the attraction effect does not depend on how far a spiral is away from fibrosis region. Instead we found that the presence effect depends on the level of fibrosis and on the size of fibrotic region. For either low or high level of fibrosis, attraction does not happen. This result puts emphasis on importance of the scar border zone (gray zone). The border zone is known to be a major predictor of cardiac mortality [149], and our study shows that the border zone plays the most significant role in the process of spiral waves attraction.

Finally, the presence of attraction of the arrhythmia sources to the scar was demonstrated in a anatomically accurate patient-specific model of the left ventricle. It was demonstrated that attraction manifests itself as a transition from polymorphic to monomorphic VT. This transition is sometimes associated with a spiral drift [20], and our study shows that it can also be an indicator of dynamical fibrillation-like restructuring of the activation pattern.

Chapter 6

Summarizing Discussion

The main subject of this thesis is to consider the effect of pathophysiological conditions on the onset and dynamics of cardiac arrhythmias. In chapter 2 we have studied the effects of global cardiac ischemia on perpetuation of ventricular fibrillation and stability of the activation pattern. In chapter 3 we have investigated the impact of another pathological condition: fibrosis. We have considered heterogeneous distribution of fibrosis and investigate whether it can promote arrhythmia triggering. In chapter 4 we have developed a patient-specific model of fiber orientation coupled with fibrosis layout for describing the results of clinical investigations. In chapter 5 we have studied the effects of compact fibrosis on dynamics and the positions of the arrhythmia sources.

In this chapter we shall review the results of the previous chapters and shall formulate the conclusions of the thesis.

In chapter 2 we have considered the effect of global cardiac ischemia on dynamics of fibrillation. The study was based on unique clinical data recorded during open chest surgery [53]. We developed a model for ischemia based on the other simulation studies [26, 57, 58] and *in vitro* experiments [55]. We have demonstrated that ischemia has a large impact on cardiac fibrillation. First, ischemia prevents formation of breakups due to decrease of steepness of the restitution curve. This effect implies an increase in stability of the activation pattern during ischemia, and a decrease in chance of spontaneous termination of the activity. Second, we have shown that one factor of ischemia—hyperkalemia—decreases the frequency of the activation pattern, and another factor—hypoxia—increases the frequency. We used these results to describe the time dynamics of these factors for the first few minutes of ischemia in the human heart. Third, we have shown that ischemia does not change the complexity of the activation patterns, and the number of the arrhythmia sources is mostly determined by the initial conditions.

In chapter 3 we have studied the effects of the fibrosis layout on arrhythmo-

genesis. We have shown that fibrosis distributed heterogeneously has higher arrhytmogenic potential than fibrosis distributed uniformly. We provided a quantitative investigation of this effect and found the boarders for the parameter region where there was a high chance for reentry formation. We investigated the spatiotemporal characteristics of the activation patterns and found that they are regular and periodic. We have shown that the period of activation patterns is determined by the regions with the highest fibrosis levels. We have also characterized the mechanism of the resulting activation patterns and have shown that for most of the cases it is mother rotor fibrillation. We have shown how the activation patterns can be terminated by applying an ablation procedure.

Chapter 4 was dedicated to developing a patient-specific model for greometry of the left ventricle out of patient specific MRI data. Following [132] we used a rule-based approach to assign the orientation of the fibers for a given point of the heart depending on the relative distance from endocardium from that point. We found the relative distance by solving the eikonal equations with appropriate boundary conditions. We coupled this approach with our model of fibrosis as small inexcitable obstacles.

Chapter 5 answered a research question posed in chapter 3, namely, why the period of the activation pattern for heterogeneous fibrosis distribution is determined by the regions where spiral rotation is the slowest. We have shown that such regions can attract the spiral waves. We studied the process of attraction in details and find that the regions that attract the spiral wave must be larger than a particular size and must have neither relatively large nor small level of local fibrosis. Using our patient-specific model developed in chapter 4 we demonstrated the effect of attraction in the clinical data.

We conclude that the question of arrhythmogenesis is tightly bounded with certain pathological conditions. Cardiac arrhythmia is usually the final step of the impact of a certain pathology. Therefore, arrhythmogenesis should not be considered *per se*, in the absence of any pathology. Arrhythmias that occur due to a presence of a certain pathology can be potentially treated once we know how this pathology affects the activation pattern.

Bibliography

[1] Guyton, A. and Hall, J. E., Textbook of Medical Physiology, 12 ed. Elsevier Health Sciences, 2010.

[2] Helmholtz, H. 1850. Messungen über den zeitlichen verlauf der zuckung animalischer muskeln und die fortpflanzungsgeschwindigkeit der reizung in den nerven. *Archiv für Anatomie, Physiologie und wissenschaftliche Medicin* :276.

[3] Kolmogorov, A. N., Petrovsky, I. G. and Piskunov, N. S. 1937. Study of the diffusion equation with growth of the quantity of matter and its application to a biological problem. *Bull. State Univ. Mos.* :1.

[4] Fisher, R. 1937. The wave of advance of advantageous genes. *Ann. Eugenics* 7:355.

[5] Mines, G. 1913. On dynamic equlibrium of the heart. *J. Physiol.* 46:349.

[6] MacWilliam, J. 1887. Fibrillar contraction of the heart. *J Physiol* 8:296.

[7] Mayer, A. G. 1906. Rhythmical pulsation in scyphomedusae. *Carnegie Institution Publication* 46:349.

[8] Wiener, N. and Rosenblueth, A. 1946. The mathematical formulation of the problem of conduction of impulses in a network of connected excitable elements, specifically in cardiac muscle. *Arch Inst Cardiol Mex* 16(3):205.

[9] Selfridge, O. 1948. Studies on flutter and fibrillation; some notes on the theory of flutter. *Arch Inst Cardiol Mex* 18(2):177.

[10] Allessie, M. A., Bonke, F. I. and Schopman, F. J. 1977. Circus movement in rabbit atrial muscle as a mechanism of tachycardia. iii. the "leading circle" concept: a new model of circus movement in cardiac tissue without the involvement of an anatomical obstacle. *Circ Res* 41(1):9.

[11] Davidenko, J. M., Kent, P. F., Chialvo, D. R., Michaels, D. C. and Jalife, J. 1990. Sustained vortex-like waves in normal isolated ventricular muscle. *Proc Natl Acad Sci U S A* 87(22):8785.

[12] Witkowski, F. X., Leon, L. J., Penkoske, P. A., Giles, W. R., Spano, M. L., Ditto, W. L. and Winfree, A. T. 1998. Spatiotemporal evolution of ventricu-

lar fibrillation. *Nature* 392(6671):78.

[13] Bub, G., Glass, L., Publicover, N. G. and Shrier, A. 1998. Bursting calcium rotors in cultured cardiac myocyte monolayers. *Proc Natl Acad Sci U S A* 95(17):10283.

[14] Iravanian, S., Nabutovsky, Y., Kong, C.-R., Saha, S., Bursac, N. and Tung, L. 2003. Functional reentry in cultured monolayers of neonatal rat cardiac cells. *Am J Physiol Heart Circ Physiol* 285(1):H449.

[15] Zaikin, A. N. and Zhabotinsky, A. M. 1970. Concentration wave propagation in two-dimensional liquid-phase self-oscillating system. *Nature* 225(5232):535.

[16] Winfree, A. T. 1972. Spiral waves of chemical activity. *Science* 175(4022):634.

[17] Zhabotinsky, A. M. and Zaikin, A. N. 1973. Autowave processes in a distributed chemical system. *J Theor Biol* 40(1):45.

[18] Mikhailov, A. S., Foundations of Synergetics I. Distributed active systems, 2nd rev. ed. 1994. Springer Verlag, 1990.

[19] Agladze, K., Davydov, V. and Mikhailov, A. 1987. An observation of resonance of spiral waves in distributed excitable medium. *JETP Lett* 45(12):767.

[20] Jalife, J., Delmar, M., Anumonwo, J., Berenfeld, O. and Kalifa, J., Basic Cardiac Electrophysiology for the Clinician. Wiley-Blackwell, 2009.

[21] Moe, G. K., Rheinboldt, W. C. and Abildskov, J. A. 1964. A computer model of atrial fibrillation. *American heart journal* 67(2):200.

[22] Rudenko, A. and Panfilov, A. 1983. Drift and interaction of vortices in two-dimensional heterogeneous active medium. *Studia Biophysica* 98(3):183.

[23] Rushton, W. 1937. Initiation of the propagated disturbance. *Proceedings of the Royal Society of London. Series B, Biological Sciences* 124(835):210.

[24] Markstein, G. 1951. Experimental and theoretical studies of flame front stability. *J. Aeronaut. Sci.* 18(3):199.

[25] Cabo, C., Pertsov, A. M., Baxter, W. T., Davidenko, J. M., Gray, R. A. and Jalife, J. 1994. Wave-front curvature as a cause of slow conduction and block in isolated cardiac muscle. *Circ Res* 75(6):1014.

[26] Carmeliet, E. 1999. Cardiac ionic currents and acute ischemia: from channels to arrhythmias. *Physiol Rev* 79(3):917.

[27] de Jong, S., van Veen, T. A. B., van Rijen, H. V. M. and de Bakker, J. M. T. 2011. Fibrosis and cardiac arrhythmias. *J Cardiovasc Pharmacol* 57(6):630.

[28] de Bakker, J. M., van Capelle, F. J., Janse, M. J., Wilde, A. A., Coronel, R., Becker, A. E., Dingemans, K. P., van Hemel, N. M. and Hauer, R. N. 1988. Reentry as a cause of ventricular tachycardia in patients with chronic

ischemic heart disease: electrophysiologic and anatomic correlation. *Circulation* 77(3):589.

[29] de Bakker, J. M., Coronel, R., Tasseron, S., Wilde, A. A., Opthof, T., Janse, M. J., van Capelle, F. J., Becker, A. E. and Jambroes, G. 1990. Ventricular tachycardia in the infarcted, langendorff-perfused human heart: role of the arrangement of surviving cardiac fibers. *J Am Coll Cardiol* 15(7):1594.

[30] Kogan, B. Y., Karplus, W. J., Billett, B. S. and Stevenson, W. G. 1992. Excitation wave propagation within narrow pathways: geometric configurations facilitating unidirectional block and reentry. *Physica D: Nonlinear Phenomena* 59(4):275.

[31] Casaclang-Verzosa, G., Gersh, B. J. and Tsang, T. S. M. 2008. Structural and functional remodeling of the left atrium: clinical and therapeutic implications for atrial fibrillation. *J Am Coll Cardiol* 51(1):1.

[32] Luong, C., Barnes, M. E. and Tsang, T. S. 2014. Atrial fibrillation and heart failure: cause or effect? *Current heart failure reports* 11(4):463.

[33] Hodgkin, A. L. and Huxley, A. F. 1952. A quantitative description of membrane current and its application to conduction and excitation in nerve. *The Journal of physiology* 117(4):500.

[34] FitzHugh, R. 1955. Mathematical models of threshold phenomena in the nerve membrane. *The bulletin of mathematical biophysics* 17(4):257.

[35] Nagumo, J., Arimoto, S. and Yoshizawa, S. 1962. An active pulse transmission line simulating nerve axon. *Proceedings of the IRE* 50(10):2061.

[36] Noble, D. 1962. A modification of the hodgkin-huxley equations applicable to purkinje fibre action and pacemaker potentials. *The Journal of Physiology* 160(2):317.

[37] Beeler, G. W. and Reuter, H. 1977. Reconstruction of the action potential of ventricular myocardial fibres. *J Physiol* 268(1):177.

[38] Luo, C. H. and Rudy, Y. 1991. A model of the ventricular cardiac action potential. depolarization, repolarization, and their interaction. *Circ Res* 68(6):1501.

[39] Luo, C. H. and Rudy, Y. 1994. A dynamic model of the cardiac ventricular action potential. i. simulations of ionic currents and concentration changes. *Circ Res* 74(6):1071.

[40] ten Tusscher, K. H. W. J., Noble, D., Noble, P. J. and Panfilov, A. V. 2004. A model for human ventricular tissue. *Am J Physiol Heart Circ Physiol* 286(4):H1573.

[41] ten Tusscher, K. H. W. J. and Panfilov, A. V. 2006. Alternans and spiral breakup in a human ventricular tissue model. *Am J Physiol Heart Circ Physiol* 291(3):H1088.

[42] Wiggers, C. J., Bell, J. R. and Paine, M. 2003. Studies of ventricular fibrillation caused by electric shock: II. Cinematographic and electrocardiographic observations of the natural process in the dog's heart. Its inhibition by potassium and the revival of coordinated beats by calcium. *Ann Noninvasive Electrocardiol* 8(3):252.

[43] Janse, M. J. and Wit, A. L. 1989. Electrophysiological mechanisms of ventricular arrhythmias resulting from myocardial ischemia and infarction. *Physiol Rev* 69(4):1049.

[44] Valenzuela, T. D., Roe, D. J., Cretin, S., Spaite, D. W. and Larsen, M. P. 1997. Estimating effectiveness of cardiac arrest interventions: a logistic regression survival model. *Circulation* 96(10):3308.

[45] Valenzuela, T. D., Roe, D. J., Nichol, G., Clark, L. L., Spaite, D. W. and Hardman, R. G. 2000. Outcomes of rapid defibrillation by security officers after cardiac arrest in casinos. *N Engl J Med* 343(17):1206.

[46] Huang, J., Rogers, J. M., Killingsworth, C. R., Singh, K. P., Smith, W. M. and Ideker, R. E. 2004. Evolution of activation patterns during long-duration ventricular fibrillation in dogs. *Am J Physiol Heart Circ Physiol* 286(3):H1193.

[47] Clayton, R. H., Zhuchkova, E. A. and Panfilov, A. V. 2006. Phase singularities and filaments: simplifying complexity in computational models of ventricular fibrillation. *Prog Biophys Mol Biol* 90(1-3):378.

[48] Huizar, J. F., Warren, M. D., Shvedko, A. G., Kalifa, J., Moreno, J., Mironov, S., Jalife, J. and Zaitsev, A. V. 2007. Three distinct phases of vf during global ischemia in the isolated blood-perfused pig heart. *Am J Physiol Heart Circ Physiol* 293(3):H1617.

[49] Nash, M. P., Mourad, A., Clayton, R. H., Sutton, P. M., Bradley, C. P., Hayward, M., Paterson, D. J. and Taggart, P. 2006. Evidence for multiple mechanisms in human ventricular fibrillation. *Circulation* 114(6):536.

[50] ten Tusscher, K. H. W. J., Mourad, A., Nash, M. P., Clayton, R. H., Bradley, C. P., Paterson, D. J., Hren, R., Hayward, M., Panfilov, A. V. and Taggart, P. 2009. Organization of ventricular fibrillation in the human heart: experiments and models. *Exp Physiol* 94(5):553.

[51] Massé, S., Farid, T., Dorian, P., Umapathy, K., Nair, K., Asta, J., Ross, H., Rao, V., Sevaptsidis, E. and Nanthakumar, K. 2009. Effect of global ischemia and reperfusion during ventricular fibrillation in myopathic human hearts. *Am J Physiol Heart Circ Physiol* 297(6):H1984.

[52] Farid, T. A., Nair, K., Massé, S., Azam, M. A., Maguy, A., Lai, P. F. H., Umapathy, K., Dorian, P., Chauhan, V., Varró, A., Al-Hesayen, A., Waxman, M., Nattel, S. and Nanthakumar, K. 2011. Role of KATP channels in the maintenance of ventricular fibrillation in cardiomyopathic human hearts. *Circ Res* 109(11):1309.

[53] Bradley, C. P., Clayton, R. H., Nash, M. P., Mourad, A., Hayward, M., Paterson, D. J. and Taggart, P. 2011. Human ventricular fibrillation during global ischemia and reperfusion / Clinical perspective. *Circulation: Arrhythmia and Electrophysiology* 4(5):684.

[54] Clayton, R. H., Nash, M. P., Bradley, C. P., Panfilov, A. V., Paterson, D. J. and Taggart, P. 2011. Experiment-model interaction for analysis of epicardial activation during human ventricular fibrillation with global myocardial ischaemia. *Prog Biophys Mol Biol* 107(1):101.

[55] Babenko, A. P., Gonzalez, G., Aguilar-Bryan, L. and Bryan, J. 1998. Reconstituted human cardiac KATP channels: functional identity with the native channels from the sarcolemma of human ventricular cells. *Circ Res* 83(11):1132.

[56] ten Tusscher, K. H. W. J. and Panfilov, A. V. 2004. Eikonal formulation of the minimal principle for scroll wave filaments. *Phys Rev Lett* 93(10):108106.

[57] Shaw, R. M. and Rudy, Y. 1997. Electrophysiologic effects of acute myocardial ischemia: a theoretical study of altered cell excitability and action potential duration. *Cardiovasc Res* 35(2):256.

[58] Rodriguez, J., Heidenreich, E., Romero, L., Ferrero, J. and Doblare, M., Post-repolarization refractoriness in human ventricular cardiac cells. In Computers in Cardiology, 2008, 2008, 581–584.

[59] ten Tusscher, K. H. W. J., Hren, R. and Panfilov, A. V. 2007. Organization of ventricular fibrillation in the human heart. *Circ Res* 100(12):e87.

[60] Hren, R. 1996. A Realistic Model of the Human Ventricular Myocardium: Applications to the Study of Ectopic Activation. Ph.D. thesis, Nova Scotia, Canada: Dalhousie University.

[61] ten Tusscher, K. H. W. J. and Panfilov, A. V. 2008. Modelling of the ventricular conduction system. *Prog Biophys Mol Biol* 96(1-3):152.

[62] Rush, S. and Larsen, H. 1978. A practical algorithm for solving dynamic membrane equations. *IEEE Trans Biomed Eng* 25(4):389.

[63] Panfilov, A. V. 1998. Spiral breakup as a model of ventricular fibrillation. *Chaos* 8(1):57.

[64] Garfinkel, A., Kim, Y. H., Voroshilovsky, O., Qu, Z., Kil, J. R., Lee, M. H., Karagueuzian, H. S., Weiss, J. N. and Chen, P. S. 2000. Preventing ventricular fibrillation by flattening cardiac restitution. *Proc Natl Acad Sci USA* 97(11):6061.

[65] Bingen, B. O., Askar, S. F. A., Schalij, M. J., Kazbanov, I. V., Ypey, D. L., Panfilov, A. V. and Pijnappels, D. A. 2013. Prolongation of minimal action potential duration in sustained fibrillation decreases complexity by transient destabilization. *Cardiovasc Res* 97(1):161.

[66] Xie, F., Qu, Z., Yang, J., Baher, A., Weiss, J. N. and Garnfinkel, A. 2004. A

simulation study of the effects of cardiac anatomy in ventricular fibrillation. *Journal of Clinical Investigation* 113(5):686.

[67] Xie, F., Qu, Z., Garfinkel, A. and Weiss, J. N. 2001. Effects of simulated ischemia on spiral wave stability. *Am J Physiol Heart Circ Physiol* 280(4):H1667.

[68] Uchida, T., Yashima, M., Gotoh, M., Qu, Z., Garfinkel, A., Weiss, J. N., Fishbein, M. C., Mandel, W. J., Chen, P. S. and Karagueuzian, H. S. 1999. Mechanism of acceleration of functional reentry in the ventricle: effects of atp-sensitive potassium channel opener. *Circulation* 99(5):704.

[69] Quintanilla, J. G., Moreno, J., Archondo, T., Chin, A., Pérez-Castellano, N., Usandizaga, E., García-Torrent, M. J., Molina-Morúa, R., González, P., Rodríguez-Bobada, C., Macaya, C. and Pérez-Villacastín, J. 2013. KATP channel opening accelerates and stabilizes rotors in a swine heart model of ventricular fibrillation. *Cardiovasc Res* 99(3):576.

[70] Coronel, R., Fiolet, J. W., Wilms-Schopman, F. J., Schaapherder, A. F., Johnson, T. A., Gettes, L. S. and Janse, M. J. 1988. Distribution of extracellular potassium and its relation to electrophysiologic changes during acute myocardial ischemia in the isolated perfused porcine heart. *Circulation* 77(5):1125.

[71] Taggart, P., Sutton, P. M., Boyett, M. R., Lab, M. and Swanton, H. 1996. Human ventricular action potential duration during short and long cycles. rapid modulation by ischemia. *Circulation* 94(10):2526.

[72] Knopp, A., Thierfelder, S., Koopmann, R., Biskup, C., Böhle, T. and Benndorf, K. 1999. Anoxia generates rapid and massive opening of KATP channels in ventricular cardiac myocytes. *Cardiovasc Res* 41(3):629.

[73] Ganitkevich, V., Reil, S., Schwethelm, B., Schroeter, T. and Benndorf, K. 2006. Dynamic responses of single cardiomyocytes to graded ischemia studied by oxygen clamp in on-chip picochambers. *Circ Res* 99(2):165.

[74] Clayton, R. H., Murray, A. and Campbell, R. W. 1994. Changes in the surface electrocardiogram during the onset of spontaneous ventricular fibrillation in man. *Eur Heart J* 15(2):184.

[75] Mandapati, R., Asano, Y., Baxter, W. T., Gray, R., Davidenko, J. and Jalife, J. 1998. Quantification of effects of global ischemia on dynamics of ventricular fibrillation in isolated rabbit heart. *Circulation* 98(16):1688.

[76] Antzelevitch, C., Sicouri, S., Litovsky, S. H., Lukas, A., Krishnan, S. C., Di Diego, J. M., Gintant, G. A. and Liu, D. W. 1991. Heterogeneity within the ventricular wall. electrophysiology and pharmacology of epicardial, endocardial, and m cells. *Circ Res* 69(6):1427.

[77] Potse, M., Dubé, B., Richer, J., Vinet, A. and Gulrajani, R. M. 2006. A comparison of monodomain and bidomain reaction-diffusion models for ac-

tion potential propagation in the human heart. *IEEE Trans Biomed Eng* 53(12 Pt 1):2425.

[78] Grandi, E., Pasqualini, F. S. and Bers, D. M. 2010. A novel computational model of the human ventricular action potential and ca transient. *J Mol Cell Cardiol* 48(1):112.

[79] O'Hara, T., Virág, L., Varró, A. and Rudy, Y. 2011. Simulation of the undiseased human cardiac ventricular action potential: model formulation and experimental validation. *PLoS Comput Biol* 7(5):e1002061.

[80] Kléber, A. G., Riegger, C. B. and Janse, M. J. 1987. Electrical uncoupling and increase of extracellular resistance after induction of ischemia in isolated, arterially perfused rabbit papillary muscle. *Circ Res* 61(2):271.

[81] Rodríguez-Sinovas, A., García-Dorado, D., Padilla, F., Inserte, J., Barrabés, J. A., Ruiz-Meana, M., Agulló, L. and Soler-Soler, J. 2003. Pre-treatment with the Na+/H+ exchange inhibitor cariporide delays cell-to-cell electrical uncoupling during myocardial ischemia. *Cardiovasc Res* 58(1):109.

[82] Cascio, W. E., Yang, H., Muller-Borer, B. J. and Johnson, T. A. 2005. Ischemia-induced arrhythmia: the role of connexins, gap junctions, and attendant changes in impulse propagation. *J Electrocardiol* 38(4 Suppl):55.

[83] Boyle, P. M., Massé, S., Nanthakumar, K. and Vigmond, E. J. 2013. Transmural IK(ATP) heterogeneity as a determinant of activation rate gradient during early ventricular fibrillation: Mechanistic insights from rabbit ventricular models. *Heart Rhythm* 10(11):1710.

[84] Dosdall, D. J., Tabereaux, P. B., Kim, J. J., Walcott, G. P., Rogers, J. M., Killingsworth, C. R., Huang, J., Robertson, P. G., Smith, W. M. and Ideker, R. E. 2008. Chemical ablation of the purkinje system causes early termination and activation rate slowing of long-duration ventricular fibrillation in dogs. *Am J Physiol Heart Circ Physiol* 295(2):H883.

[85] Keldermann, R. H., ten Tusscher, K. H. W. J., Nash, M. P., Hren, R., Taggart, P. and Panfilov, A. V. 2008. Effect of heterogeneous APD restitution on VF organization in a model of the human ventricles. *Am J Physiol Heart Circ Physiol* 294(2):H764.

[86] Keldermann, R. H., ten Tusscher, K. H. W. J., Nash, M. P., Bradley, C. P., Hren, R., Taggart, P. and Panfilov, A. V. 2009. A computational study of mother rotor VF in the human ventricles. *Am J Physiol Heart Circ Physiol* 296(2):H370.

[87] Cha, Y. M., Uchida, T., Wolf, P. L., Peters, B. B., Fishbein, M. C., Karagueuzian, H. S. and Chen, P. S. 1995. Effects of chemical subendocardial ablation on activation rate gradient during ventricular fibrillation. *Am J Physiol* 269(6 Pt 2):H1998.

[88] Sutton, M. S. J., Lee, D., Rouleau, J. L., Goldman, S., Plappert, T., Braun-

wald, E. and Pfeffer, M. A. 2003. Left ventricular remodeling and ventricular arrhythmias after myocardial infarction. *Circulation* 107(20):2577.

[89] Nattel, S., Maguy, A., Le Bouter, S. and Yeh, Y.-H. 2007. Arrhythmogenic ion-channel remodeling in the heart: heart failure, myocardial infarction, and atrial fibrillation. *Physiol Rev* 87(2):425.

[90] Nattel, S., Burstein, B. and Dobrev, D. 2008. Atrial remodeling and atrial fibrillation: mechanisms and implications. *Circ Arrhythm Electrophysiol* 1(1):62.

[91] Kawara, T., Derksen, R., de Groot, J. R., Coronel, R., Tasseron, S., Linnenbank, A. C., Hauer, R. N., Kirkels, H., Janse, M. J. and de Bakker, J. M. 2001. Activation delay after premature stimulation in chronically diseased human myocardium relates to the architecture of interstitial fibrosis. *Circulation* 104(25):3069.

[92] de Jong, S., van Veen, T. A. B., de Bakker, J. M. T., Vos, M. A. and van Rijen, H. V. M. 2011. Biomarkers of myocardial fibrosis. *J Cardiovasc Pharmacol* 57(5):522.

[93] Tanaka, K., Zlochiver, S., Vikstrom, K. L., Yamazaki, M., Moreno, J., Klos, M., Zaitsev, A. V., Vaidyanathan, R., Auerbach, D. S., Landas, S., Guiraudon, G., Jalife, J., Berenfeld, O. and Kalifa, J. 2007. Spatial distribution of fibrosis governs fibrillation wave dynamics in the posterior left atrium during heart failure. *Circ Res* 101(8):839.

[94] Stein, M., Noorman, M., van Veen, T. A. B., Herold, E., Engelen, M. A., Boulaksil, M., Antoons, G., Jansen, J. A., van Oosterhout, M. F. M., Hauer, R. N. W., de Bakker, J. M. T. and van Rijen, H. V. M. 2008. Dominant arrhythmia vulnerability of the right ventricle in senescent mice. *Heart Rhythm* 5(3):438.

[95] Campian, M. E., Hardziyenka, M., de Bruin, K., van Eck-Smit, B. L. F., de Bakker, J. M. T., Verberne, H. J. and Tan, H. L. 2010. Early inflammatory response during the development of right ventricular heart failure in a rat model. *Eur J Heart Fail* 12(7):653.

[96] van Veen, T. A. B., Stein, M., Royer, A., Quang, K. L., Charpentier, F., Colledge, W. H., Huang, C. L.-H., Wilders, R., Grace, A. A., Escande, D., de Bakker, J. M. T. and van Rijen, H. V. M. 2005. Impaired impulse propagation in scn5a-knockout mice: combined contribution of excitability, connexin expression, and tissue architecture in relation to aging. *Circulation* 112(13):1927.

[97] Panfilov, A. V. 2002. Spiral breakup in an array of coupled cells: the role of the intercellular conductance. *Phys Rev Lett* 88(11):118101.

[98] ten Tusscher, K. H. W. J. and Panfilov, A. V. 2003. Influence of nonexcitable cells on spiral breakup in two-dimensional and three-dimensional excitable media. *Phys Rev E Stat Nonlin Soft Matter Phys* 68(6 Pt 1):062902.

[99] ten Tusscher, K. H. W. J. and Panfilov, A. V. 2005. Wave propagation in excitable media with randomly distributed obstacles. *SIAM Journal of Multiscale Modeling & Simulation* 3:265.

[100] ten Tusscher, K. H. W. J. and Panfilov, A. V. 2007. Influence of diffuse fibrosis on wave propagation in human ventricular tissue. *Europace* 9 Suppl 6:vi38.

[101] Alonso, S., Bär, M. and Panfilov, A. V. 2011. Effects of reduced discrete coupling on filament tension in excitable media. *Chaos* 21(1):013118.

[102] Majumder, R., Nayak, A. R. and Pandit, R. 2012. Nonequilibrium arrhythmic states and transitions in a mathematical model for diffuse fibrosis in human cardiac tissue. *PLoS One* 7(10):e45040.

[103] Jacquemet, V. and Henriquez, C. S. 2007. Modelling cardiac fibroblasts: interactions with myocytes and their impact on impulse propagation. *Europace* 9 Suppl 6:vi29.

[104] Zlochiver, S., Muñoz, V., Vikstrom, K. L., Taffet, S. M., Berenfeld, O. and Jalife, J. 2008. Electrotonic myofibroblast-to-myocyte coupling increases propensity to reentrant arrhythmias in two-dimensional cardiac monolayers. *Biophys J* 95(9):4469.

[105] Ashihara, T., Haraguchi, R., Nakazawa, K., Namba, T., Ikeda, T., Nakazawa, Y., Ozawa, T., Ito, M., Horie, M. and Trayanova, N. A. 2012. The role of fibroblasts in complex fractionated electrograms during persistent/permanent atrial fibrillation: implications for electrogram-based catheter ablation. *Circ Res* 110(2):275.

[106] McDowell, K. S., Zahid, S., Vadakkumpadan, F., Blauer, J., MacLeod, R. S. and Trayanova, N. A. 2015. Virtual electrophysiological study of atrial fibrillation in fibrotic remodeling. *PLoS One* 10(2):e0117110.

[107] Trayanova, N. A., Boyle, P. M., Arevalo, H. J. and Zahid, S. 2014. Exploring susceptibility to atrial and ventricular arrhythmias resulting from remodeling of the passive electrical properties in the heart: a simulation approach. *Front Physiol* 5:435.

[108] Gonzales, M. J., Vincent, K. P., Rappel, W.-J., Narayan, S. M. and McCulloch, A. D. 2014. Structural contributions to fibrillatory rotors in a patient-derived computational model of the atria. *Europace* 16 Suppl 4:iv3.

[109] Taggart, P., Sutton, P. M., Opthof, T., Coronel, R., Trimlett, R., Pugsley, W. and Kallis, P. 2000. Inhomogeneous transmural conduction during early ischaemia in patients with coronary artery disease. *J Mol Cell Cardiol* 32(4):621.

[110] Press, W. H., Teukolsky, S. A., Vetterling, W. T. and Flannery, B. P., Numerical Recipes: The Art of Scientific Computing, 3rd ed. Cambridge University Press, 2007.

[111] Zaitsev, A. V., Berenfeld, O., Mironov, S. F., Jalife, J. and Pertsov, A. M. 2000. Distribution of excitation frequencies on the epicardial and endocardial surfaces of fibrillating ventricular wall of the sheep heart. *Circ Res* 86(4):408.

[112] Skanes, A. C., Mandapati, R., Berenfeld, O., Davidenko, J. M. and Jalife, J. 1998. Spatiotemporal periodicity during atrial fibrillation in the isolated sheep heart. *Circulation* 98(12):1236.

[113] Wenckebach, K. F. 1899. Zur analyse des unregelmassigen pulses. *Z Klin Med* 37:475.

[114] Jalife, J. 2000. Ventricular fibrillation: mechanisms of initiation and maintenance. *Annu Rev Physiol* 62:25.

[115] Spector, P. S., Correa de Sa, D. D., Tischler, E. S., Thompson, N. C., Habel, N., Stinnett-Donnelly, J., Benson, B. E., Bielau, P. and Bates, J. H. T. 2012. Ablation of multi-wavelet re-entry: general principles and in silico analyses. *Europace* 14 Suppl 5:v106.

[116] Panfilov, A. V. 2006. Is heart size a factor in ventricular fibrillation? or how close are rabbit and human hearts? *Heart Rhythm* 3(7):862.

[117] Hansen, B. J., Zhao, J., Csepe, T. A., Moore, B. T., Li, N., Jayne, L. A., Kalyanasundaram, A., Lim, P., Bratasz, A., Powell, K. A., Simonetti, O. P., Higgins, R. S. D., Kilic, A., Mohler, P. J., Janssen, P. M. L., Weiss, R., Hummel, J. D. and Fedorov, V. V. 2015. Atrial fibrillation driven by microanatomic intramural re-entry revealed by simultaneous sub-epicardial and sub-endocardial optical mapping in explanted human hearts. *Eur Heart J* 36(35):2390.

[118] Samie, F. H., Berenfeld, O., Anumonwo, J., Mironov, S. F., Udassi, S., Beaumont, J., Taffet, S., Pertsov, A. M. and Jalife, J. 2001. Rectification of the background potassium current: a determinant of rotor dynamics in ventricular fibrillation. *Circ Res* 89(12):1216.

[119] Wu, T.-J., Lin, S.-F., Baher, A., Qu, Z., Garfinkel, A., Weiss, J. N., Ting, C.-T. and Chen, P.-S. 2004. Mother rotors and the mechanisms of d600-induced type 2 ventricular fibrillation. *Circulation* 110(15):2110.

[120] Narayan, S. M., Krummen, D. E., Shivkumar, K., Clopton, P., Rappel, W.-J. and Miller, J. M. 2012. Treatment of atrial fibrillation by the ablation of localized sources: Confirm (conventional ablation for atrial fibrillation with or without focal impulse and rotor modulation) trial. *J Am Coll Cardiol* 60(7):628.

[121] Panfilov, A. V. and Keener, J. P. 1993. Effects of high frequency stimulation on cardiac tissue with an inexcitable obstacle. *Journal of theoretical biology* 163(4):439.

[122] Agladze, K., Keener, J. P., Müller, S. C. and Panfilov, A. 1994. Rotating spi-

ral waves created by geometry. *Science* 264(5166):1746.

[123] Majumder, R., Pandit, R. and Panfilov, A. V. 2014. Turbulent electrical activity at sharp-edged inexcitable obstacles in a model for human cardiac tissue. *Am J Physiol Heart Circ Physiol* 307(7):H1024.

[124] Panfilov, A. and Vasiev, B. 1991. Vortex initiation in a heterogeneous excitable medium. *Physica D: Nonlinear Phenomena* 49(1):107.

[125] Krinsky, V. I. 1966. Spread of excitation in an inhomogeneous medium (state similar to cardiac fibrillation). *Biophysics* 11:776.

[126] Kohl, P. and Gourdie, R. G. 2014. Fibroblast-myocyte electrotonic coupling: does it occur in native cardiac tissue? *J Mol Cell Cardiol* 70:37.

[127] Allessie, M., Ausma, J. and Schotten, U. 2002. Electrical, contractile and structural remodeling during atrial fibrillation. *Cardiovasc Res* 54(2):230.

[128] Angel, N., Li, L. I., Macleod, R. S., Marrouche, N., Ranjan, R. and Dosdall, D. J. 2015. Diverse fibrosis architecture and premature stimulation facilitate initiation of reentrant activity following chronic atrial fibrillation. *J Cardiovasc Electrophysiol* .

[129] Kudryashova, N. N., Teplenin, A. S., Orlova, Y. V., Selina, L. V. and Agladze, K. 2014. Arrhythmogenic role of the border between two areas of cardiac cell alignment. *J Mol Cell Cardiol* 76:227.

[130] Morita, N., Sovari, A. A., Xie, Y., Fishbein, M. C., Mandel, W. J., Garfinkel, A., Lin, S.-F., Chen, P.-S., Xie, L.-H., Chen, F., Qu, Z., Weiss, J. N. and Karagueuzian, H. S. 2009. Increased susceptibility of aged hearts to ventricular fibrillation during oxidative stress. *Am J Physiol Heart Circ Physiol* 297(5):H1594.

[131] Comtois, P. and Nattel, S. 2011. Interactions between cardiac fibrosis spatial pattern and ionic remodeling on electrical wave propagation. *Conf Proc IEEE Eng Med Biol Soc* 2011:4669.

[132] Streeter, D. D. J. 1979. Gross morphology and fiber geometry of the heart. *Handbook of Physiology* 1:61.

[133] Potse, M., Krause, D., Kroon, W., Murzilli, R., Muzzarelli, S., Regoli, F., Caiani, E., Prinzen, F. W., Krause, R. and Auricchio, A. 2014. Patient-specific modelling of cardiac electrophysiology in heart-failure patients. *Europace* 16 Suppl 4:iv56.

[134] McDowell, K. S., Vadakkumpadan, F., Blake, R., Blauer, J., Plank, G., MacLeod, R. S. and Trayanova, N. A. 2012. Methodology for patient-specific modeling of atrial fibrosis as a substrate for atrial fibrillation. *J Electrocardiol* 45(6):640.

[135] Spach, M. S., Miller, W., 3rd, Dolber, P. C., Kootsey, J. M., Sommer, J. R. and Mosher, C., Jr. 1982. The functional role of structural complexities in the propagation of depolarization in the atrium of the dog. cardiac conduction

disturbances due to discontinuities of effective axial resistivity. *Circ Res* 50(2):175.

[136] Li, D., Fareh, S., Leung, T. K. and Nattel, S. 1999. Promotion of atrial fibrillation by heart failure in dogs: atrial remodeling of a different sort. *Circulation* 100(1):87.

[137] Kazbanov, I. V., ten Tusscher, K. H. W. J. and Panfilov, A. V. 2016. Effects of heterogeneous diffuse fibrosis on arrhythmia dynamics and mechanism. *Scientific Reports* 6:20835.

[138] Engelman, Z. J., Trew, M. L. and Smaill, B. H. 2010. Structural heterogeneity alone is a sufficient substrate for dynamic instability and altered restitution. *Circ Arrhythm Electrophysiol* 3(2):195.

[139] Kim, R. J., Fieno, D. S., Parrish, T. B., Harris, K., Chen, E. L., Simonetti, O., Bundy, J., Finn, J. P., Klocke, F. J. and Judd, R. M. 1999. Relationship of mri delayed contrast enhancement to irreversible injury, infarct age, and contractile function. *Circulation* 100(19):1992.

[140] Kim, R. J., Wu, E., Rafael, A., Chen, E.-L., Parker, M. A., Simonetti, O., Klocke, F. J., Bonow, R. O. and Judd, R. M. 2000. The use of contrast-enhanced magnetic resonance imaging to identify reversible myocardial dysfunction. *New England Journal of Medicine* 343(20):1445.

[141] de Jong, S., Zwanenburg, J. J., Visser, F., van der Nagel, R., van Rijen, H. V., Vos, M. A., de Bakker, J. M. and Luijten, P. R. 2011. Direct detection of myocardial fibrosis by mri. *J Mol Cell Cardiol* 51(6):974.

[142] Vetter, F. J., Simons, S. B., Mironov, S., Hyatt, C. J. and Pertsov, A. M. 2005. Epicardial fiber organization in swine right ventricle and its impact on propagation. *Circ Res* 96(2):244.

[143] Roberts, D. E., Hersh, L. T. and Scher, A. M. 1979. Influence of cardiac fiber orientation on wavefront voltage, conduction velocity, and tissue resistivity in the dog. *Circ Res* 44(5):701.

[144] Panfilov, A. and Rudenko, A. 1987. Two regimes of the scroll ring drift in the three-dimensional active media. *Physica D: Nonlinear Phenomena* 28(1):215.

[145] Wellner, M., Berenfeld, O., Jalife, J. and Pertsov, A. M. 2002. Minimal principle for rotor filaments. *Proc Natl Acad Sci U S A* 99(12):8015.

[146] Fenton, F. and Karma, A. 1998. Vortex dynamics in three-dimensional continuous myocardium with fiber rotation: Filament instability and fibrillation. *Chaos* 8(1):20.

[147] Panfilov, A. V. and Keener, J. P. 1993. Generation of reentry in anisotropic myocardium. *J Cardiovasc Electrophysiol* 4(4):412.

[148] Kudryashova, N. N., Kazbanov, I. V., Panfilov, A. V. and Agladze, K. I. 2015. Conditions for waveblock due to anisotropy in a model of human

ventricular tissue. *PLoS One* 10(11):e0141832.

[149] Roes, S. D., Borleffs, C. J. W., van der Geest, R. J., Westenberg, J. J. M., Marsan, N. A., Kaandorp, T. A. M., Reiber, J. H. C., Zeppenfeld, K., Lamb, H. J., de Roos, A., Schalij, M. J. and Bax, J. J. 2009. Infarct tissue heterogeneity assessed with contrast-enhanced mri predicts spontaneous ventricular arrhythmia in patients with ischemic cardiomyopathy and implantable cardioverter-defibrillator. *Circ Cardiovasc Imaging* 2(3):183.

[150] Piers, S. R. D., Tao, Q., de Riva Silva, M., Siebelink, H.-M., Schalij, M. J., van der Geest, R. J. and Zeppenfeld, K. 2014. Cmr-based identification of critical isthmus sites of ischemic and nonischemic ventricular tachycardia. *JACC Cardiovasc Imaging* 7(8):774.

[151] Osher, S. and Sethian, J. A. 1988. Fronts propagating with curvature-dependent speed: algorithms based on hamilton-jacobi formulations. *Journal of computational physics* 79(1):12.

[152] Sethian, J. A. 1996. A fast marching level set method for monotonically advancing fronts. *Proceedings of the National Academy of Sciences* 93(4):1591.

[153] Bishop, M. J., Plank, G., Burton, R. A. B., Schneider, J. E., Gavaghan, D. J., Grau, V. and Kohl, P. 2010. Development of an anatomically detailed mri-derived rabbit ventricular model and assessment of its impact on simulations of electrophysiological function. *Am J Physiol Heart Circ Physiol* 298(2):H699.

[154] Ragnemalm, I. 1992. Neighborhoods for distance transformations using ordered propagation. *CVGIP: Image Understanding* 56(3):399.

[155] Tsitsiklis, J. N. 1995. Efficient algorithms for globally optimal trajectories. *Automatic Control, IEEE Transactions on* 40(9):1528.

[156] Dijkstra, E. W. 1959. A note on two problems in connexion with graphs. *Numerische mathematik* 1(1):269.

[157] Bayer, J. D., Blake, R. C., Plank, G. and Trayanova, N. A. 2012. A novel rule-based algorithm for assigning myocardial fiber orientation to computational heart models. *Ann Biomed Eng* 40(10):2243.

[158] Chan, T. F., Shen, J. and Vese, L. 2003. Variational pde models in image processing. *Notices AMS* 50:14.

[159] Delacrétaz, E., Brenner, R., Schaumann, A., Eckardt, L., Willems, S., Pitschner, H.-F., Kautzner, J., Schumacher, B., Hansen, P. S., Kuck, K.-H. and , V. T. A. C. H. S. G. 2013. Catheter ablation of stable ventricular tachycardia before defibrillator implantation in patients with coronary heart disease (vtach): an on-treatment analysis. *J Cardiovasc Electrophysiol* 24(5):525.

[160] Reddy, V. Y., Reynolds, M. R., Neuzil, P., Richardson, A. W., Taborsky, M., Jongnarangsin, K., Kralovec, S., Sediva, L., Ruskin, J. N. and Josephson, M. E. 2007. Prophylactic catheter ablation for the prevention of defibrillator

therapy. *N Engl J Med* 357(26):2657.

[161] Aliot, E. M., Stevenson, W. G., Almendral-Garrote, J. M., Bogun, F., Calkins, C. H., Delacretaz, E., Della Bella, P., Hindricks, G., Jaïs, P., Josephson, M. E., Kautzner, J., Kay, G. N., Kuck, K.-H., Lerman, B. B., Marchlinski, F., Reddy, V., Schalij, M.-J., Schilling, R., Soejima, K., Wilber, D., , E. H. R. A. E. H. R. A., , R. B. o. t. E. S. o. C. E. S. C., , H. R. S. H. R. S., , A. C. o. C. A. C. C. and , A. H. A. A. H. A. 2009. Ehra/hrs expert consensus on catheter ablation of ventricular arrhythmias: developed in a partnership with the european heart rhythm association (ehra), a registered branch of the european society of cardiology (esc), and the heart rhythm society (hrs); in collaboration with the american college of cardiology (acc) and the american heart association (aha). *Heart Rhythm* 6(6):886.

[162] Stevenson, W. G., Wilber, D. J., Natale, A., Jackman, W. M., Marchlinski, F. E., Talbert, T., Gonzalez, M. D., Worley, S. J., Daoud, E. G., Hwang, C., Schuger, C., Bump, T. E., Jazayeri, M., Tomassoni, G. F., Kopelman, H. A., Soejima, K., Nakagawa, H. and , M. T. V. T. A. T. I. 2008. Irrigated radiofrequency catheter ablation guided by electroanatomic mapping for recurrent ventricular tachycardia after myocardial infarction: the multicenter thermocool ventricular tachycardia ablation trial. *Circulation* 118(25):2773.

[163] Tung, R., Josephson, M. E., Reddy, V., Reynolds, M. R. and , S. M. A. S. H.-V. T. I. 2010. Influence of clinical and procedural predictors on ventricular tachycardia ablation outcomes: an analysis from the substrate mapping and ablation in sinus rhythm to halt ventricular tachycardia trial (smash-vt). *J Cardiovasc Electrophysiol* 21(7):799.

[164] Dinov, B., Fiedler, L., Schönbauer, R., Bollmann, A., Rolf, S., Piorkowski, C., Hindricks, G. and Arya, A. 2014. Outcomes in catheter ablation of ventricular tachycardia in dilated nonischemic cardiomyopathy compared with ischemic cardiomyopathy: results from the prospective heart centre of leipzig vt (help-vt) study. *Circulation* 129(7):728.

[165] Piers, S. R. D., Leong, D. P., van Huls van Taxis, C. F. B., Tayyebi, M., Trines, S. A., Pijnappels, D. A., Delgado, V., Schalij, M. J. and Zeppenfeld, K. 2013. Outcome of ventricular tachycardia ablation in patients with nonischemic cardiomyopathy: the impact of noninducibility. *Circ Arrhythm Electrophysiol* 6(3):513.

[166] de Riva, M., Piers, S. R. D., Kapel, G. F. L., Watanabe, M., Venlet, J., Trines, S. A., Schalij, M. J. and Zeppenfeld, K. 2015. Reassessing noninducibility as ablation endpoint of post-infarction ventricular tachycardia: the impact of left ventricular function. *Circ Arrhythm Electrophysiol* 8(4):853.

[167] Jadidi, A. S., Cochet, H., Shah, A. J., Kim, S. J., Duncan, E., Miyazaki, S., Sermesant, M., Lehrmann, H., Lederlin, M., Linton, N., Forclaz, A., Nault, I., Rivard, L., Wright, M., Liu, X., Scherr, D., Wilton, S. B., Roten, L., Pascale, P., Derval, N., Sacher, F., Knecht, S., Keyl, C., Hocini, M., Montaudon,

M., Laurent, F., Haïssaguerre, M. and Jaïs, P. 2013. Inverse relationship between fractionated electrograms and atrial fibrosis in persistent atrial fibrillation: combined magnetic resonance imaging and high-density mapping. *J Am Coll Cardiol* 62(9):802.

[168] Defauw, A., Vandersickel, N., Dawyndt, P. and Panfilov, A. V. 2014. Small size ionic heterogeneities in the human heart can attract rotors. *Am J Physiol Heart Circ Physiol* 307(10):H1456.

List of Publications

- **Kazbanov IV, Vandersickel N, Watanabe M, Tao Q, Fostier J, Zeppenfeld K, Panfilov AV** Attraction of arrhythima sources by fibrotic scars via dynamical restructuring of the action pattern, *in preparation*

- **Kazbanov IV, ten Tusscher KHWJ, Panfilov AV** Effects of Heterogeneous Diffuse Fibrosis on Arrhythmia Dynamics and Mechanism, *Sci Rep*. 2016 Feb;6:20835

- **Kudryashova NN, Kazbanov IV, Panfilov AV, Agladze KI.** Conditions for Waveblock Due to Anisotropy in a Model of Human Ventricular Tissue. *PLoS One*. 2015 Nov 2;10(11):e0141832.

- **Vandersickel N, Kazbanov IV, Defauw A, Pijnappels DA, Panfilov AV.** Decreased repolarization reserve increases defibrillation threshold by favoring early afterdepolarizations in an in silico model of human ventricular tissue. *Heart Rhythm*. 2015 May;12(5):1088–96

- **Kazbanov IV, Clayton RH, Nash MP, Bradley CP, Paterson DJ, Hayward MP, Taggart P, Panfilov AV.** Effect of global cardiac ischemia on human ventricular fibrillation: insights from a multi-scale mechanistic model of the human heart. *PLoS Comput Biol*. 2014 Nov 6; 10(11):e1003891.

- **Vandersickel N, Kazbanov IV, Nuitermans A, Weise LD, Pandit R, Panfilov AV**. A study of early afterdepolarizations in a model for human ventricular tissue. *PLoS One*. 2014 Jan 10;9(1):e84595

- **Bingen BO, Askar SF, Schalij MJ, Kazbanov IV, Ypey DL, Panfilov AV, Pijnappels DA**. Prolongation of minimal action potential duration in sustained fibrillation decreases complexity by transient destabilization. *Cardiovasc Res*. 2013 Jan 1;97(1):161–70

- **Bingen BO, Neshati Z, Askar SF, Kazbanov IV, Ypey DL, Panfilov AV, Schalij MJ, de Vries AA, Pijnappels DA**. Atrium-specific Kir3.x determines inducibility, dynamics, and termination of fibrillation by regulating restitution-driven alternans. *Circulation*. 2013 Dec 24;128(25):2732–44

• **Defauw A, Kazbanov IV, Dierckx H, Dawyndt P, Panfilov AV.** Action potential duration heterogeneity of cardiac tissue can be evaluated from cell properties using Gaussian Green's function approach. *PLoS One*. 2013 Nov 18;8(11):e79607

Acknowledgments

I am sincerely grateful to my promotor and scientific mentor Prof. Alexander Panfilov.

I would like to thank Prof. Mikhail Gromov for inviting me as a visitor to Institut des Hautes Études Scientifiques (IHES).

I want to thank Robert Young whom I had a chance to work with for a month at IHES. He has highly impacted the evolution of my scientific interests for the time of my PhD study.

I heartily thank Daniel Weise whom I met in Utrecht University and had a pleasure of working with during last years. Apart from his scientific input, I appreciate him being a good friend of mine.

This thesis would have never been possible without Kirsten ten Tusscher whose work I deeply appreciate. Her impact on my research is hardly possible to overestimate. Apart from being my coauthor, she put a cornerstone to most of the research performed in our group.

I would like to thank Richard Clayton for his huge contribution to a chapter of this thesis and his fantastic writing skills. I also thank Martin Nash, Chris Bradley and Peter Taggart for being so conscientious coathors.

With my deep respect I want to thank Daniël Pijnappels for his enormous impact on my progress as a researcher. It has always been encouraging and educational to be a part of his research projects. During my collaboration with Daniël, I had a pleasure to meet other members of Laboratory of Experimental Cardiology at Leiden University Medical Center whom I would also like to thank. I am grateful to Saïd Askar and Brian Bingen for giving me an opportunity to contribute to their research. I thank Antoine de Vries for sharing his ideas and extremely pleasant discussions. I thank Dick Ypey for being so interested in my research. I am very grateful to Marc Engels for being so helpful and friendly during my stay in Leiden. With all the warmness of my heart I would like to thank Rupa Majumder for our collaboration and for being so positive towards me. I am very grateful to Sasha Teplenin whom I have a joy to study from. I would like to thank Masaya Watanabe for his contribution to this thesis. I thank Prof. Katja Zeppenfeld for her interest in my research. I am grateful to Yoke Jangsangthong, Iolanda Feola, Jia Liu, Annemarie Kip, Minka Bax, Cindy